LONG-TERM STRUCTURAL MODELING OF THE NORTH HALAWA VALLEY VIADUCT

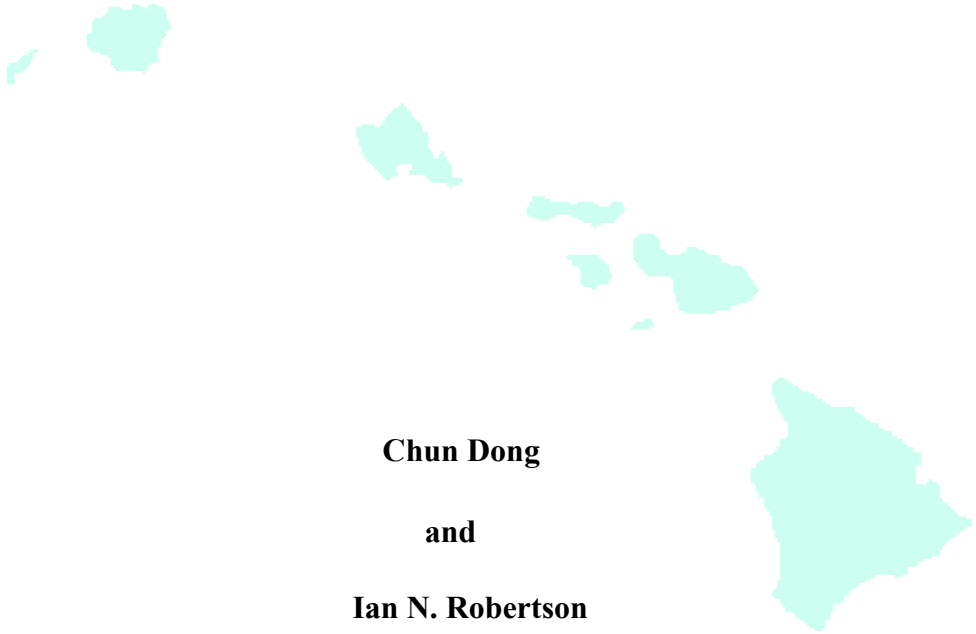

Chun Dong

and

Ian N. Robertson

UNIVERSITY OF HAWAII
COLLEGE OF ENGINEERING

DEPARTMENT OF CIVIL AND ENVIRONMENTAL ENGINEERING

Research Report UHM/CE/99-04
July 1999

LONG-TERM STRUCTURAL MODELING OF THE NORTH HALAWA VALLEY VIADUCT

Chun Dong

Ian N. Robertson

Research Report UHM/CE/99-04

July 1999

ACKNOWLEDGEMENT

This report is based on a Masters Thesis prepared by Chun Dong under the direction of Ian Robertson. The authors wish to express their gratitude to Drs. H. Ronald Riggs and Craig Newtson for their effort in reviewing this report, and for their valuable comments and suggestions.

This project was supported by funds from the Federal Highway Administration and the Hawaii State Department of Transportation. This support is gratefully acknowledged.

TABLE OF CONTENTS

LIST OF FIGURES

LIST OF TABLE

CHAPTER 1

INTRODUCTION

Segmentally erected prestressed concrete box girder bridges have become a mainstay in North American highway construction. Because they meet the demand for economy and environmental sensitivity, segmentally constructed prestressed concrete box girder bridges have become very popular for medium and long span bridge structures around the world. Since their introduction in 1964, more than 360,000 lineal feet of segmental bridge have been built, with a trend toward increasing popularity (Shushkewich et al, 1998).

The H-3 Freeway is the newest portion of Hawai'i's freeway system, linking the leeward and windward sides of Oahu. One of the largest sections of the H-3 freeway is the North Halawa Valley Viaduct (NHVV), designed by Nakamura and Tyau Associates of Honolulu, Hawaii and T.Y.Lin International of San Francisco. The twin viaducts which make up the NHVV are segmental cast-in-place concrete box girder structures built by the cantilever construction method. The NHVV is described in detail in Chapter 2.

An extensive instrumentation program was initiated by the University of Hawai'i (UH) and T.Y.Lin International personnel during construction of unit 2 of the inbound viaduct in 1994. Four of the spans in this unit were instrumented for long-term monitoring as described in Chapter 3. The focus of this study is the long-term performance of the NHVV after four years of monitoring.

In order to determine the concrete material properties in the NHVV, including creep and shrinkage, extensive testing was performed by Construction Technology Laboratory (CTL) in Skokie, Illinois. The testing and resulting material properties are described in Chapter 4.

Chapter 5 presents the application of SFRAME to the North Halawa Valley Viaduct (NHVV). SFRAME is a structural analysis program specifically developed for the time-dependent analysis of segmentally erected prestressed concrete plane frame bridge structures (Ketchum, 1986). T.Y.Lin International used SFRAME during the original analysis and design of the NHVV. Section 5.2 describes the operation of the SFRAME program. Section 5.3 and 5.4 outline the modeling of the NHVV culminating in the "T.Y.Lin As-built model". Finally, section 5.5 describes the development of concrete material properties for use in this study, based on the CTL test data of the concrete used in the NHVV.

The results of various SFRAME models are compared with measured viaduct deflections in Chapter 6. Neither the T.Y.Lin As-built or the initial laboratory models were able to predict the long-term structural response for all spans of the viaduct. Inclusion of creep and shrinkage predictions based on short-term laboratory tests improved the predictions from the initial laboratory model, but the results are still inadequate as predictors of the structural response.

Consequently, it is necessary for the designer to estimate likely ranges for each of the critical parameters and develop upper and lower envelopes which can be anticipated to encompass any potential structural response. Chapter 7 presents the development of envelopes for the NHVV.

Finally, conclusions are presented in Chapter 8.

CHAPTER 2

NORTH HALAWA VALLEY VIADUCT PROJECT

2.1 Introduction

The H-3 Freeway is the newest portion of Hawaii's freeway system, linking the leeward and windward sides of Oahu. The project is the largest ever undertaken by the State of Hawaii Department of Transportation, with a cost totaling approximately one billion dollars.

2.2 Project Description

The H-3 Interstate Highway starts from the Halawa Valley Interchange in Honolulu, Hawaii and ends at the Marine Corps station in Kaneohe, Hawaii (Figure 2.1).

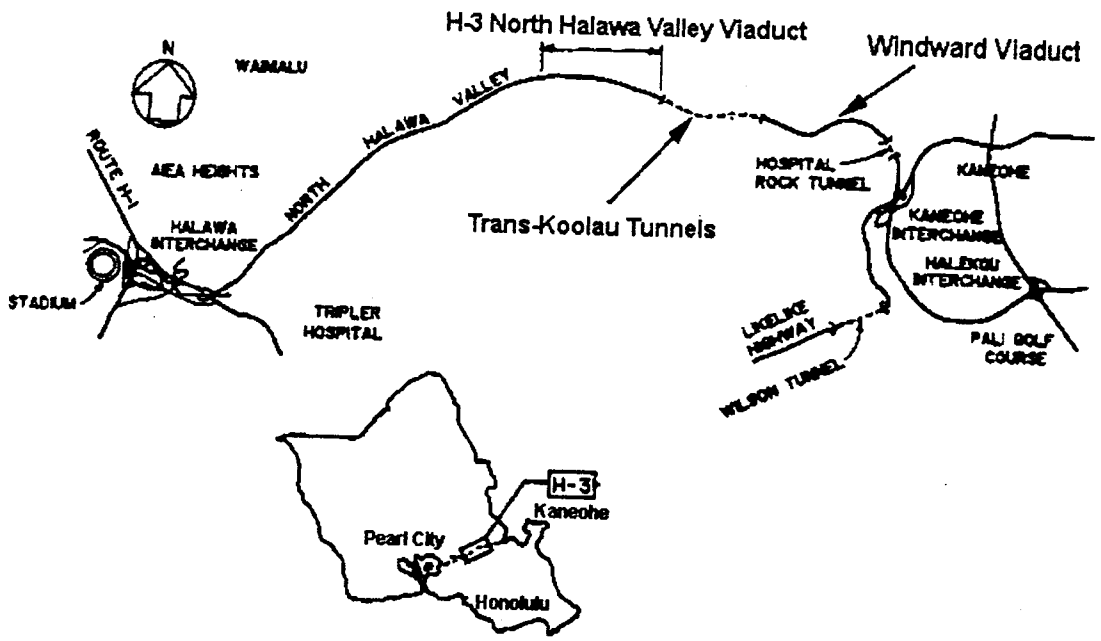

Figure 2.1: H-3 freeway location

Three of the major structures making up the H-3 freeway are the trans-Koolau tunnel, the Windward Viaduct and the North Halawa Valley Viaduct (Figure 2.2).

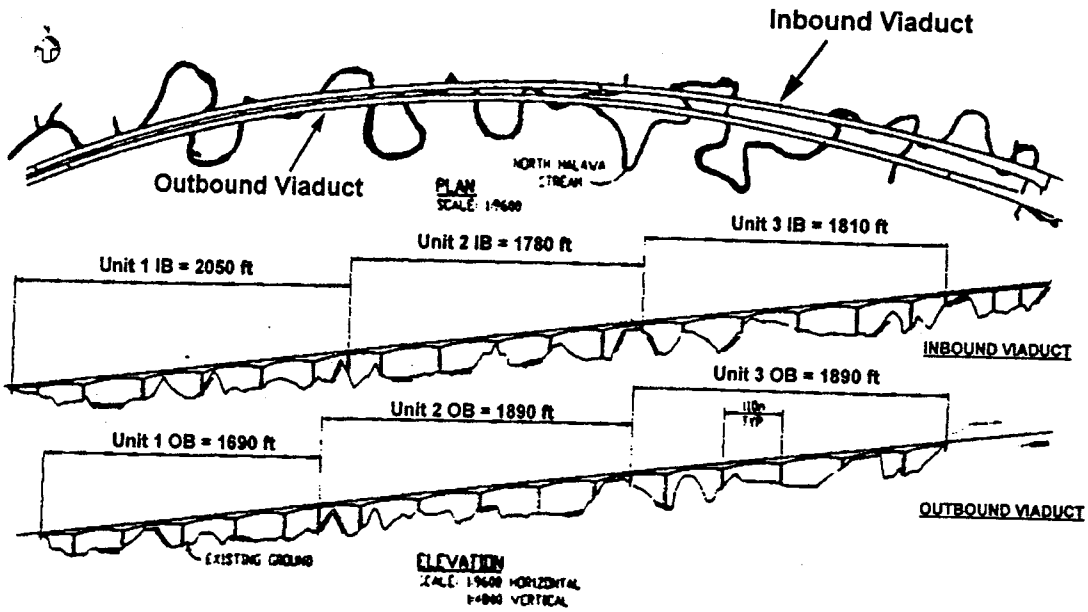

Figure 2.2: North Halawa Valley Viaduct

The North Halawa Valley Viaduct (NHVV) was designed by Nakamura and Tyau Associates of Honolulu, Hawaii, and T.Y.Lin International of San Francisco. The twin viaducts are segmental cast-in-place post-tensioned concrete single-cell box girders. They were constructed by the cantilever method using formwork supported by an overhead gantry.

The twin viaducts each consist of three independent units. Each unit has six spans supported by seven piers. The second unit of the inbound viaduct (Unit 2IB) was instrumented and monitored in this project. Seven sections of Unit 2IB were selected for instrumentation to provide an adequate representation of the viaduct behavior.

Unit 2 of the inbound viaduct is 1782 feet in length and consists of 7 piers and 6 spans. The span length varies from 200 feet to 360 feet. There are two fixed piers near the middle of the unit, while the other pier supports are slide bearings. The slide bearings allow for creep, shrinkage, and thermal expansion and contraction. The dimensions of the cast-in-place box girder are as follows: deck widths are 41 feet over a 23 feet wide single cell box. Segment depth varies from 8 feet at mid-span to 18 feet at piers. Segment lengths are typically 24 feet with closure segments varying up to 28 feet (Figure 5.2).

2.3 Construction description

The construction method for the prestressed segmental box girder bridge was developed by Kiewit Pacific Company in Honolulu, Hawaii, and VSL Corporation in Campbell, California. The superstructure was constructed using a cast-in-place cantilever construction method. Box girder segments were cast-in-place by means of a form-traveler assembly. Using a steel truss (gantry truss), the form-travelers were supported and positioned, without dismantling, from pier to pier (shown in Figure 2.3). The cast-in-place option was selected over a precast segmental option due to environmental constraints, limited service road access, and the long distance between potential casting yards and the construction site.

Figure 2.3: North Halawa Valley Viaduct under construction

A major advantage of the cantilever construction method is elimination of shoring, which can amount to nearly 40 percent of the construction cost. Using the cantilever construction method, the structure is self-supporting at all times during construction. Construction hazards are reduced since wash-out of shoring in potential flooding terrain is avoided (Ingham et al,1995).

The bridge structure was redesigned by the contractor to reduce the number of cast-in-place segments, thus increasing productivity in the construction process. The segment lengths were increased from 21 to 24 feet, and the closure length from 8 to a maximum of 28 feet. To further increase productivity in the construction process, high strength concrete was used so as to achieve a 3500 psi compressive strength overnight. The forms

were thermally insulated to retain the heat of hydration and accelerate strength gain. This allowed earlier post-tensioning and stripping of the forms (Ingham et al,1995).

Ready-mix concrete supplied by Hawaiian Cement Company was used for all construction in this project. The batch plant is located in Halawa Valley, providing direct and short time delivery. The same concrete mix design was used throughout the construction of Unit 2IB. This mixture is shown in Table 2.1.

Table 2.1: Hawaiian Cement Ready-mix Concrete Composition

MATERIAL	CEMENT	SAND	NO.4	3F(w)	3/8(w)	WATER	TOTAL
SOURCE	HAW'N	CIP-EWA	HALAWA	HALAWA	HALAWA	CITY	
SSD WTS.	715	1244	0	1014	676	293	3939
SPGR.	3.15	2.52	2.65	2.65	2.65	1	
ABSVOL/CF	3.64	7.91	0	6.13	4.09	4.65	26.42
MOIST %	6.5	4.5	4.5	5			
ABSORP %	4	5	4	4			
CORRECT %	2.5	-0.5	0.5	1			
ADJ. WTS/#	31	0	5	7	-43		
BATCH WTS/LBS	715	1275	0	1019	683	247	3939

CHAPTER 3

INSTRUMENTATION PROJECT

3.1 Introduction

An extensive instrumentation program was initiated by the University of Hawai'i (UH) and T.Y. Lin personnel during construction of unit 2 of the inbound viaduct. Four of the spans in this unit were instrumented for long-term monitoring as shown in Figure 3.1. The following are brief descriptions of selected instruments specifically referred to in this study. A full description of all instrumentation systems, including installation and monitoring, is presented by Lee and Robertson (1995).

3.2 Deflection measurement

The vertical deflected shape of the viaduct was recorded by a number of methods. During the construction, the deflected shape of the cantilevers and backspans were monitored by optical surveys. After completion of the construction, a base-line system was installed in each of the four instrumented spans. Tiltmeters were also installed in the box girder above the piers at each end of the instrumented spans.

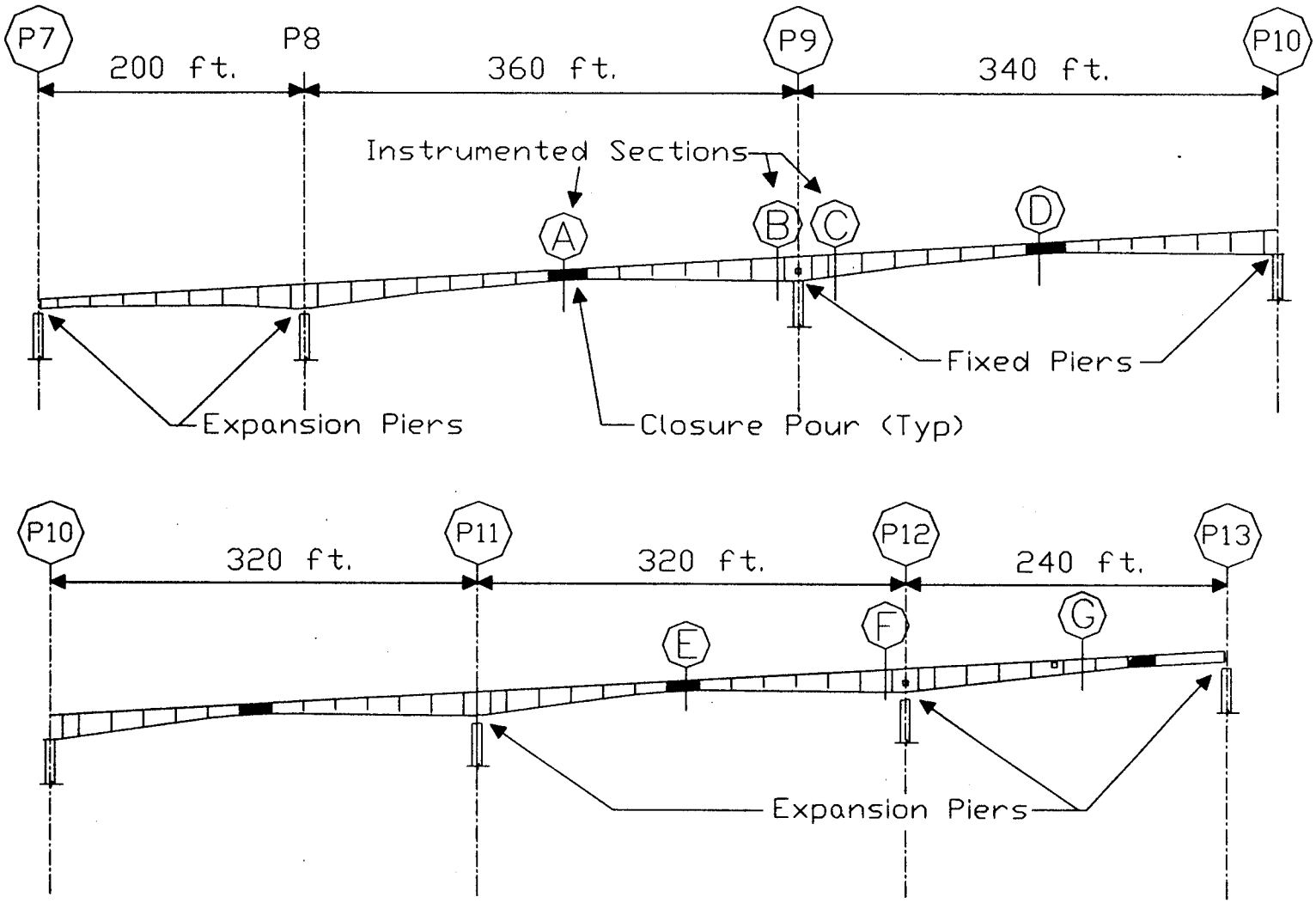

Figure 3.1: Unit 2 Inbound Viaduct

3.2.1 Base-line system

3.2.1.1 Description

A taut-wire base-line system was installed in all four instrumented spans for vertical deflection measurements. This system consists of a high-strength piano wire strung at constant tension inside the box girder from one pier to the next to act as a reference line.

The base-line system was chosen for its simplicity of installation and reading, economy, excellent short and long term stability, and accuracy.

3.2.1.2 Layout and installation

Four spans were equipped with base-line systems. The instrumented spans were from pier 8 to pier 9, pier 9 to pier 10, pier 11 to pier 12, and pier 12 to pier 13. The deflection measurements were taken at locations shown in Figures 3.2 and 3.3.

The base-line system consists of a piano wire as a reference line, two end brackets (live and dead), base plates, and a caliper. The arrangement is shown schematically in Figure 3.4. The number 8 piano wire was stressed to approximately 80% of its breaking strength to avoid any appreciable variations in the catenary shape of the free length of the piano wire. To create this tension in the piano wire, one end of the wire is fixed (Figure 3.5) while the other end runs over a pulley and supports an 80 pound weight (Figure 3.6). The wires were coated with Linseed oil to resist corrosion.

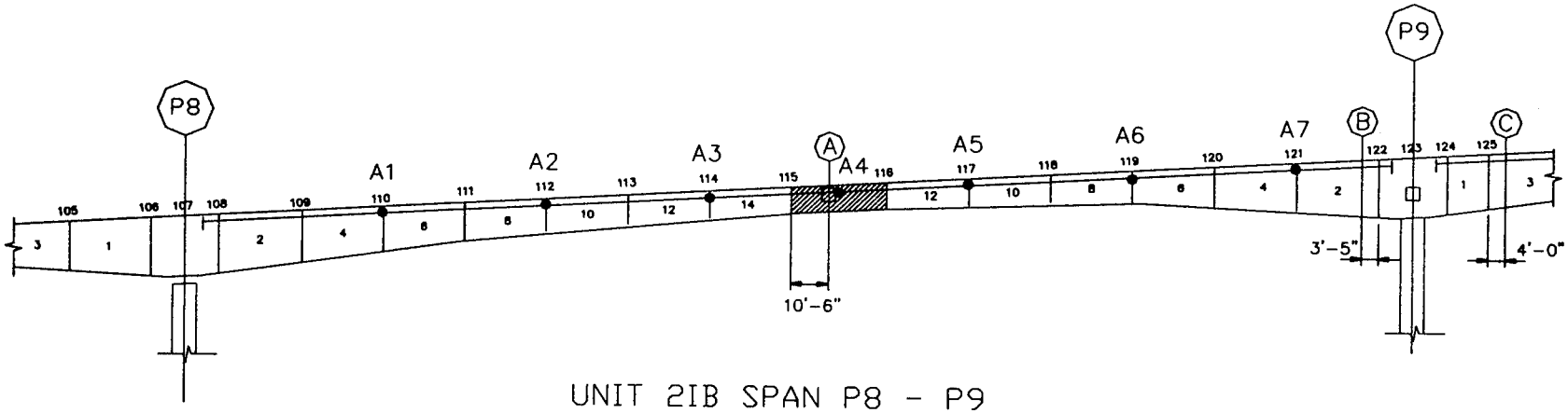

UNIT 2IB SPAN P8 - P9

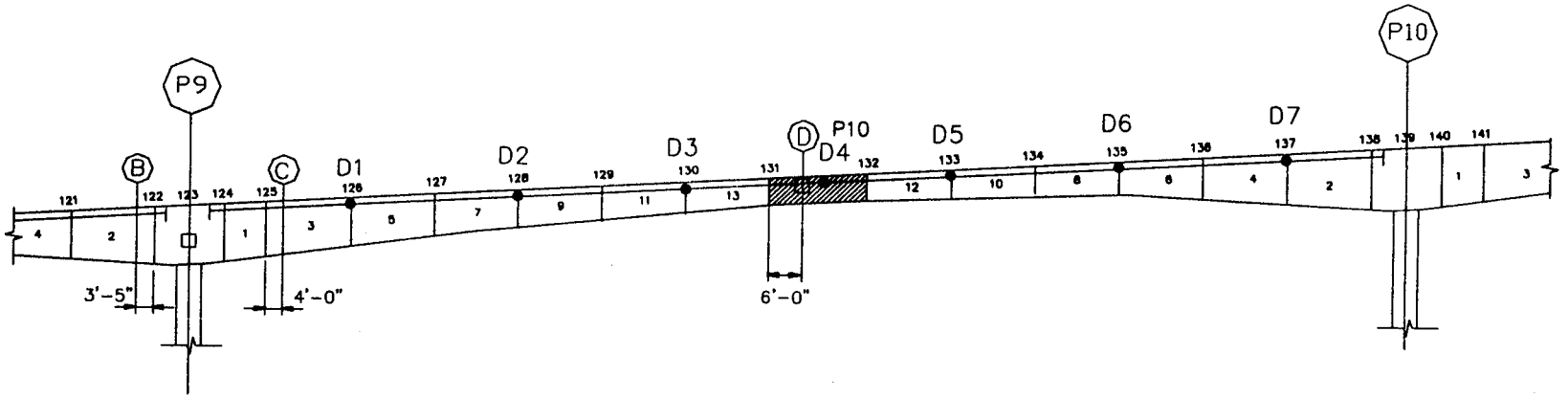

UNIT 2IB SPAN P9 - P10

Figure 3.2: Measurement stations for spans between piers 8 and 10

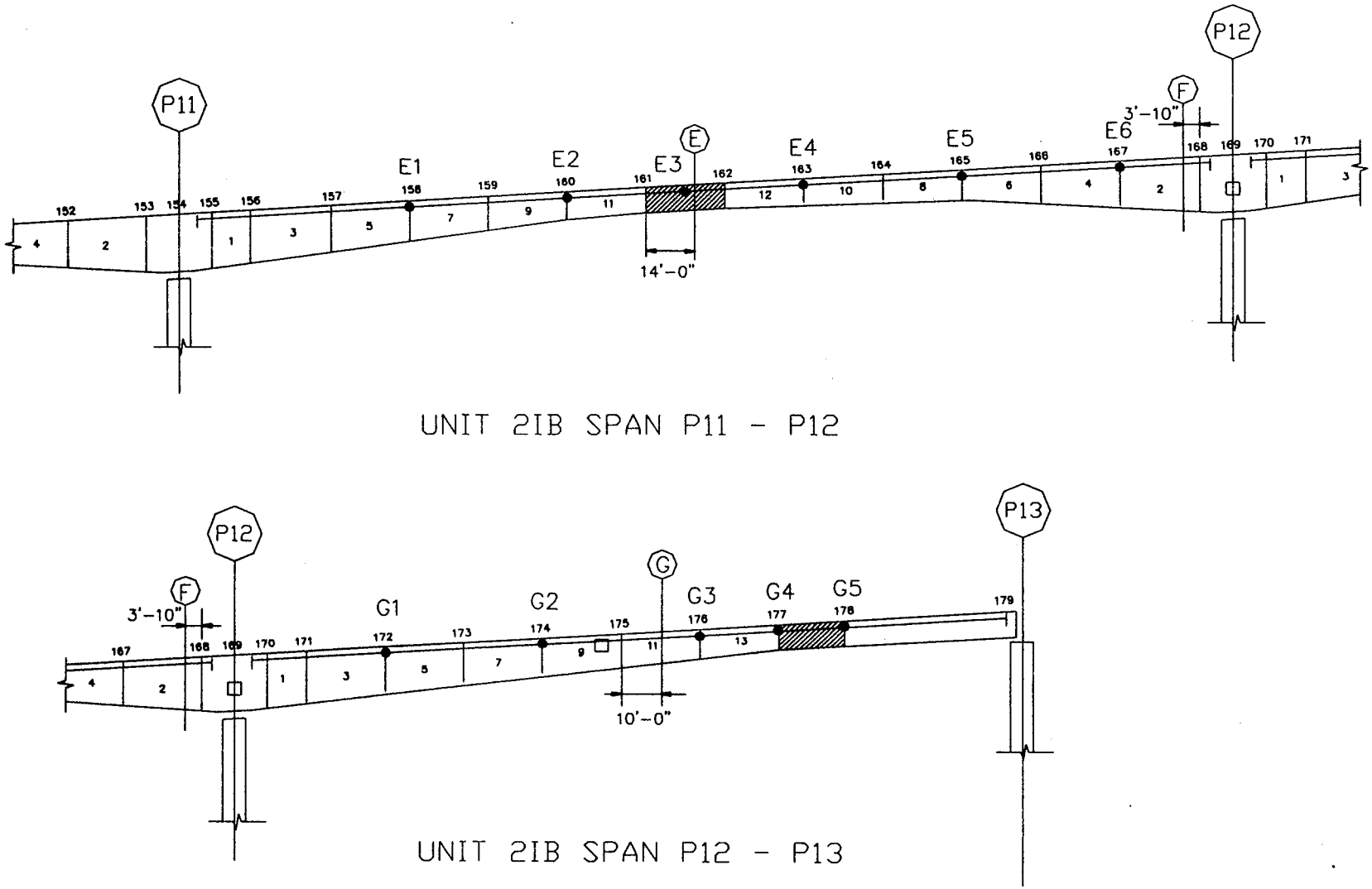

Figure 3.3: Measurement stations for spans between piers 11 and 13

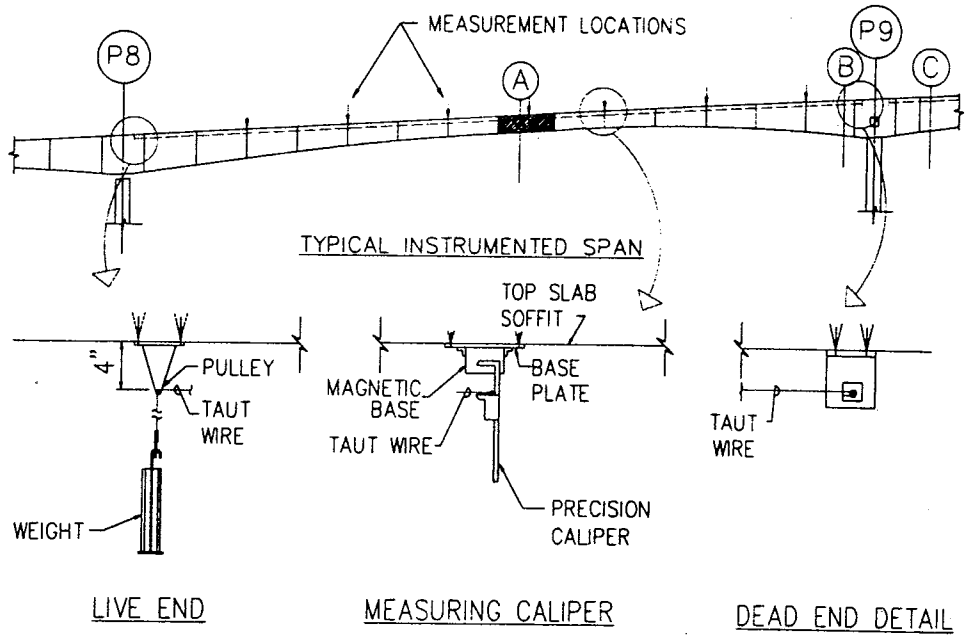

Figure 3.4: Base-line deflection measurement system

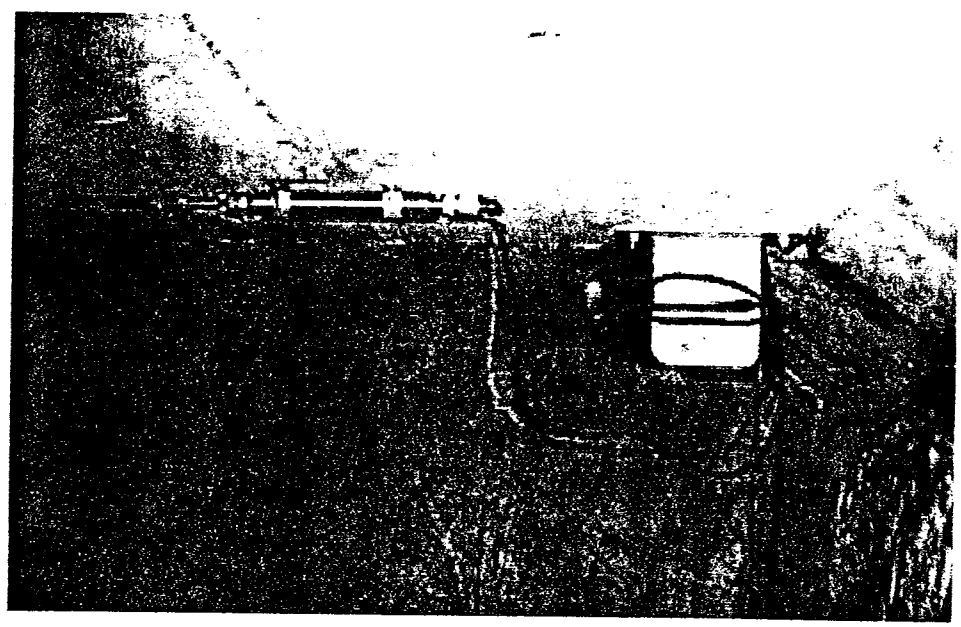

Figure 3.5: Base-line fixed end

Figure 3.6: Base-line tension end

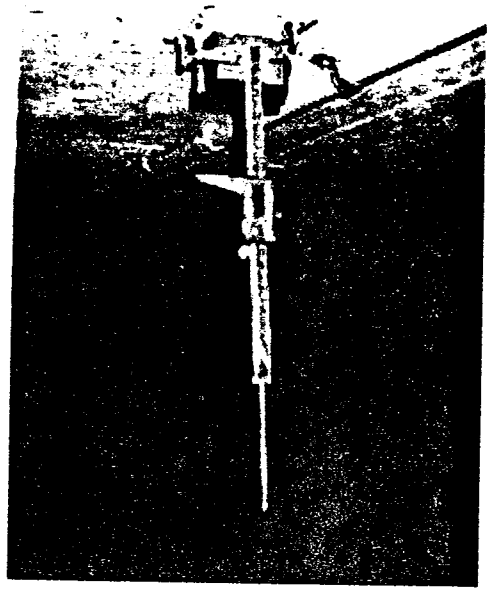

Figure 3.7: Base-line caliper

Note that in a plan view the piano-wire represents a straight line in a curved viaduct. The end brackets were positioned such that the wire came as close as possible to the centerline of the box girder at midspan. To do this, the end brackets were positioned to the North of the girder centerline at each end of the span. In addition, construction access openings in the top slabs near the ends of certain spans had to be avoided, resulting in further offsets of the end brackets in these spans. The exact locations of the end brackets are given in Lee and Robertson (1995).

Deflection measurement points along the span are generally located at alternate construction joints, and at midspan. Steel base plates were installed on the soffit of the

top slab at each of these locations using expansion anchor bolts. Small angles were welded to each base plate as guide bars. This ensures consistent positioning of the measuring caliper on the base plate.

The measuring caliper is a modified 8 inch range Mitutoyo digital caliper (Figure 3.7). The caliper is attached to a magnetic base, which is used to secure its position on the base plate. The magnetic base is equipped with an on/off switch allowing easy attachment to and removal from the base plates. Once the magnetic base is secured to a base plate, the caliper is used to read the location of the piano-wire relative to the top slab of the viaduct box. After initial readings are taken at each of the measurement locations, subsequent readings record the vertical deflection of the box girder relative to the ends of the span.

3.1.2 Optical surveys

During construction, optical surveys were made on the viaduct top surface to ensure construction progressed at the correct elevations. Subsequent to construction, optical surveys have been undertaken for barrier elevation and topping elevation purposes. These optical surveys were used to confirm the base-line observations.

3.2.3 Tiltmeters

3.2.3.1 Description

For support rotation measurement, Applied Geomechanic Instruments (AGI) Uniaxial Tiltmeters Model 800 were installed in the box girder above all six piers from pier 8

through pier 13 (Figure 3.8). These tiltmeters incorporate a high-precision electrolytic tilt transducer as the internal sensing element. They measure rotational movement with respect to the unchanging vertical gravity vector.

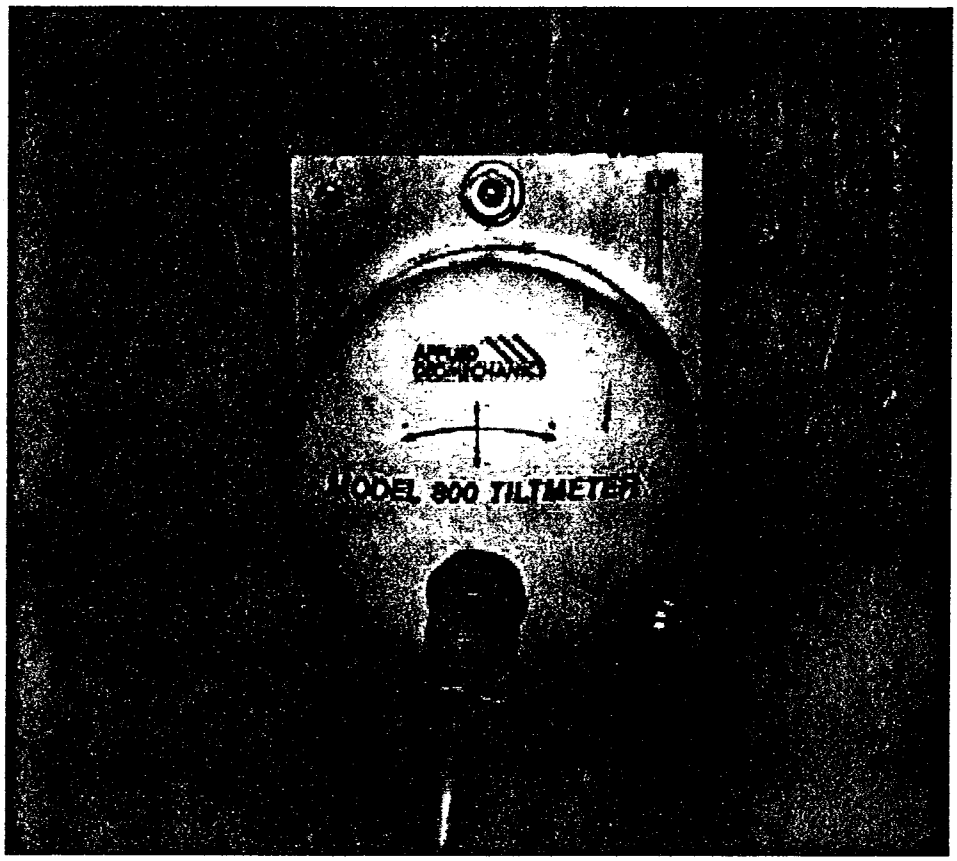

Figure 3.8: AGI uniaxial tilmeter

3.2.3.2 Layout and installation

Tiltmeters were installed at piers 8, 9, 10, 11, 12 and 13. They were mounted on a smooth vertical surface. All of the tiltmeters were installed on South facing vertical surfaces except at pier 12, where the tiltmeter faces North.

3.3 Span shortening measurements

Measurement of the overall shortening of each instrumented span provides a valuable check of the behavior observed at the localized instrumented sections.

3.3.1 Extensometers

To measure the overall shortening of the box girder, extensometers were installed in the four instrumented spans as shown in Figure 3.9.

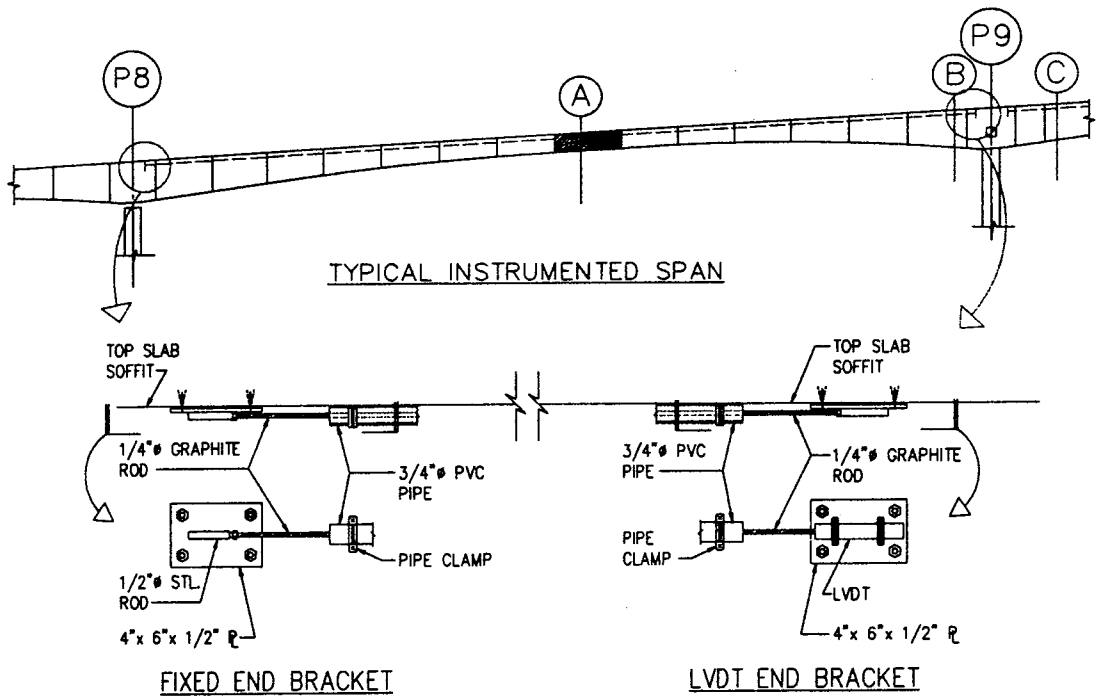

Figure 3.9: Span extensometer details

Each extensometer consists of a series of graphite rods (¼ inch diameter by 20 feet long) spliced together to span from pier to pier inside the box girder. The graphite rods are connected with rigid couplers and inserted into a ¾ inch diameter PVC pipe attached to

the underside of the girder top slab. One end of the rod is fixed, while the other end is coupled to a Linear Variable Displacement Transducer (LVDT). The relative displacement of the two ends of the extensometer is measured by the LVDT. The LVDT's were manufactured by Geokon and operate on the vibrating wire principle. One of the LVDT's has a six inch stroke, while the others have two inch strokes. Once this limit is reached, they are repositioned so as to continue monitoring the span shortening.

Extensometers were installed in all four instrumented spans, that is, between pier 8 and pier 9, pier 9 and pier 10, pier 11 and pier 12, and pier 12 and pier 13, as shown in Figure 3.1.

3.4 Tendon prestress – load cells

3.4.1 Description

The load cells used to measure the tendon forces were designed and manufactured by Construction Technology Laboratories. They are cylindrical load cells with a 700 kip compressive capacity. The load cells were placed directly below the stressing anchor block prior to stressing of the tendons as shown in Figure 3.10.

3.4.2 Layout and installation

Six span tendons were fitted with load cells. At each of the long span conditions from pier 8 to pier 9 and pier 9 to pier 10, two span tendons were fitted with load cells, one in each stem as shown in Figure 3.11. One of these tendons was a long tendon while the

other was a short tendon. The remaining two load cells were installed on span tendons in the spans from pier 11 to pier 12 and pier 12 to pier 13 as shown in Figure 3.12.

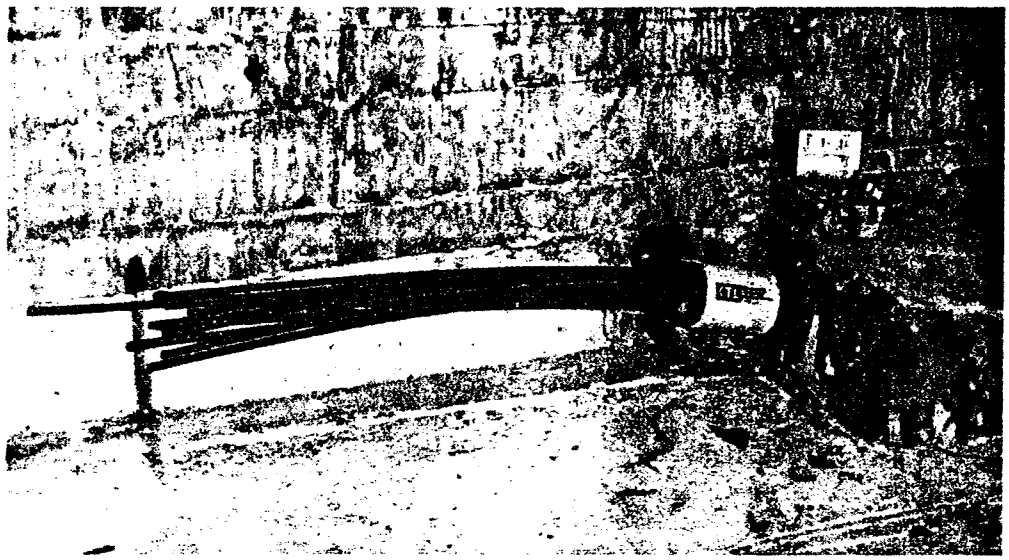

Figure 3.10: Prestress tendon load cell

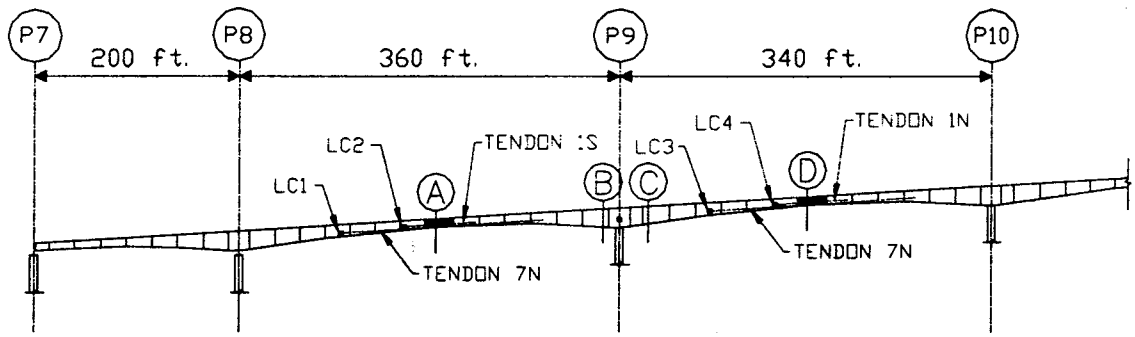

Figure 3.11: Tendon load cell locations – P8 to P10

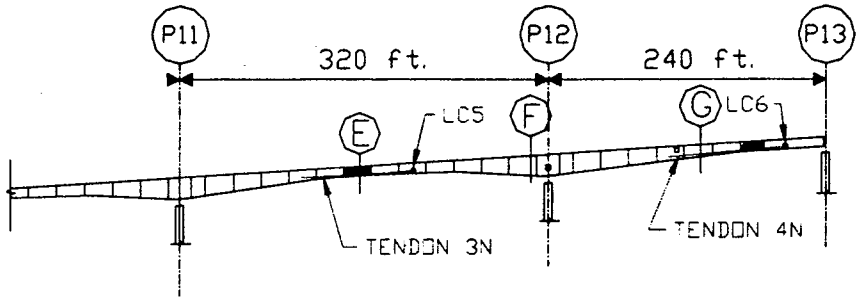

Figure 3.12: Tendon load cell locations – span P11 to P13

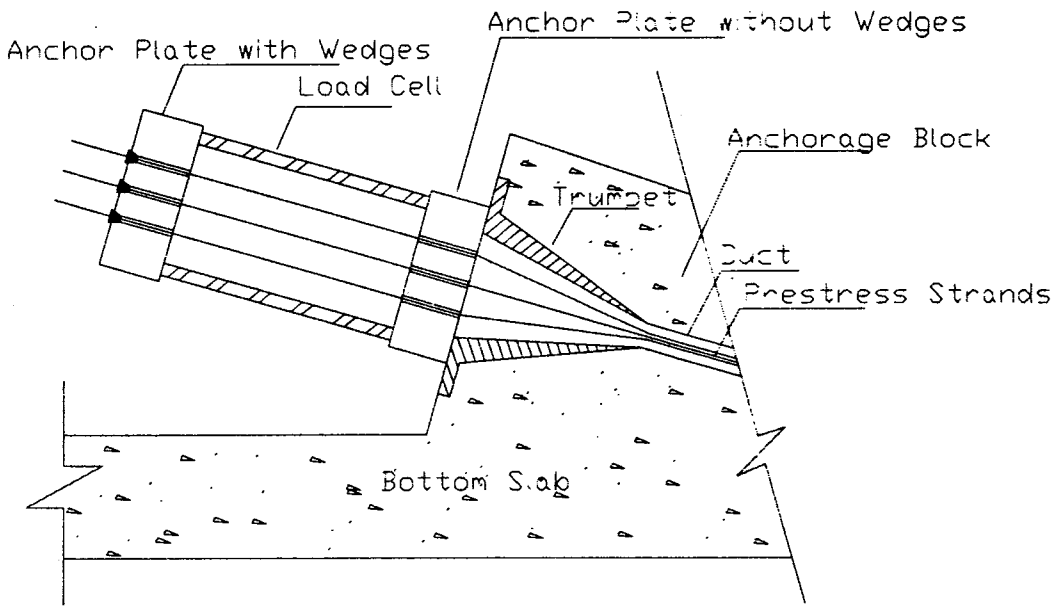

Figure 3.13: Load cells 1 & 2

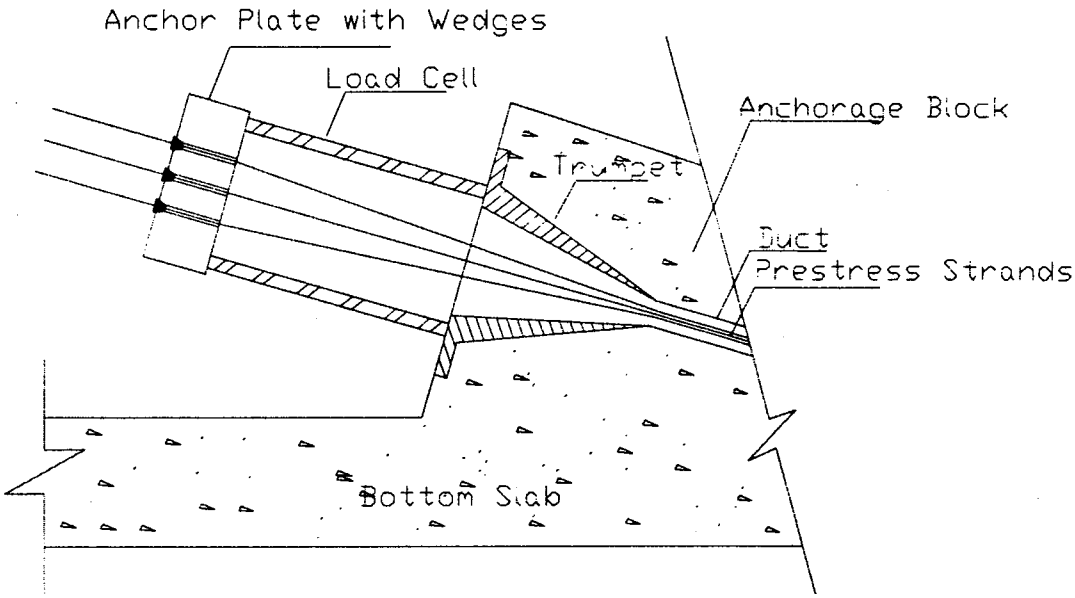

Figure 3.14: Load cells 3, 4, 5 and 6

The tendons monitored by load cells were left ungrouted. They are protected from corrosion by means of Dichan 100, a powder corrosion inhibitor.

There are two different placements of the load cells as shown in Figures 3.13 and 3.14. For load cells 1 and 2, an anchor plate without wedge was placed between the load cell and the trumpet embedded in the anchorage block. During stressing of these tendons, it was noted that the load cell readings were substantially lower than the anticipated prestress. It was assumed that the friction at the first anchor plate may have caused the additional prestress losses for load cells 1 and 2. Therefore, subsequent load cells were installed without the first anchor plate (Figure 3.14). Discrepancies were still noted between the applied prestress and the load cell readings leading to a separate study of the prestressing ram and load cells by Henry Russell and Scott Hunter (Russell and Hunter, 1995).

CHAPTER 4

CONCRETE MATERIAL PROPERTIES

4.1 Introduction

Concrete is unique among structural materials in that it undergoes complex physical and chemical changes over time, resulting in deformation and constitutive properties which are time dependent under practical service conditions. These time dependent phenomena in concrete are some of the most significant factors influencing structural behavior. When concrete is subjected to a constant load, it not only experiences an immediate elastic deformation, but will also experience a continual inelastic deformation, or time-dependent deformation. In addition, a concrete specimen experiences volume changes throughout its life even without the application of load. The combination of time-dependent deformations due to application of load and the deformations occurring independently of load are together known as creep and shrinkage. Creep strain, or deformation per unit length, is an inelastic, time-dependent strain produced by sustained stress, while shrinkage strain is a reduction of volume, independent of stress, caused primarily by the loss of water during the drying process.

4.1.1 Creep

The stress-strain response of concrete depends upon the time history of loading. If the stress is held constant for some length of time, the strain increases, a phenomenon referred to as creep. The amount of creep that a particular concrete will exhibit is difficult

to estimate accurately unless tests are conducted to determine the creep characteristics. Many designers do not have the time or the budget to afford such tests to obtain long-term results. However, short term test can be used to improve creep predictions substantially (Durbin and Robertson, 1998). Without specific tests, accuracies of better than $\pm 30\%$ should not be expected. Even with short term test results, the actual creep under field conditions may still vary by $\pm 20\%$.

4.1.2 Shrinkage

Basically, there are two types of shrinkage: plastic shrinkage and drying shrinkage. Plastic shrinkage occurs during the first few hours after placing fresh concrete in the forms. Exposed surfaces such as floor slabs are more easily affected by exposure to dry air because of their large contact surface. Drying shrinkage, on the other hand, occurs after the concrete has already attained its final set and a good portion of the chemical hydration process in the cement gel has been accomplished. Shrinkage is greatest at exposed surface areas of specimens and decreases towards the interior of the specimen.

4.2 Effects of Creep and Shrinkage

The effects of creep and shrinkage on concrete structures can be dramatic. Creep can significantly change the stress distributions in a reinforced concrete specimen. Creep causes a redistribution of stresses between the concrete and the reinforcing bars. As concrete creeps, compatibility requires that the concrete and steel strains are identical.

There is a rearrangement of local equilibrium, and load is transferred from the concrete to the steel.

Shrinkage induces tension in concrete, which may result in cracks. These cracks may be difficult to control and increase expenses by requiring additional steel. The cracks create durability and serviceability problems, and may also reduce shear strength.

In summary, creep and shrinkage have a significant effect on structural behavior and performance. In some instances, creep may be detrimental, causing undesired deformations and deflections. In other cases, it may be beneficial, reducing stress concentrations due to imposed deformations such as support settlement, shrinkage and thermal gradients.

4.3 Concrete properties in the NHVV project

In order to establish the material properties of the concrete used in the viaduct, concrete samples were taken during pouring of each instrumented section. The following concrete material properties were determined using concrete samples:

Compressive Strength,

Modulus of Elasticity,

Coefficient of Thermal Expansion, and

Creep and shrinkage.

These tests were all performed by Construction Technology Laboratories (CTL) at Skokie, Illinois. Tests were performed or initiated at concrete ages of 3, 28 and 90 days for samples taken from each of the seven instrumented sections. Concrete age is the number of days after the section was poured.

4.3.1 Concrete sample collection

Concrete samples were collected during pouring of each instrumented section. Standard 6-inch diameter by 12-inch long concrete cylinders were used for all tests. Thirty-three cylinders were collected at each section and shipped to CTL. All samples were made in plastic cylinder molds in accordance with ASTM C192 procedures. The molds were capped to ensure sealed conditions during shipping of the cylinders to CTL. The samples were collected at ten different locations in the cross section and throughout the pour to obtain a complete representation of the concrete in the instrumented segment. The sample locations are bottom slab middle (BSM), south stem bottom (SSB), south stem middle (SSM), south stem top (SST), north stem bottom (NSB), north stem middle (NSM), north stem top (NST), top slab south (TSS), top slab north (TSN), and top slab middle (TSM), as shown in Figure 4.1.

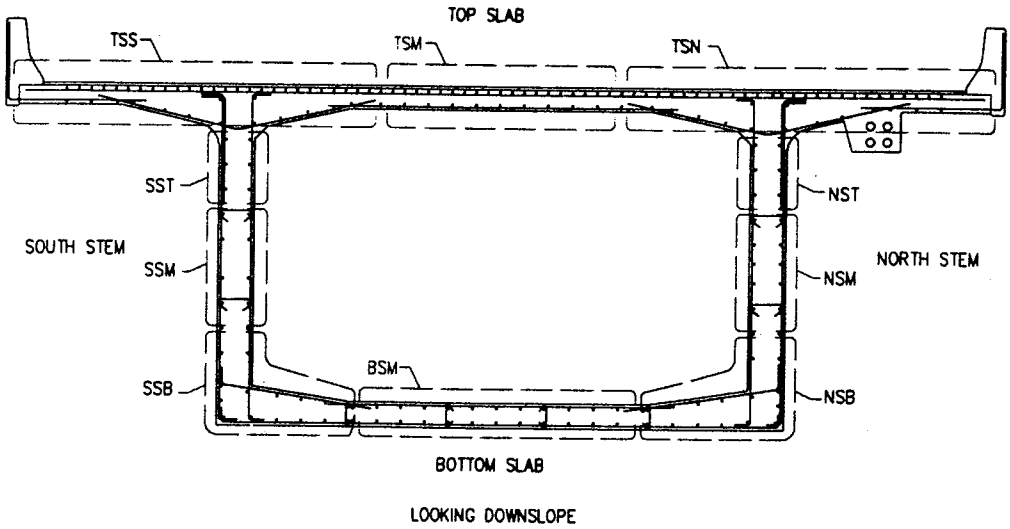

Figure 4.1: Concrete test cylinder sampling locations

4.3.2 Concrete sample shipping

The day after the pour, eleven of the cylinders were airfreighted to CTL so as to arrive in time for 3-day tests. The 28 and 90-day cylinders were shipped by surface delivery so as to arrive in time for testing. All cylinders were shipped in the capped plastic molds to preserve 100 percent moisture conditions. They were packed individually in styrofoam filled cardboard boxes. No damage was noted on any of the cylinders on their arrival at CTL.

4.3.3 Concrete testing results

4.3.3.1 Compressive strength

The compressive strength tests were performed in accordance with ASTM C39. Table 4.1 presents the test results at 3, 28 and 90 days for each section. Each result is an average of three concrete cylinders.

Table 4.1: Compressive Strength Test Results (psi)

Section	3 Days	28 Days	90 Days
A	4260	6140	7700
B	3780	6770	7910
C	3780	6740	7650
D	4290	6640	7630
E	4210	6530	7430
F	3880	5850	7060
G	3830	5990	6510
Average	4004	6380	7413
Standard Deviation	237	379	478

4.3.3.2 Modulus of elasticity

The modulus of elasticity tests were performed in accordance with ASTM C469. Table 4.2 shows the test results at 3, 28 and 90 days for each section. Each result is an average of two concrete cylinders.

Table 4.2: Modulus of Elasticity Test Results (psi)

Section	3 Days	28 Days	90 Days
A	3.07×10^6	3.51×10^6	3.93×10^6
B	3.23×10^6	3.98×10^6	3.93×10^6
C	3.23×10^6	3.54×10^6	3.95×10^6
D	3.21×10^6	3.59×10^6	4.12×10^6
E	3.27×10^6	3.81×10^6	3.54×10^6
F	3.48×10^6	3.57×10^6	3.88×10^6
G	3.05×10^6	3.45×10^6	3.58×10^6
Average	3.22×10^6	3.64×10^6	3.85×10^6
Standard Deviation	0.142×10^6	0.189×10^6	0.210×10^6

4.3.3.3 Coefficient of thermal expansion

The coefficient of thermal expansion tests were performed in accordance with CRD C39. Tables 4.3 and 4.4 illustrate the test results at 3, 28, and 90 days at each section, per degree Fahrenheit and per degree Celsius respectively. Each result is an average of three concrete cylinders.

Table 4.3: Coefficient of Thermal Expansion Test Results (10^{-6} per ° F)

Section	3 Days	28 Days	90 Days
A	5.55	4.86	5.38
B	4.80	4.77	5.23
C	6.04	4.86	5.52
D	4.09	5.34	4.34
E	3.85	4.10	6.53
F	3.92	4.21	4.06
G	3.78	4.34	6.24
Average	4.58	4.64	5.33
Standard Deviation	0.91	0.44	0.90

Table 4.4: Coefficient of Thermal Expansion Test Results (10^{-6} per ° C)

Section	3 Days	28 Days	90 Days
A	9.99	8.75	9.68
B	8.64	8.59	9.41
C	10.87	8.75	9.94
D	7.36	9.61	7.81
E	6.93	7.38	11.75
F	7.06	7.58	7.31
G	6.80	7.81	11.23
Average	8.24	8.35	9.59
Standard Deviation	1.64	0.79	1.63

4.3.3.4 Creep strain

At CTL laboratories, creep and shrinkage tests were conducted following the recommendations of ASTM C512. The laboratory tests were performed on concrete samples from each of the seven instrumented sections. For each section, three creep frames were loaded, one each at 3 days, 28 days and 90 days age after pouring. Each creep frame contained two concrete cylinders under load and two companion shrinkage cylinders which were not loaded.

Figures 4.2 through 4.4 present the CTL measured creep values for each creep frame along with average creep values for concrete samples loaded at 3 days, 28 days, and 90 days, respectively. The average creep plot represents the average of 14 cylinders in 7 creep frames. Creep values are expressed as specific creep (creep strain per unit stress). Table 4.5 shows the values of average specific creep and creep coefficient after one year of loading for the 3-day, 28-day, and 90-day samples:

Table 4.5: Average Creep Values after One Year of Loading

Age at Loading	Age (Days)	Days Loaded	($\times 10^{-3}$) Creep/ksi (Ave)	Creep Coeff
3 Days	368	365	1.147	3.654
28 Days	393	365	0.917	3.324
90 Days	455	365	0.686	2.633

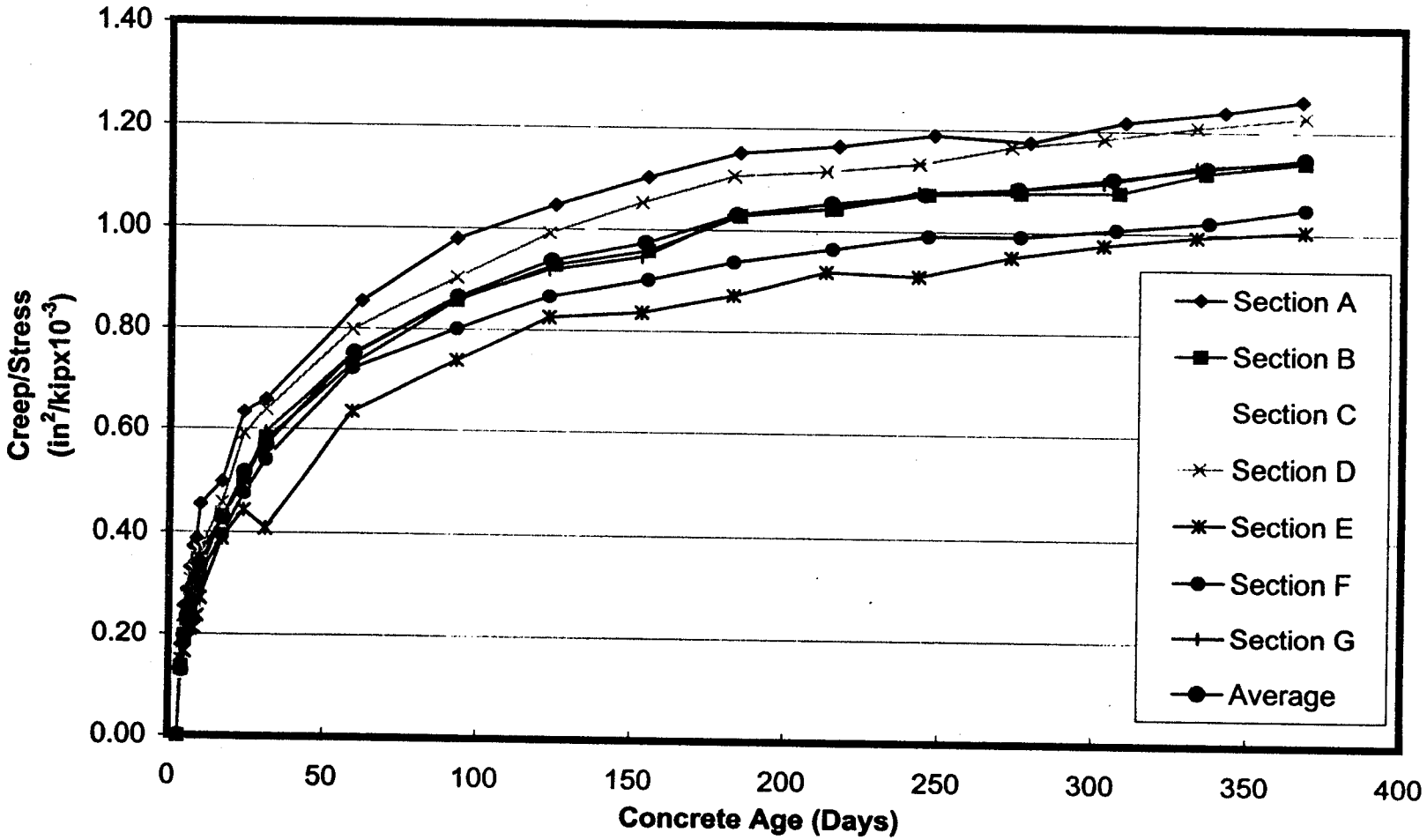

Figure 4.2: CTL 3-day creep values (50% humidity)

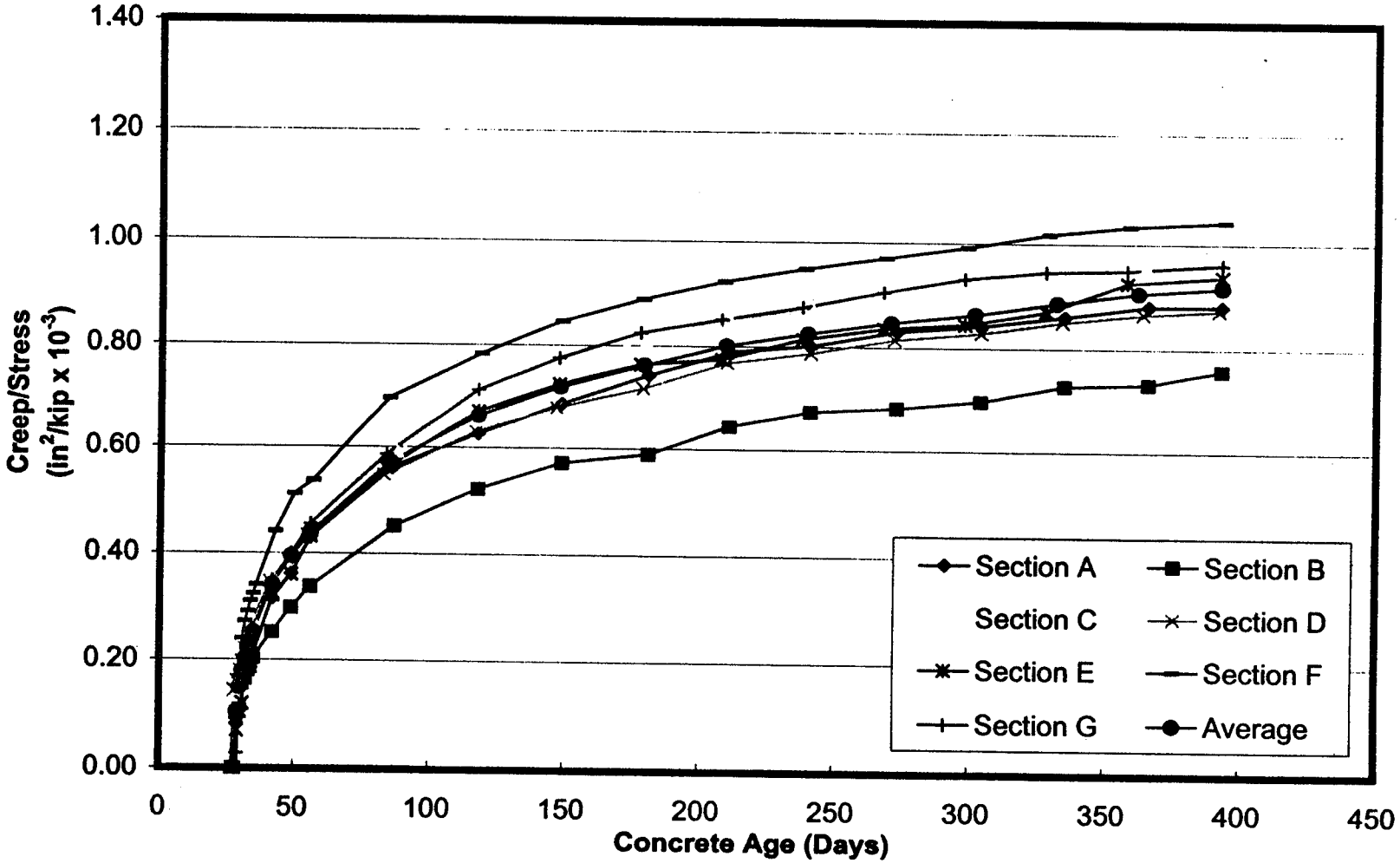

Figure 4.3: CTL 28-day creep values (50% humidity)

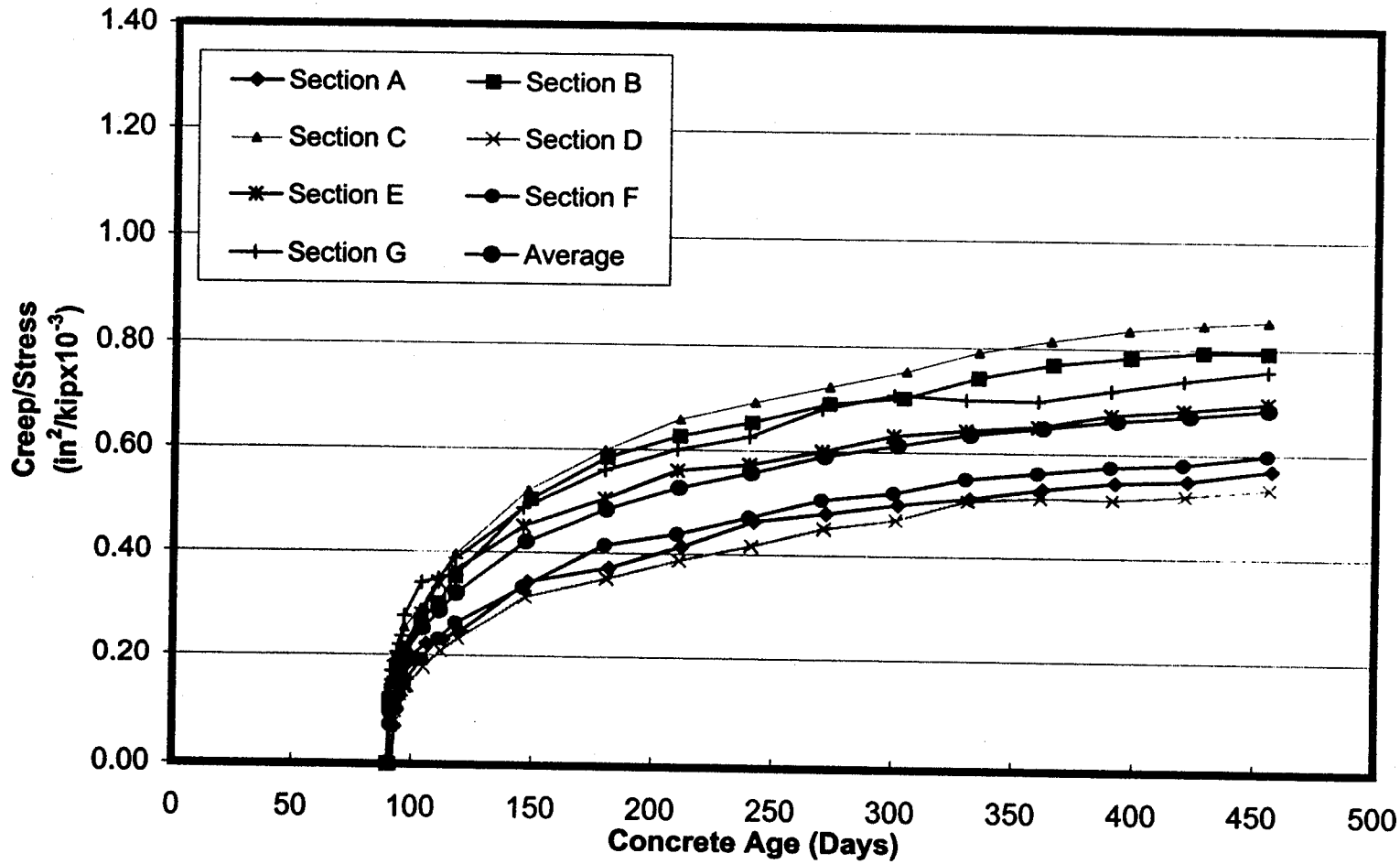

Figure 4.4: CTL 90-day creep values (50% humidity)

For a loading age of 365 days, it may be seen from table 4.5 that the average specific creep for the 3-day sample is 1.147, decreasing with increasing concrete age at loading by 20% for the 28-day sample, and 42% for the 90 day sample.

Although all concrete samples were taken from concrete having the same mix design, significant variability of creep results is noted. Figure 4.2 shows that the creep for the 3-day sample at section A is 10.1% above the average value, while section E is 12.4% below the average value. For the 28 day sample, creep at section F is 13.5% higher than the average while section B is 17.2% lower than the average as shown in Figure 4.3. In a more detailed statistical analysis by Durbin and Robertson (1998), it was shown that 95% confidence limits for the 3-day, 28-day and 90-day samples were at ± 21%, ± 25% and ± 41% from the mean, respectively.

4.3.3.5 Shrinkage strain

Figure 4.5 displays the CTL measured shrinkage for all seven sections and the average shrinkage values for the cylinders with drying from 3-day concrete age. Only these shrinkage cylinders were recorded, since the initial start of drying for the 28-day and 90-day shrinkage companion cylinders were not recorded.

Shrinkage values are expressed in microstrain. Table 4.6 lists the average shrinkage after one year of drying at 50% humidity. Durbin and Robertson (1998) show that 95% confidence limits for the 3-day shrinkage sample are ± 7% from the mean.

Table 4.6: Average 3-Day Shrinkage Values for One Year of Drying

Age at Drying	Age (Days)	Days Drying	Shrinkage ($\mu\varepsilon$)
3 Days	368	365	1045

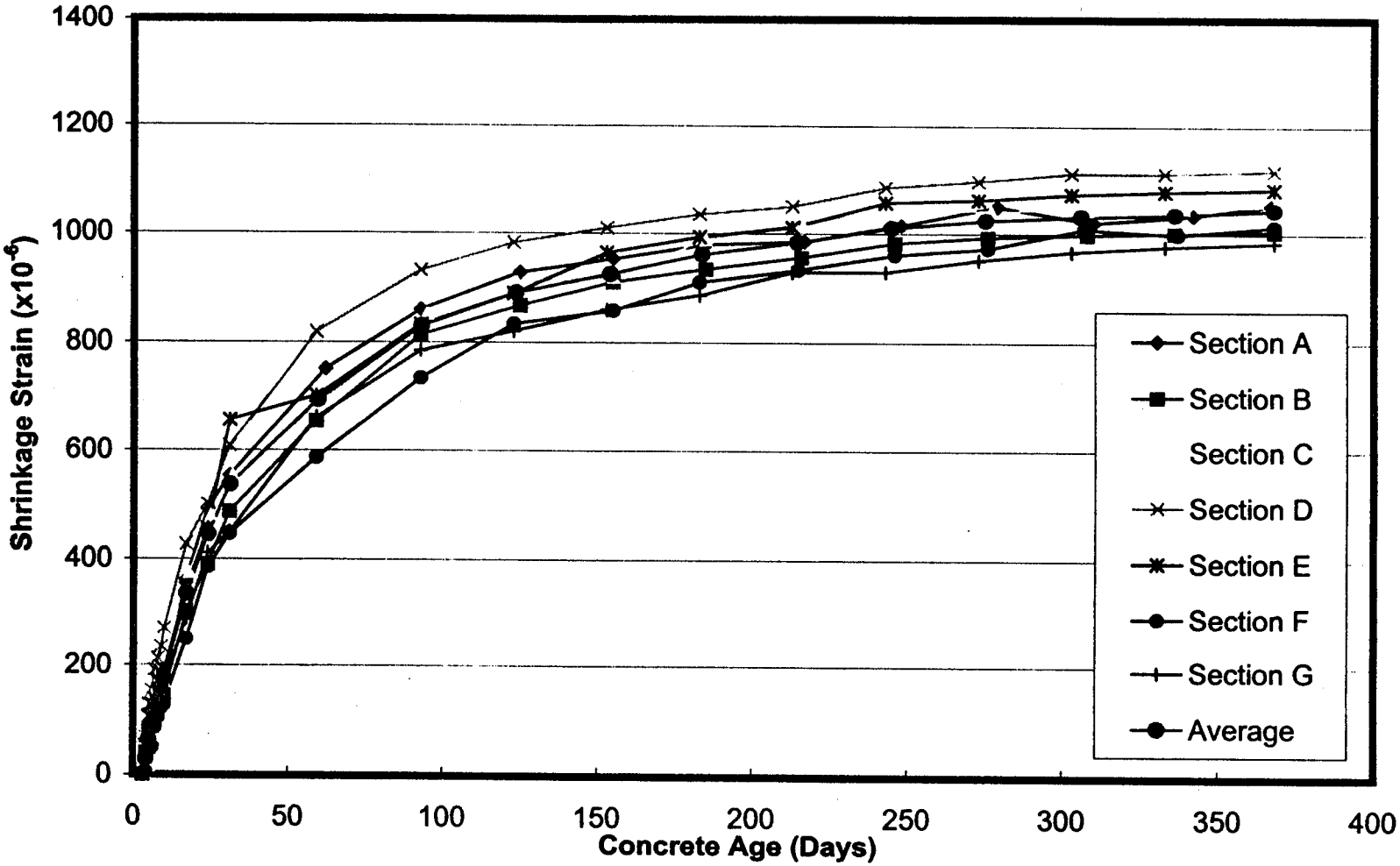

Figure 4.5: CTL 3-day shrinkage values (50% humidity)

CHAPTER 5

COMPUTER MODELING—SFRAME

5.1 Overview and introduction

SFRAME is a structural analysis program specifically developed for the time-dependent analysis of segmentally erected prestressed concrete plane frame bridge structures (Ketchum, 1986). The analysis is based on step forward integration in the time domain of a plane frame finite element model of the structure. The structural model uses beam elements to model the box girder and piers, tendon elements to model the prestressing, and special traveler elements to model moving formwork. At each solution step, a complete analysis of the finite element system is performed, providing a record of displacements in the structure. The program can build the structure in the computer using any statically feasible construction sequence for the plane frame. The program incorporates automated construction and prestressing options, and time dependent material behavior into a command structure allowing the analysis of complex segmental bridge types. The solution includes the effects of creep, shrinkage and aging of the concrete, plus friction, anchorage slip and relaxation of the prestressing steel (Ketchum, 1986).

This chapter explains the application of SFRAME to the North Halawa Valley Viaduct (NHVV). T.Y. Lin International used SFRAME during the original analysis and design of the NHVV. The model used for that analysis was revised to match the contractor's

redesign of the viaduct. It has since been updated throughout construction to accurately reflect the as-built conditions. The final model obtained from T.Y. Lin at the start of this study is a true as-built representation of the schedule of construction and is referred to herein as the "T.Y. Lin As-built model". This model was used by T.Y. Lin to predict the long-term deflections included in the maintenance manual for the NHVV produced in October,1998.

Section 5.2 describes the operation of the SFRAME program. Sections 5.3 and 5.4 outline the modeling of the NHVV culminating in the "T.Y. Lin As-built model". Finally section 5.5 describes the development of concrete material properties for use in this study, based on the CTL test data of the concrete used in the NHVV.

5.2 SFRAME operation

5.2.1 SFRAME construction operation

5.2.1.1 Material model operation

The time dependent phenomena in concrete are some of the most significant factors influencing the structural behavior of segmentally erected prestressed concrete bridges. Accurate consideration of time dependent concrete behavior is necessary for the accurate prediction of stresses and deflections in the structure at all load levels. Material properties influenced by time include the strength, f'_c, modulus of elasticity, E_C, creep strain and shrinkage strain. Three material models can be used in SFRAME, namely the ACI 209 recommendations (ACI 209,1992), the CEB/FIP recommendations (CEB/FIP, 1993), or

laboratory test data. These models provide the constitutive properties used in the time dependent analysis of the structure. The ACI and CEB/FIP are two built-in models in SFRAME. The time dependent material properties of these two models can be determined by the SFRAME program. When the lab model is specified, the loading ages, observation times, elastic modulus, creep strain and shrinkage strain are not generated by the program and must be directly input by the user.

5.2.1.2 Frame element operation

The plane frame element in SFRAME is based on classical Bernoulli-Euler beam kinematics. The frame element has six global displacement degrees of freedom, consisting of two translations and one rotation at each node. The element consists of parallel concrete and mild steel components to model the typical reinforced concrete bridge girder. The mild steel component is assumed to be uniformly distributed over the entire cross section. Each element has a constant cross section over its length. Dead load is automatically applied as equivalent concentrated forces at the nodes. Each element may be installed into and subsequently removed from the structure at any solution step. Frame elements are installed by including the contributions of their current stiffness matrix, dead load and time dependent strains.

5.2.1.3 Prestressing tendon operation

The prestressing tendon idealization in SFRAME is based on representing the actual curved geometry of a post-tensioned tendon by a system of piecewise linear prestressing

segments. The displacements of tendon points are rigidly constrained to the displacements of their associated nodes. The initial prestressing forces in the tendon segments at the time of the tendon's installation are computed by SFRAME based on input jacking forces at the tendon ends and short term losses over the length of the tendon due to friction and anchorage slip. SFRAME idealizes the tendon force profile as linear over the tendon length and closely approximates the actual tendon force profile.

5.2.1.4 Traveling formwork operation

The traveler element in SFRAME is provided in order to restrain the displacements of freshly cast frame elements. These elements have zero or near-zero elastic modulus and would otherwise undergo large incremental displacements, but are restrained by the actual traveling formwork, Traveling formwork for construction of the concrete segments is included by modeling each actual traveler as two short beam elements. For the construction of each segment, the travel is moved so that it supports the new concrete segment as shown in Figure 5.1.

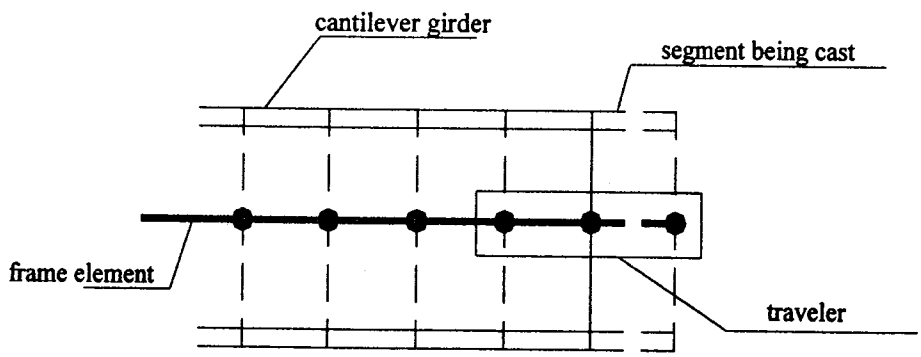

Figure 5.1: Traveler model

5.2.2 SFRAME Program Structure

The SFRAME computer program consists of a short main program and approximately 100 Fortran subroutines, which perform the input and output functions, database management functions, and the numerical computations required for the time dependent solution. These subroutines are grouped into several source modules listed as follows:

a) The Root Module

Initializes the database and the problem solution, controls overall program flow, and calls the other modules when required by the input commands.

b) The Concrete Parameters Module

Inputs and generates the tables of time dependent concrete material model parameters for creep, shrinkage, and aging of the concrete.

c) The Mesh Input Module

Inputs and generates the node coordinates, material properties, and element types and locations. Computes and files all frame and tendon element characteristic matrices.

d) The Change Module

Interprets all structure configuration change commands. Initializes nodal displacements, tendon segment forces and traveler element characteristic matrices based on input commands.

e) The Solve Module

Solves the current structure for one time step. This module performs the bulk of the numerical operations.

f) The Output Module

Prints and summarizes the total nodal displacements and reactions, and frame, tendon and traveler element internal stresses and stress resultants at any time step.

5.2.3 Numerical solution strategy

The solution is based on combining a finite element analysis of the structure with a step forward integration scheme in the time domain. The time domain is subdivided into a number of time steps, and an analysis of the finite element system is performed for each step. Time dependent strains over the time step are considered as an initial strain loading on the finite element system. At the beginning of each time step, the complete stress, strain and displacement distribution within the structure is known. Over the length of the time step, any external load increment is gradually applied, and all resulting displacements, stresses and strains in the structure are assumed to vary linearly from their initial values to their final values, which are computed by the program. The linear variations of loading increment and structural response require the use of a zero length time step when instantaneously applied loadings or changes in the structure configuration are considered. At the end of the time step a new stress, strain and displacement distribution within the structure is known.

5.3 Analytical modeling

5.3.1 Structure introduction

The North Halawa Valley Viaduct is a segmental post-tensioned concrete box-girder bridge. The structure consists of two parallel viaducts, one inbound and one outbound.

The instrumentation was placed on Unit 2 of the Inbound Viaduct (Unit 2 IB), which was modeled with SFRAME to analyze the long-term structural response.

Unit 2IB of the Inbound Viaduct is 1782 feet in length. It consists of seven piers and six spans. The span lengths vary from 200 feet to 360 feet. The third and the fourth piers are fixed and the other pier supports are on sliding bearings.

Unit 2 IB was constructed with 82 cast-in-place concrete segments, connected by mild steel reinforcement and post-tensioning. The length of segments is 24 feet in general and up to 28 feet at the midspan closures. The out-to-out width of the box girder top slab is 41 feet and the cell box is 23 feet wide throughout the whole length of the viaduct. The depth of each segment varies from 8 feet at midspan to18 feet near the piers. Typical midspan and endspan cross sections are shown in Figure 5.2.

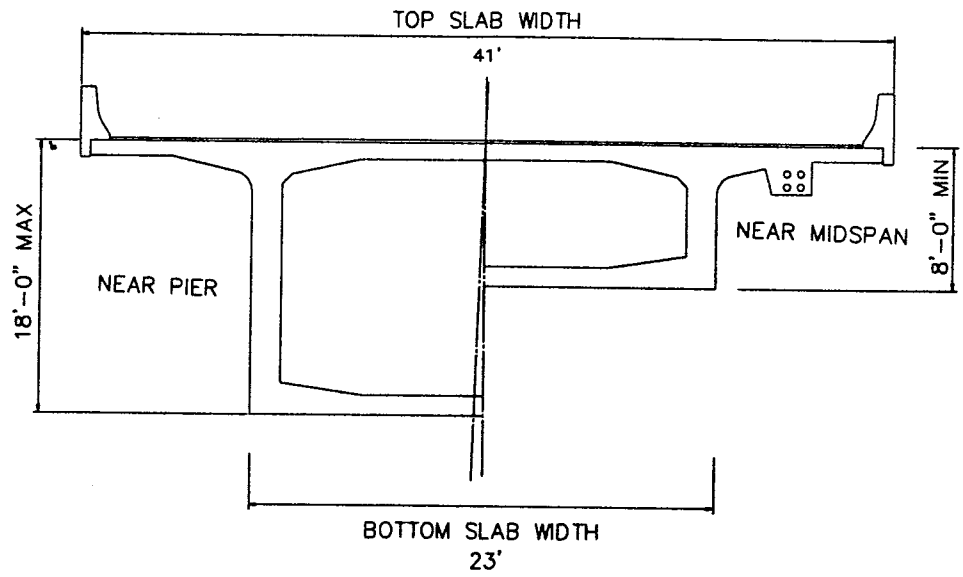

Figure 5.2: Typical box girder cross sections

Concrete barriers were rigidly affixed on both sides of the bridge deck. They are approximately trapezoidal in shape. The top and bottom edges are 9 inches and 1 foot 6 inches respectively. Each barrier unit is 40 feet long, with an expansion gap between units.

5.3.2 Model description

5.3.2.1 Analysis description

The structural model for the longitudinal analysis, shown in Figure 5.3, is a plane frame to represent the total structural system, consisting of nodes in the global X-Y plane connected by frame elements and prestressing tendon elements.

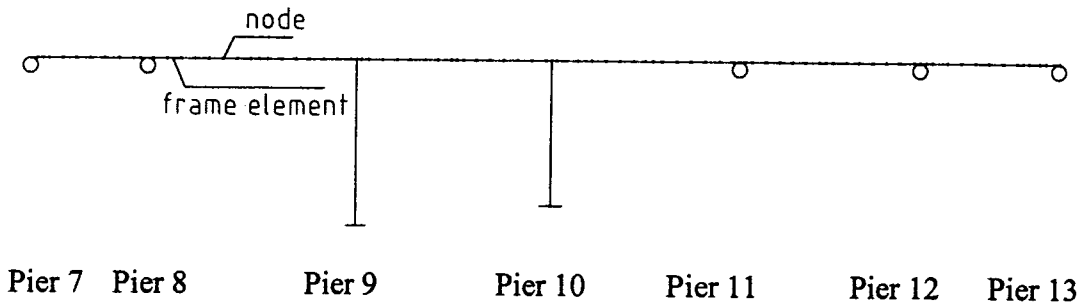

Figure 5.3: SFRAME analytical model

The 92 nodes in the superstructure are located at segment joints along the centroidal axis of the box girder. 218 frame elements are used to model the girder and piers. The elements are each prismatic with constant section properties based on the cross section selected at the mid-length of the element. Each cantilever segment is modeled with one

frame element. Additional elements are used to model the six closure segments at midspan. The pier elements model the gross cross section of the pier.

The cross section in SFRAME consists of a single cell box with wide cantilevered slabs. The girder depth varies from a maximum of 18 feet at the piers to a minimum of 8 feet at midspan. The bottom slab thickness varies from 8 inches at midspan to a maximum of 24 inches at the piers. For the section properties and dead load generation, the cross section of each girder element is idealized as shown in Figure 5.4. A 2 inch thick overlay was added to the top of the roadway 2 years after the end of construction of the box girder. The dead weight of the overlay is included in the analysis, but its contribution to the section properties is ignored. Any contribution of the barriers to the section properties also is ignored in this model.

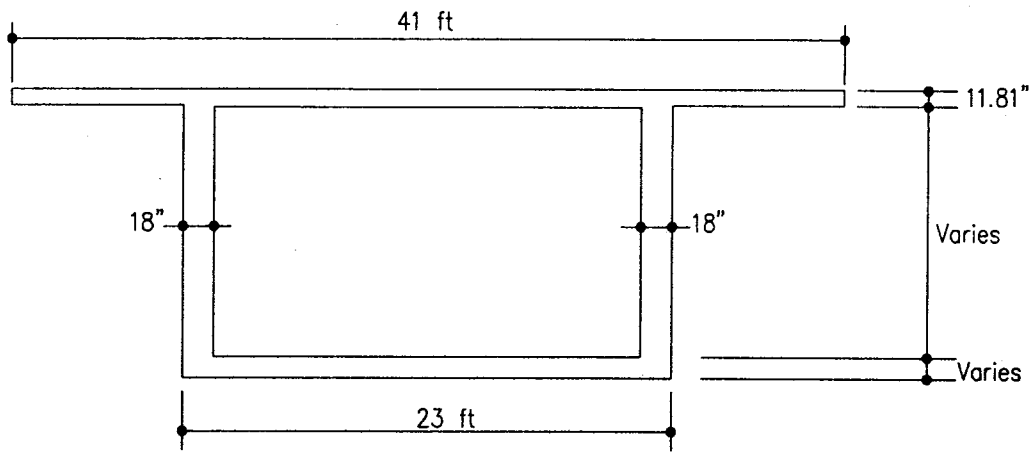

Figure 5.4: Idealized cross section in SFRAME

Uniformly distributed mild steel reinforcement is included in all elements, based on an area ratio of 0.5 percent in the girder and 1.5 percent in the piers.

The post-tensioned segmental structure contains three major types of pretressing tendons. Up to sixty-four cantilever tendons are used at each pier for construction of the segmentally balanced cantilevers. Up to sixteen span tendons are located in the bottom slab at midspan of each span to provide positive moment capacity. Eight continuity tendons provide continuous prestressing along the length of the Viaduct. During construction, each concrete segment was post-tensioned to the previous segments with two cantilever tendons. After the closure at midspan, the span tendons were installed and post-tensioned to provide positive moment capacity. Finally the continuity tendons were stressed from both ends to provide additional negative moment capacity at the supports and positive moment capacity at midspan. The continuity tendons also contribute to the shear capacity of the box girder stems.

All SFRAME analyses were performed in units of pounds and inches.

5.3.2.2 Material model in SFRAME

In the original design of the viaduct, T.Y. Lin used the CEB/FIP material model for SFRAME long-term analysis. In this study, CTL laboratory test results were used in the SFRAME lab material model in order to model the concrete properties more realistically. The detailed calculation of these material parameters is discussed in Section 5.5.

The uniformly distributed mild steel reinforcement in the frame element has elastic modulus of E_s = 29,000,000 psi. The prestressing steel has elastic modulus

E_p =28,000,000 psi. A relaxation coefficient of R=45 is used for the low-relaxation prestressing steel.

5.3.2.3 Loading and construction sequence for the time dependent analysis

The bridge is analyzed for the as-built construction sequence, in which each segment is cast-in-place and post-tensioned on an approximately 4-day cycle. The daily operations in a typical cycle were as follows:

1) Day 1: install the reinforcing and post-tensioning ducts in the bottom slab of the box girder.
2) Day 2: install the reinforcing and post-tensioning in the webs and the top slab, adjust and set the forms, and perform a button-up survey.
3) Day 3: perform a pre-pour survey and cast the segment.
4) Day 4: stress the cantilever post-tensioning tendons in the top slab, break down and move the forms forward, and perform an as-built survey.

The start of Unit 2 IB construction was on February 22nd, 1994. In SFRAME this date is referred to as day 1. Construction of the unit continued through October 3rd, 1994 when the final tendons were pretressed. This was day 224 in SFRAME. The behavior of the bridge under dead load, superimposed load and prestressing, is traced throughout the construction phase and for 40 years thereafter. The SFRAME results are output at particular dates in order to compare the model prediction with the site measurements at the same dates.

5.4 T.Y. Lin As-built model

Two of the leading analytical models to predict concrete creep and shrinkage are the ACI 209 method (American Concrete Institute-U.S.A.) and the CEB-FIP method (Comite Euro-International du Beton/Federation International de la Precontrainte-Europe). For the original design of the North Halawa Valley Viaduct, T.Y. Lin selected the CEB/FIP-78 model for prediction of creep and shrinkage. Since prior research had indicated that Hawaiian concrete exhibits greater creep and shrinkage than Mainland US and European concrete (Hamada and Chiu, 1972), T.Y. Lin commissioned laboratory creep and shrinkage tests on the viaduct trial concrete mix. The CEB model was modified based on these short-term laboratory tests.

Vertical deflection predictions based on this as-built model were included in the maintenance manual (T.Y. Lin International, 1998) for the Viaduct and are shown in Figure 5.5. Note that in Figure 5.5 and all subsequent Figures showing deflected shape, the vertical deflections are greatly exaggerated to allow for easier comparison between plots.

5.5 Long-term concrete properties for SFRAME

5.5.1 Long-term modulus of elasticity prediction

The modulus of elasticity of concrete varies with different concrete strengths, concrete age, type of loading, and the characteristics of the cement and aggregate. In this study, three prediction methods are used to calculate the elastic modulus for comparison with

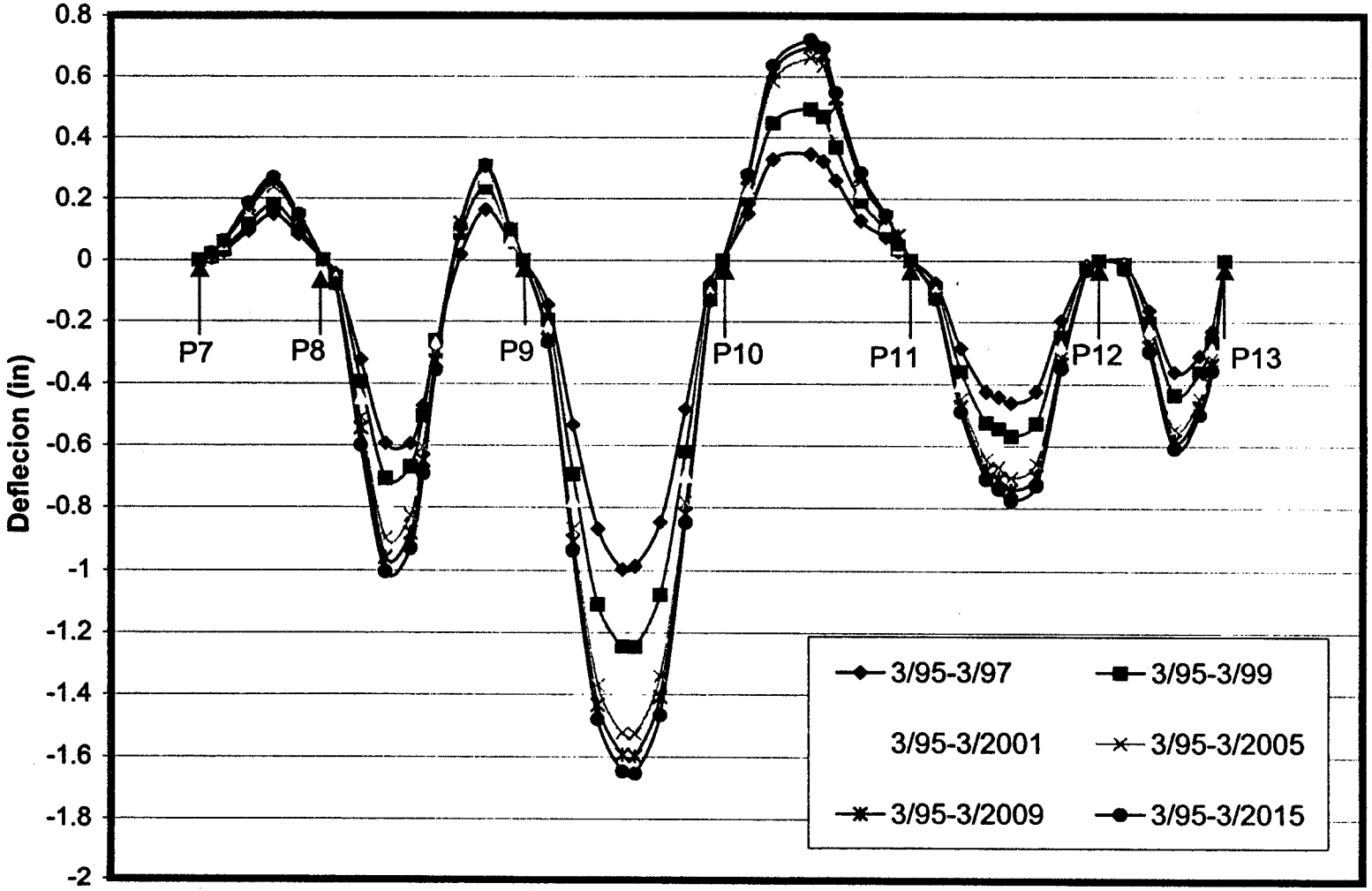

Figure 5.5: T.Y. Lin As-built model deflection prediction

the average CTL 3-day, 28-day and 90-day test results (Table 4.2). A final prediction model was selected for use in the SFRAME input.

5.5.1.1 ACI209R-92 modulus of elasticity prediction

ACI209R-92 (ACI 209, 1992) gives the following expression for calculating the modulus of elasticity of normal-weight concrete:

$$E(t) = 57{,}000\sqrt{f'_c(t)} \qquad (5.1)$$

Where

t is the concrete age in days, and

$f'_c(t)$ is the compressive cylinder strength in psi at time t.

For example, the 28-day modulus is given by:

$$E(28) = 57{,}000\sqrt{f'_c(28)} \qquad (5.2)$$

Rearranging the above equation gives:

$$f'_c(28) = \left(\frac{E(28)}{57{,}000}\right)^2 \qquad (5.3)$$

The equation relating concrete strength development with time is a hyperbolic-power expression given by ACI209R-92 as follows:

$$f'_c(t) = f'_c(28)\frac{t}{\alpha + \beta \cdot t} \qquad (5.4)$$

Where

$f'_c(28)$ = 28-day concrete compressive strength,

t = concrete age in days,

α = 4.0 - for Type I cement,

α = 2.3 - for Type III cement,

β = 0.85 - for Type I cement, and

β = 0.92 - for Type III cement.

By substituting equations (5.4) and (5.3) into equation (5.1), the modulus of elasticity at any time can be determined from:

$$E(t) = E(28)\left(\frac{t}{\alpha + \beta \cdot t}\right)^{0.5} \qquad (5.5)$$

Figure 5.6 shows the ACI 209R-92 modulus of elasticity predictions for concrete using type I and III cements against concrete age based on a logarithmic scale. The average 3-day, 28-day and 90-day CTL test results also are shown for comparison. Although the Type I cement prediction agrees well with the 28-day and 90-day test results, it significantly underestimates the 3-day measured modulus. This is likely the result of the characteristics of the cement used in the NHVV. The only cement produced in Hawaii is ground by Hawaii Cement Co. from imported clinker. This cement is classified as Type I, however it is ground to a fineness similar to Type III cement in order to accelerate early age strength gain. No true Type III cement is produced in Hawaii.

In order to predict the modulus of elasticity more accurately at all concrete ages, the ACI 209R-92 Type III prediction was modified to fit the CTL test results as described in the following sections.

5.5.1.2 Modified ACI 209 modulus of elasticity prediction

In order to obtain better long-term predictions of modulus of elasticity, the ACI 209 formula for Type III was modified as follows:

$$f'_c(t) = f'_c(28)\left(\frac{t^{0.75}}{\alpha + \beta \cdot t^{0.75}}\right)^{0.5} \qquad (5.6)$$

where

$f'_c(28)$ = 28-day concrete compressive strength,

t = Concrete age in days,

α = 1.0 - for Type III cement (changed from 2.3),

β = 0.92 -for Type III cement (unchanged).

Therefore, the modulus of elasticity at any time is obtained as

$$E(t) = E(28)\left(\frac{t^{0.75}}{\alpha + \beta \cdot t^{0.75}}\right)^{0.5} \qquad (5.7)$$

Figure 5.7 shows the modified ACI long-term modulus predictions for concrete using Type III compared with the measured values. The original ACI209R-92 (type III) is also shown for comparison. This modified ACI prediction better approaches the test data trend. Agreement with test data is best at 28-days but slightly underestimated at 3 and 90

days. A final modification was made to bring the prediction into closer agreement with 3-day and 90-day results.

5.5.1.3 The final modulus of elasticity prediction

A scaling factor of 1.065 was applied to equation (5.7), leading to the final modulus of elasticity used in the SFRAME material model as follows:

$$E(t) = 1.065 \times \left[E(28) \left(\frac{t^{0.75}}{\alpha + \beta \cdot t^{0.75}} \right)^{0.75} \right] \qquad (5.8)$$

Figure 5.8 shows this final prediction along with the original and modified ACI209R-92 curves for comparison.

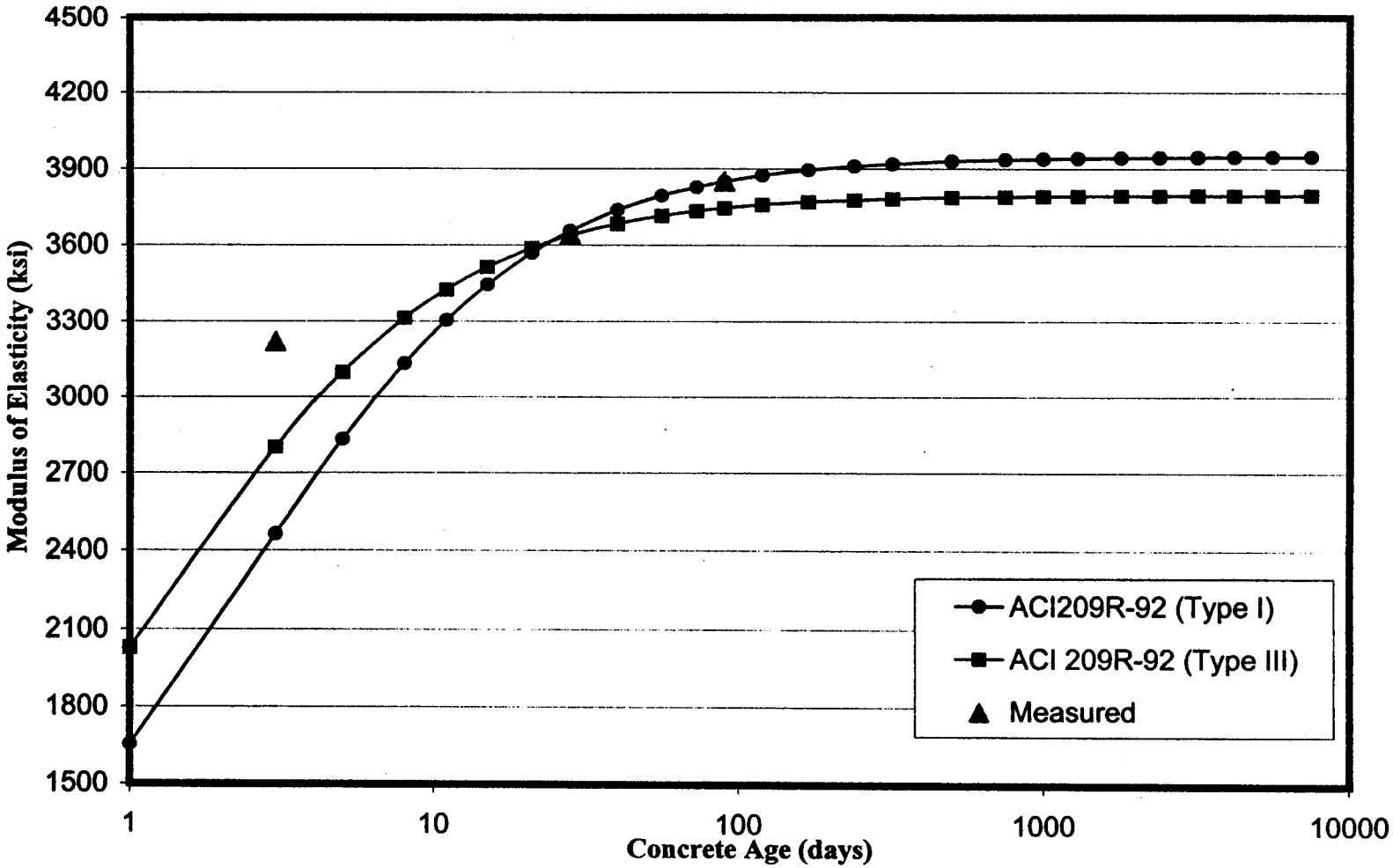

Figure 5.6: ACI 209R-92 modulus of elasticity prediction

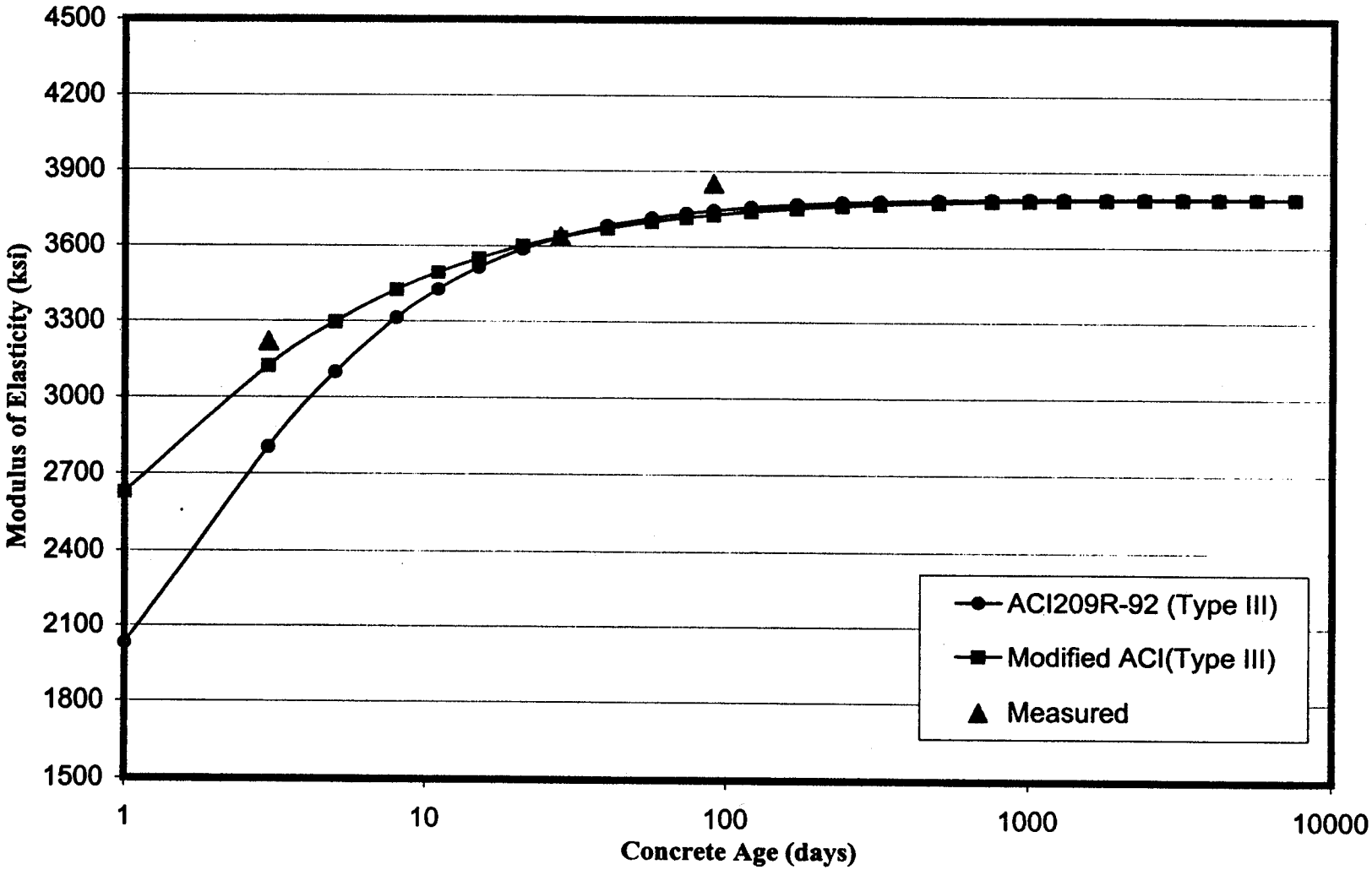

Figure 5.7: ACI (Type III) modulus of elasticity prediction

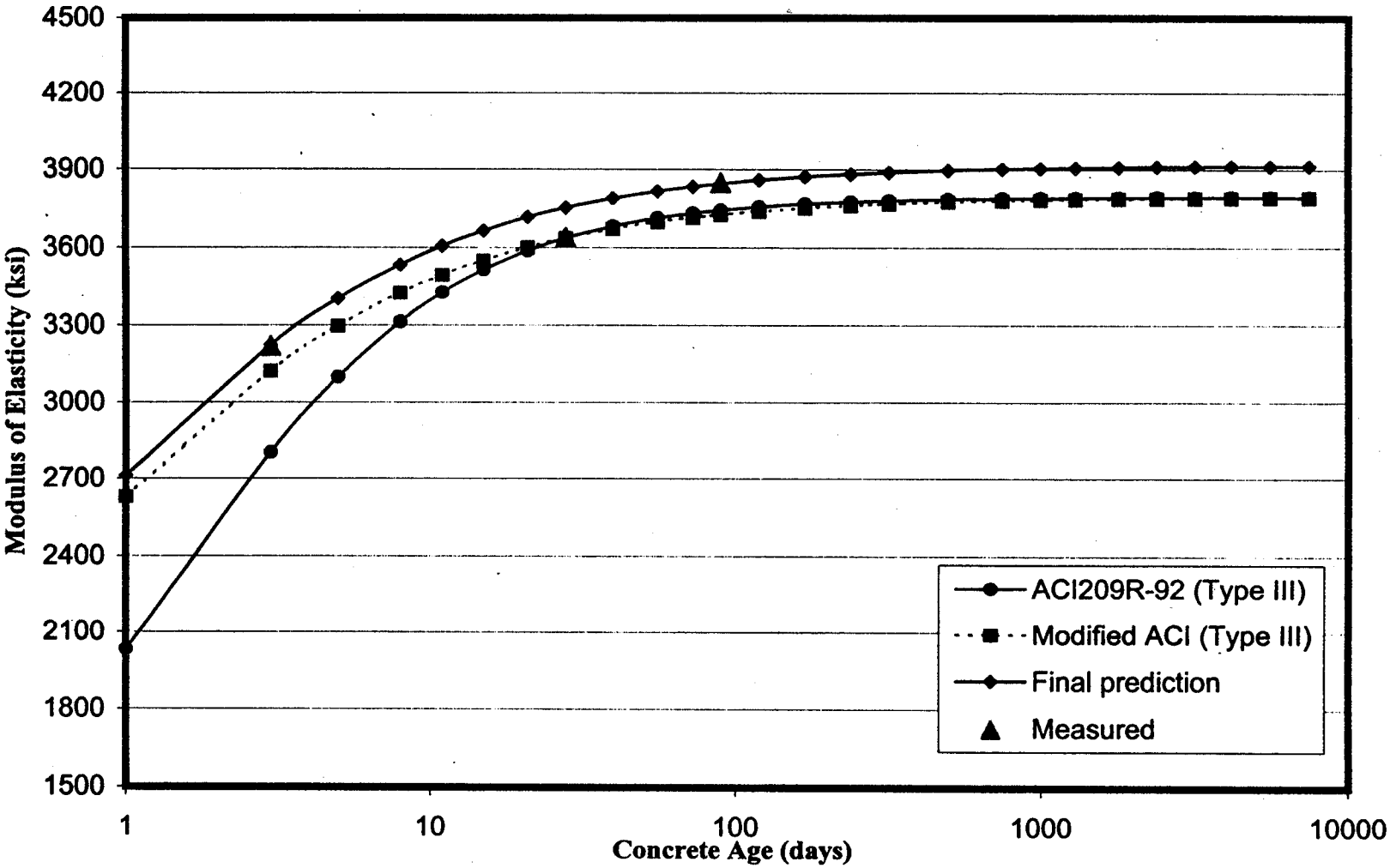

Figure 5.8: Final modulus of elasticity prediction

5.5.2 Long-term creep and shrinkage prediction

Numerous expressions have been proposed for the development of concrete creep and shrinkage with time. However, because creep and shrinkage effects are so complicated and because a satisfactory mathematical theory has yet to be developed, potentially the most accurate means for predicting long-term creep and shrinkage strains is to extrapolate from short-term test results and adjust the long-term parameters accordingly.

5.5.2.1 Prediction methods

A previous study of the creep and shrinkage measured by CTL on concrete samples from Unit 2 IB showed that two mathematical models could be modified based on short-term test results (Durbin and Robertson, 1998). Their study showed that among all the prediction models, the Bazant and Baweja B3 Short Form creep model (Bazant and Baweja, 1996) and the Gardner and Zhou shrinkage model (Gardner and Zhou, 1993) gave the best predictions compared with the measured values for one year of loading and drying. These two models are referred to herein as the Bazant creep model and the Gardner shrinkage model.

5.5.2.2 Regression analysis

As demonstrated by Durbin and Robertson, modified prediction values for creep and shrinkage may be obtained by comparing short-term test data points against the values obtained by using the predictive models. If the predictive model data, $\phi'(t)$, corresponded exactly to the test data, $\phi(t)$, a plot of $\phi'(t)$ versus $\phi(t)$ would be a 45° degree straight

line passing through the origin. In reality, these values do not correspond exactly. To obtain the least deviation between the test data and the model, a least-squares regression is calculated. This results in the regression line:

$$\phi''(t) = p_2\phi(t) + p_1 \qquad (5.9)$$

Where

p_1 = the y-intercept of the regression line,

p_2 = the slope of the regression line,

$\phi(t)$ = creep coefficients (or shrinkage strains) from the short-term test data,

$\phi'(t)$ = creep coefficients (or shrinkage strain) from the predictive model, and

$\phi''(t)$ = modified creep coefficients (or shrinkage strain) using the short-term data.

The regression coefficients p_1 and p_2 are calculated as follows (Bazant and Baweja, 1996):

$$p_2 = \frac{n\sum(\phi_i\phi'_i) - (\sum\phi_i)(\sum\phi'_i)}{n\sum(\phi_i^2) - (\sum\phi_i)^2} \qquad (5.10)$$

$$p_1 = \bar{\phi}' - \bar{\phi} \qquad (5.11)$$

where

n = the number of data points in the short-term test data,

ϕ_i = the ith creep coefficient (or shrinkage strain) from the short-term test data,

ϕ'_i = the ith creep coefficient (or shrinkage strain) from the predictive model,

$\bar{\phi}$ = the average value of the short-term test creep coefficients (or shrinkage strains), and

$\bar{\phi}'$ = the average value of the predictive model creep coefficients(or shrinkage strains).

Durbin and Robertson used this procedure to modify the Bazant creep and Gardner shrinkage predictions to provide a better estimate of long-term concrete behavior.

5.5.2.3 Long-term creep strain

Figures 5.9, 5.10, and 5.11 compare the CTL average creep with both original and modified Bazant creep predictive models for concrete loaded at 3 days, 28 days, and 90 days, respectively. Each figure represents the creep test data for a loading period of one year. Using only the first 28 days of test data, the modified Bazant creep model is able to predict the subsequent creep with considerably greater accuracy than the original Bazant model. Using the modified Bazant models, the creep strains for any concrete loading period can be determined. Figures 5.12, 5.13 and 5.14 show the predicted creep for 10,000 days for loading at 3, 28 and 90-days respectively. The CTL relative humidity (RH) is 50% and the volume-to-surface area ratio (V/S) is 1.5in, while the field conditions are an average annual RH of 85% and V/S average of 7.5inch (See Chapter 6). Making these changes in the modified Bazant model produces the final prediction curves shown in Figures 5.12, 5.13, and 5.14.

The Lab Data option in SFRAME requires input of a matrix of creep and shrinkage values. For creep, values of creep coefficient are required for loading ages from 1 to

7,500 days, with concrete age up to 10,000 days. Shrinkage strains are required for each age from drying at 3 days to 7,500 days.

To develop this input matrix, creep values at various loading ages had to be obtained by interpolation and extrapolation from the known test data. For concrete loading from 3 to 90 days, interpolation between the 3, 28 and 90-day predictions was based on a logarithmic time scale. In order to extrapolate beyond 90-day loading, it was necessary to estimate the 7,500-day loading creep curve. This curve was based on Bazant's prediction with an assumed ultimate creep strain of 0.0002 at 10,000 days. For concrete loading from 90 to 7,500 days, logarithmic interpolation was used. To estimate the creep for loading at 1 day, Bazant's prediction was modified using the regression coefficients p_1 and p_2 obtained for loading at 3 days. Figure 5.15 shows the resulting creep predictions for up to 10,000 days for different concrete loading ages.

5.5.2.4 Long-term shrinkage strain

Figure 5.16 compares the CTL average 3-day shrinkage values with both the original and modified Gardner shrinkage prediction models. This figure represents the shrinkage test data for a drying period of one year. Using only the first 28 days of test data, the modified Gardner shrinkage model is able to predict the subsequent shrinkage with greater accuracy than the original Gardner model. Figure 5.17 shows the predicted shrinkage for 10,000 days for drying at 3 days. The CTL relative humidity (RH) is 50% and the volume-to-surface area ratio (V/S) is 1.5in, while the field conditions are an average

annual RH of 85% and V/S average of 7.5in. Making these changes in the modified Gardner shrinkage model produces the final prediction curve shown in Figure 5.17.

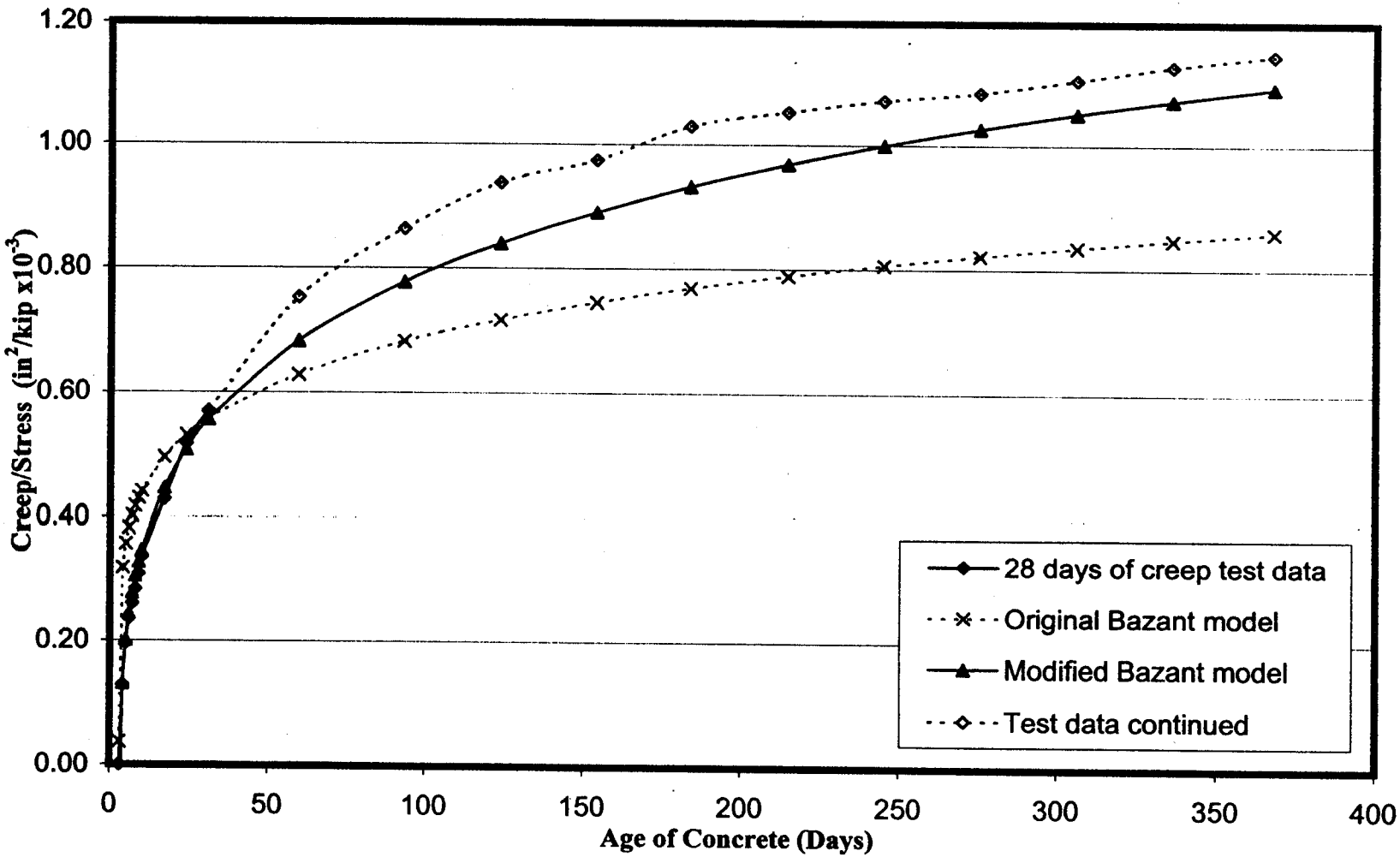

Figure 5.9: Creep prediction for specimens loaded at 3-day concrete age

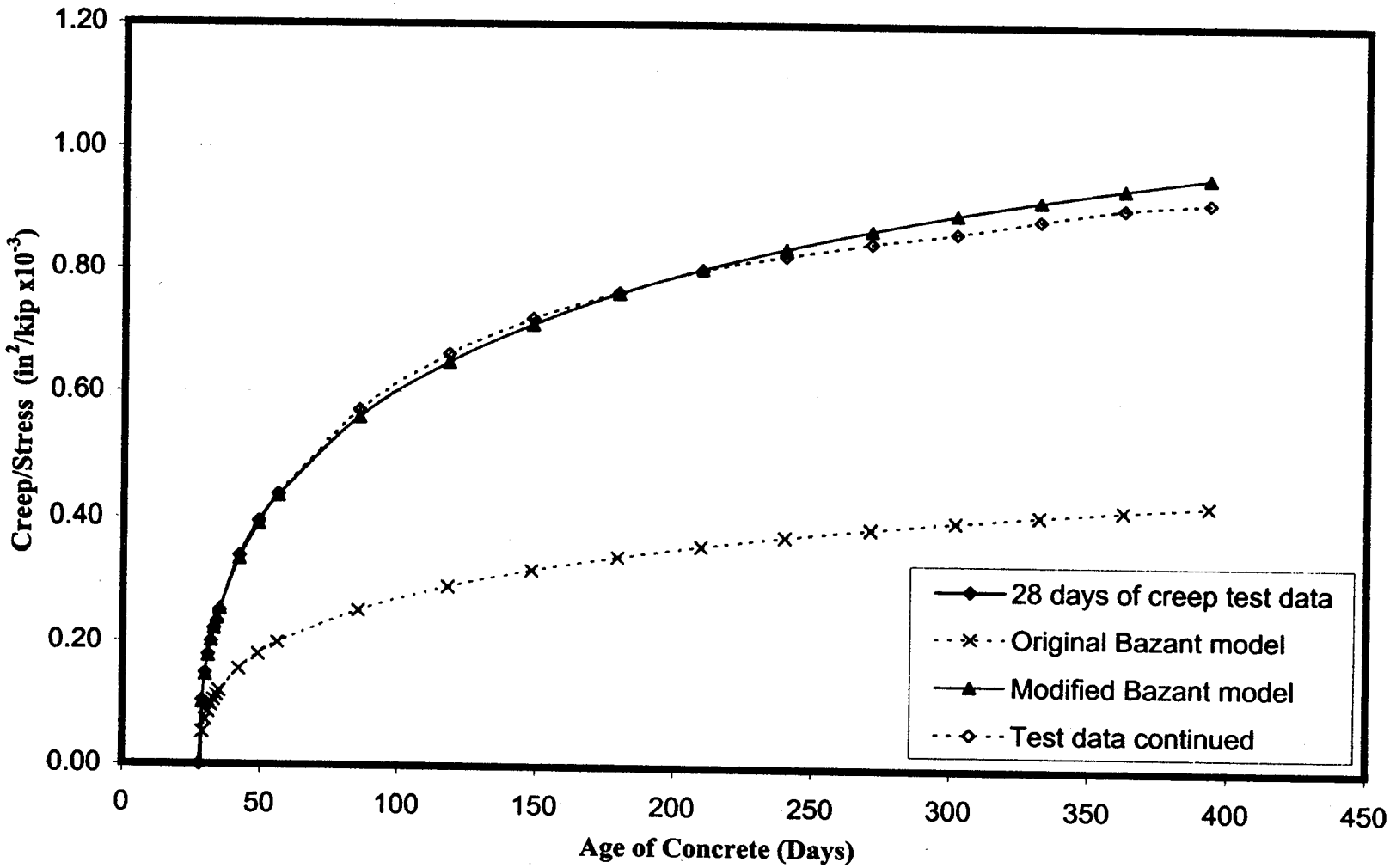

Figure 5.10: Creep prediction for specimens loaded at 28-day concrete age

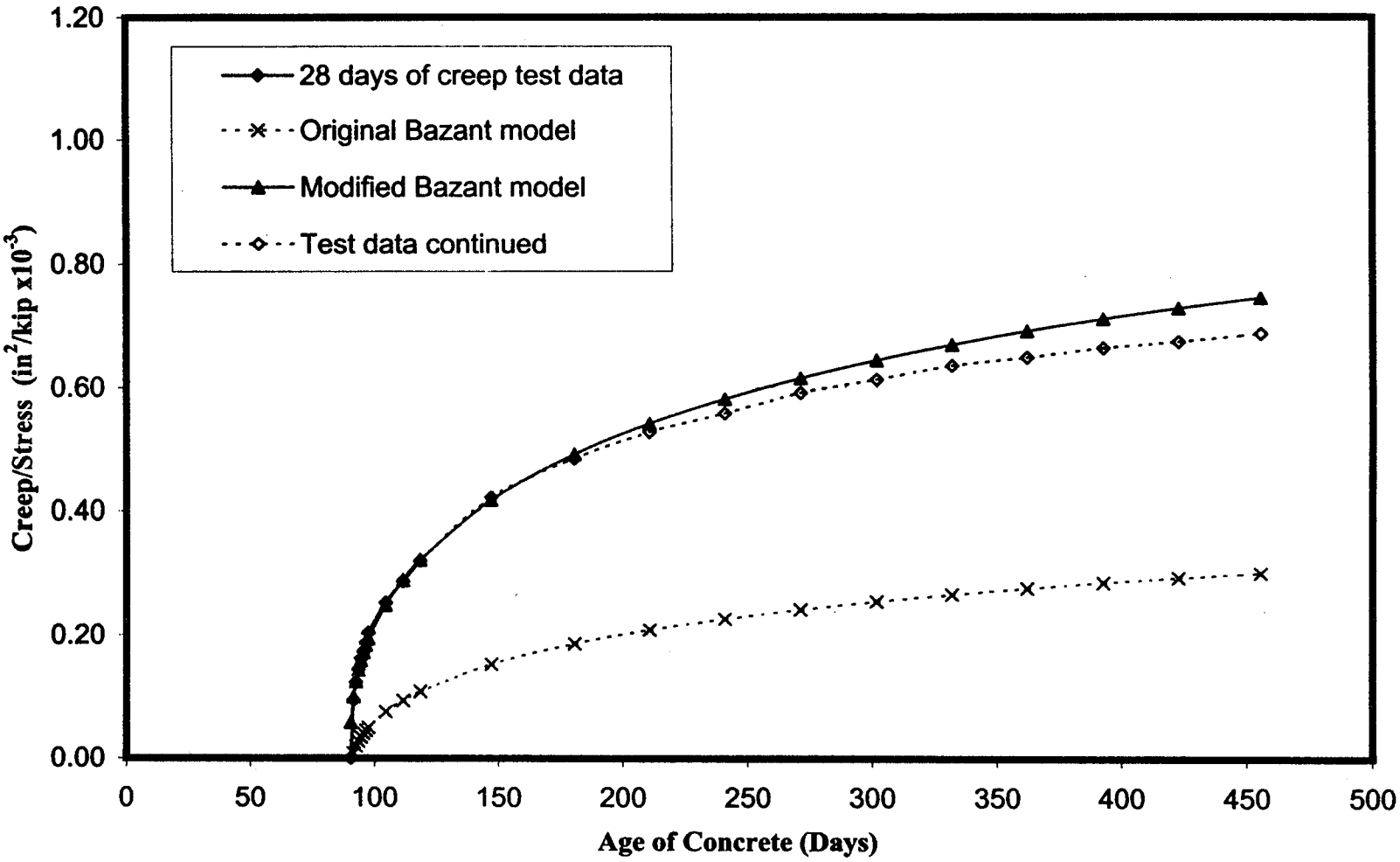

Figure 5.11: Creep prediction for specimens loaded at 90-day concrete age

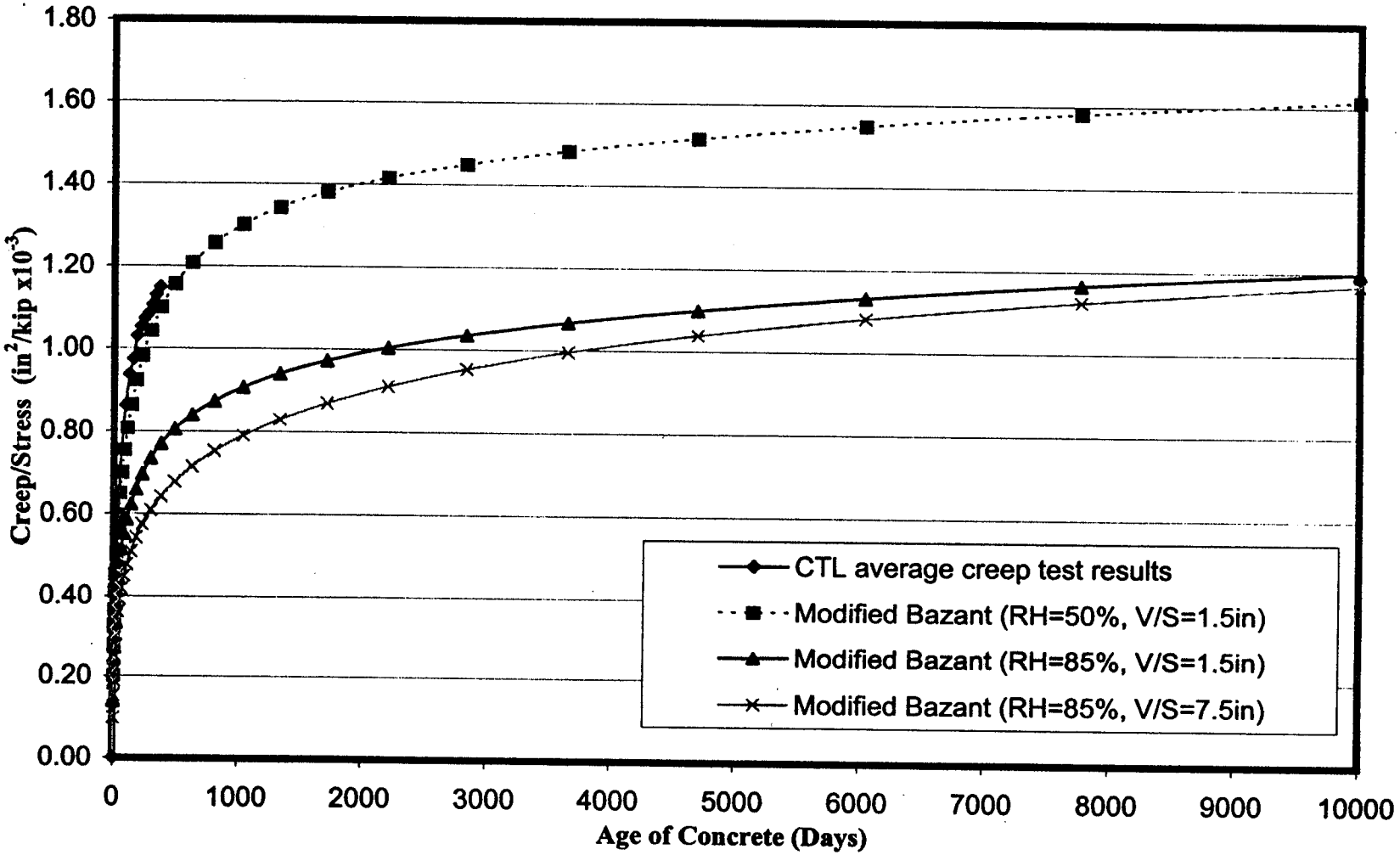

Figure 5.12: Long term creep prediction for concrete loaded at 3 days

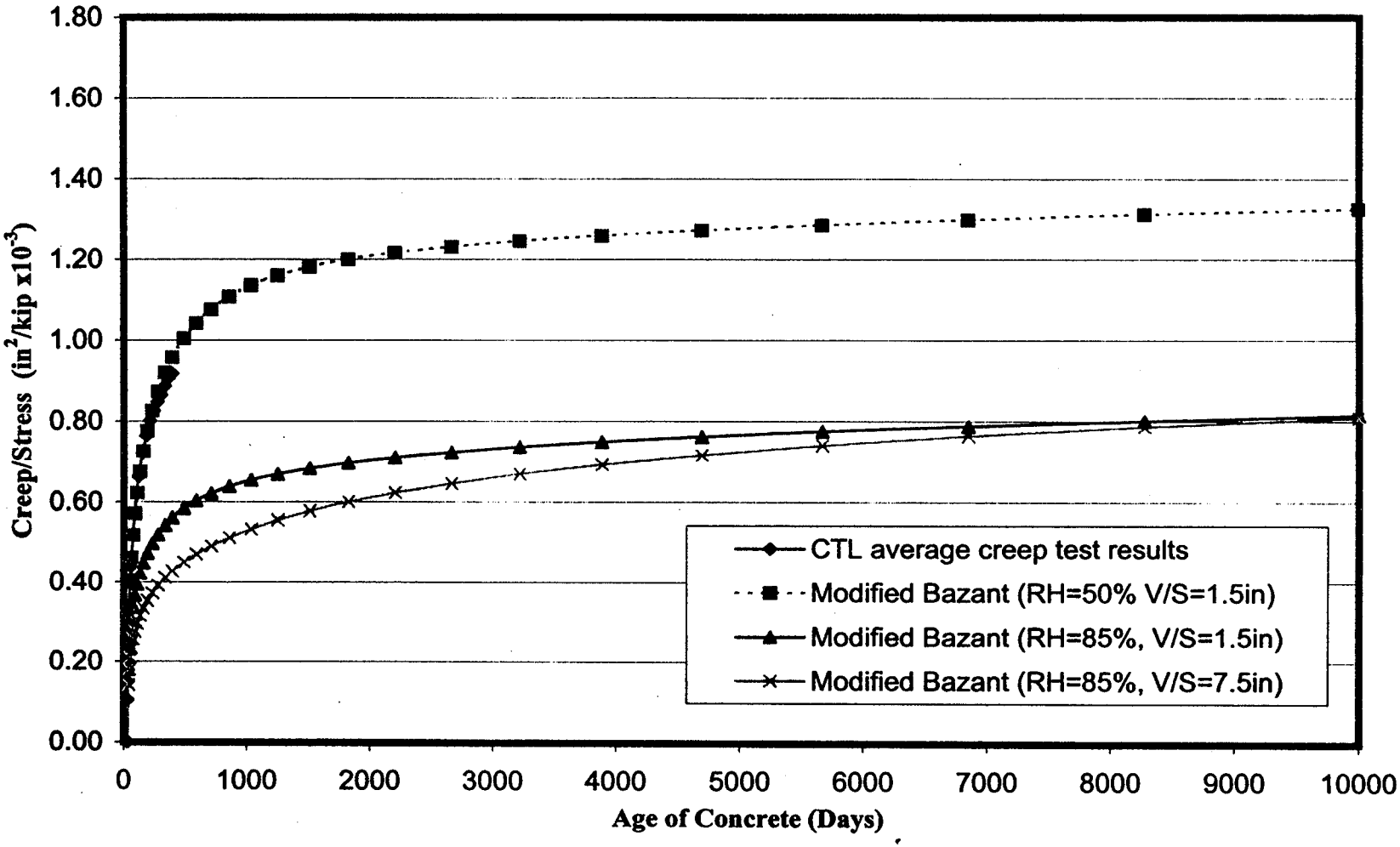

Figure 5.13: Long term creep prediction for concrete loaded at 28 days

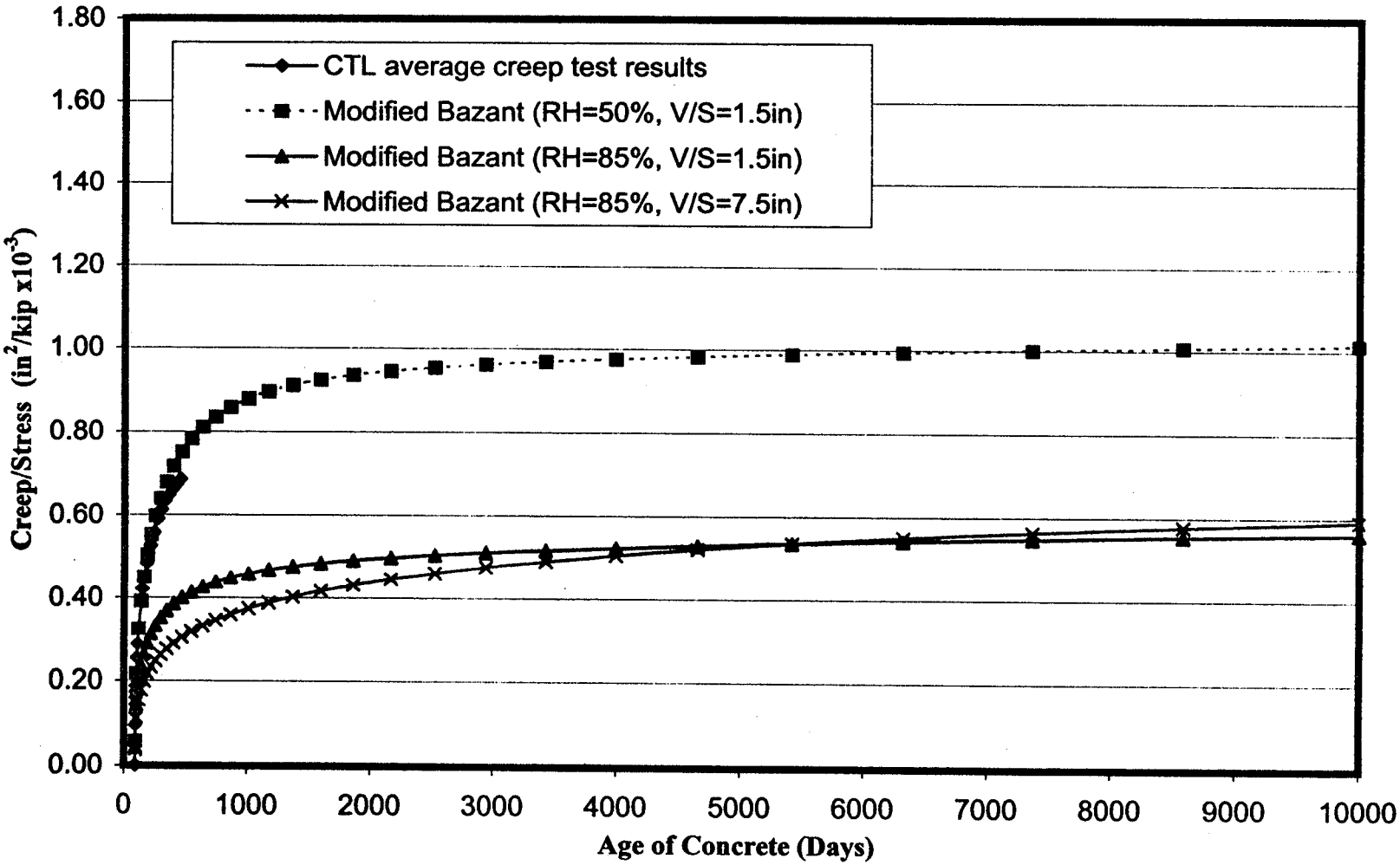

Figure 5.14: Long term creep prediction for concrete loaded at 90 days

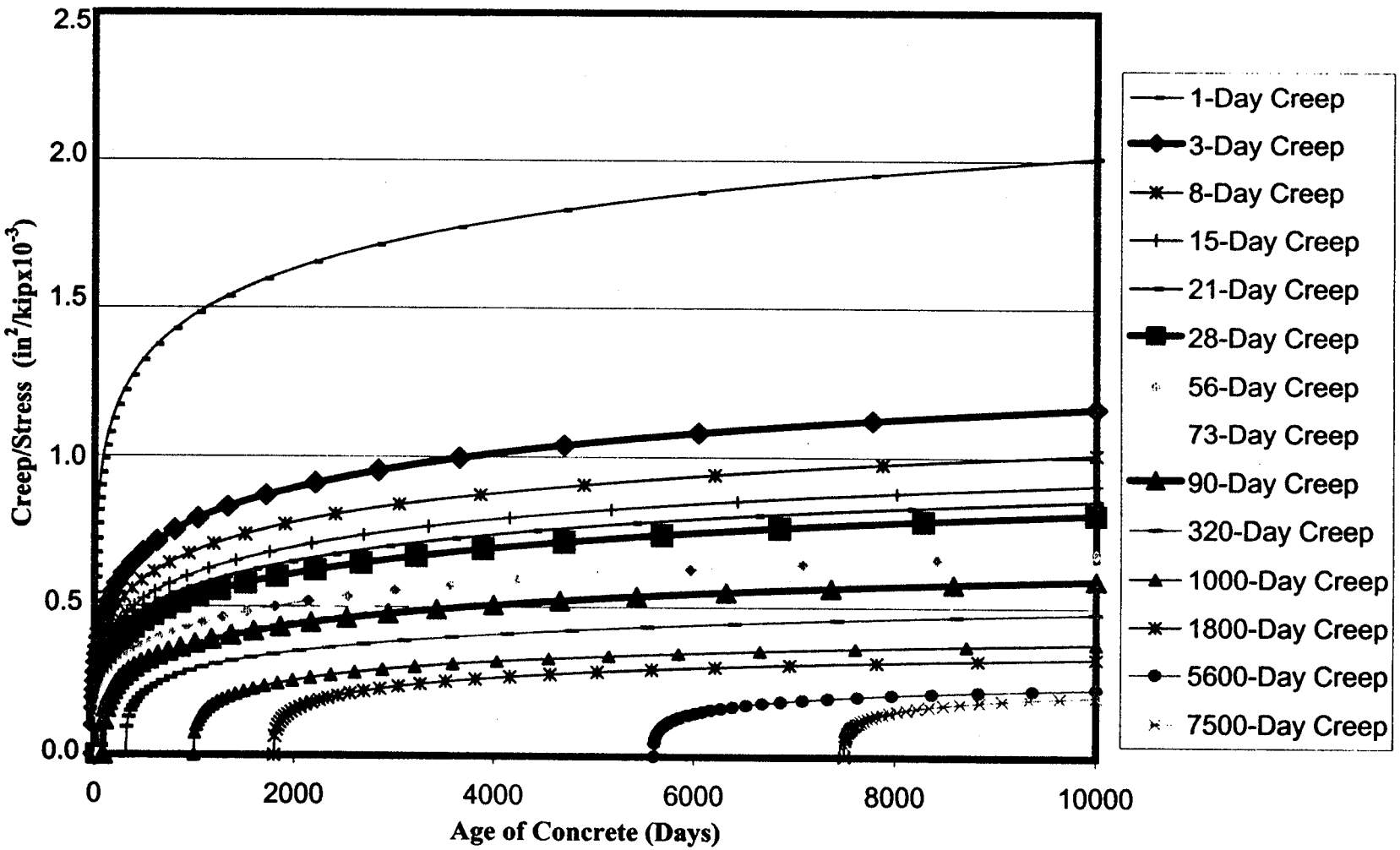

Figure 5.15: Modified Bazant interpolated creep

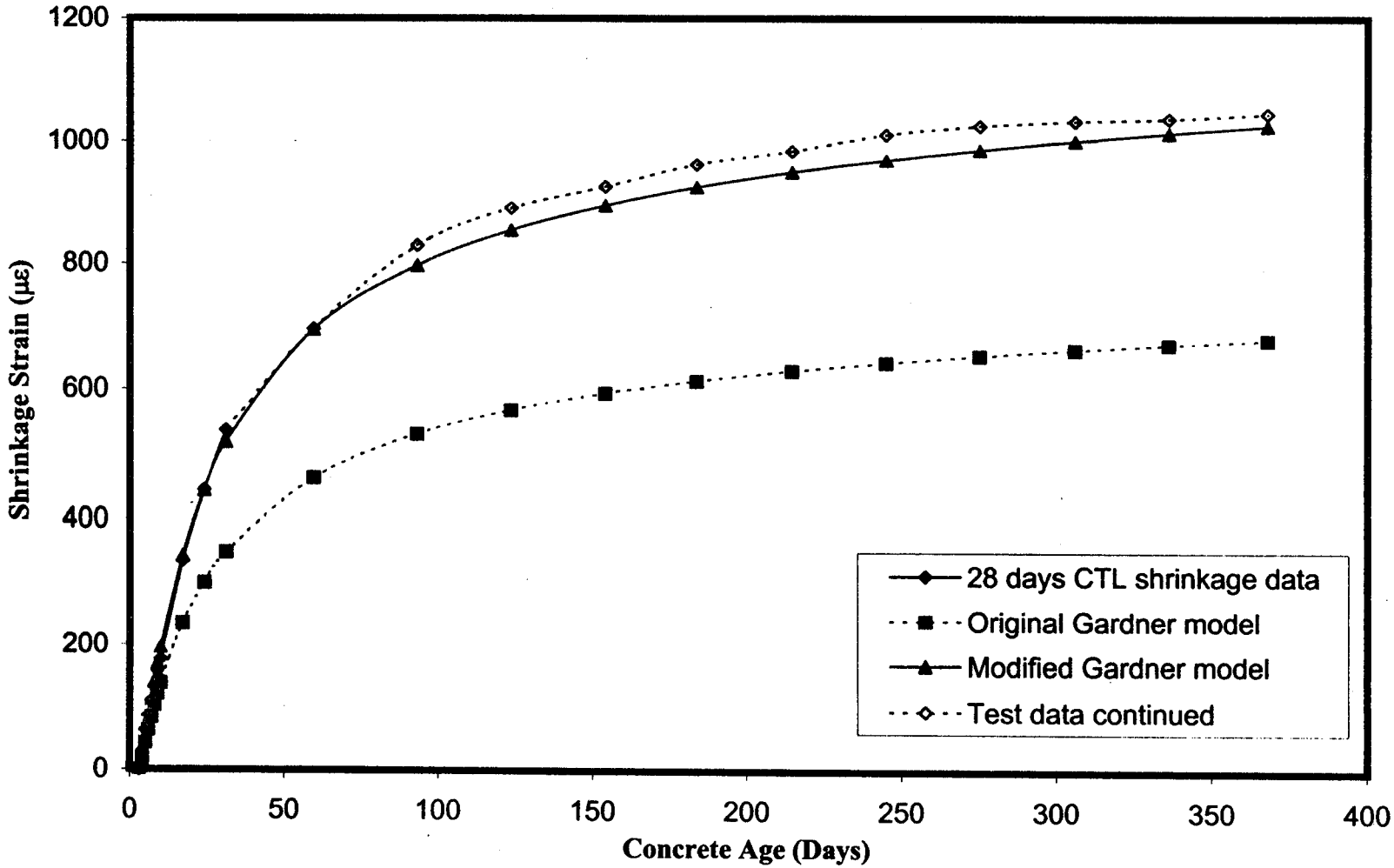

Figure 5.16: Shrinkage prediction

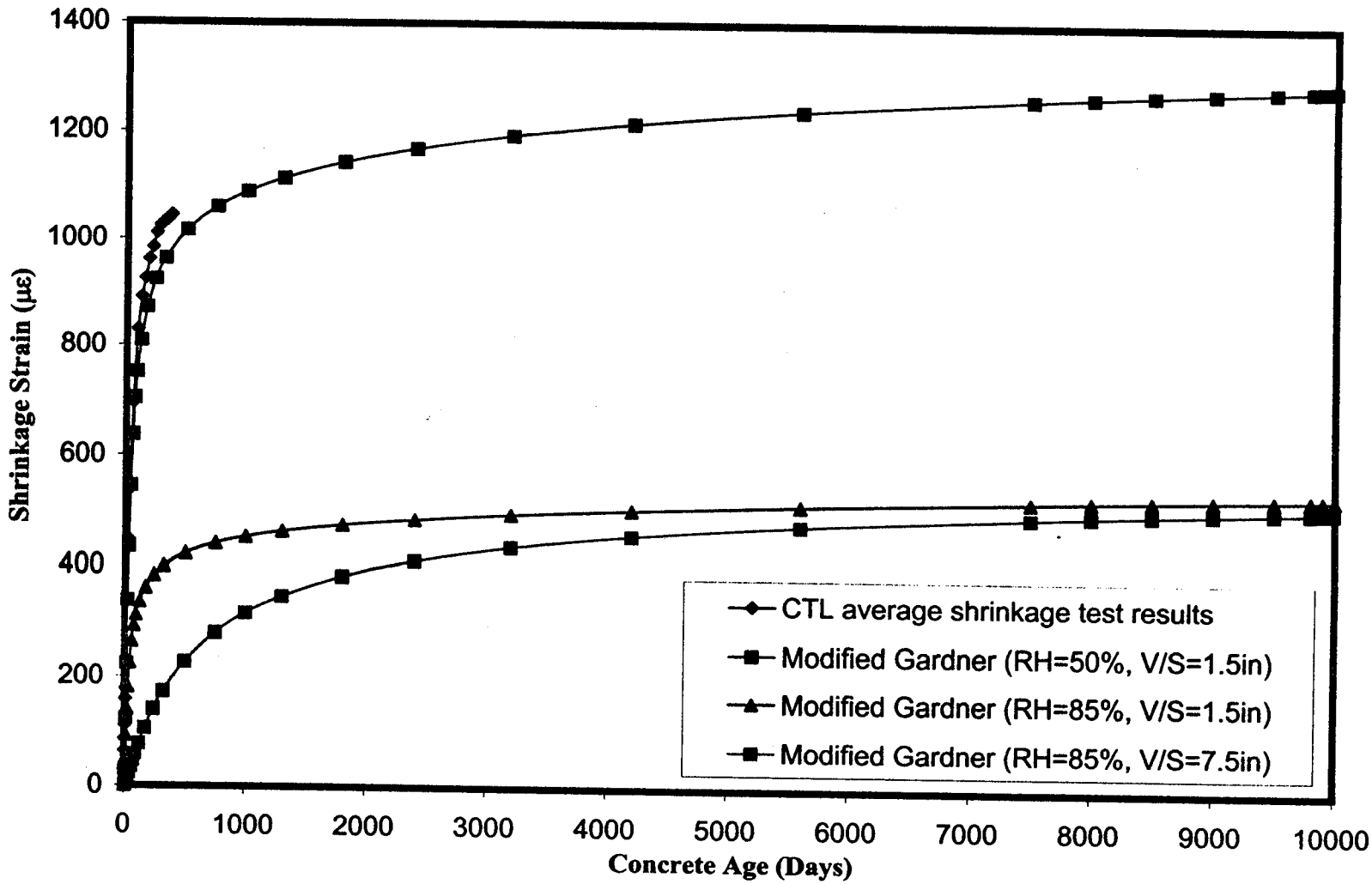

Figure 5.17: Long term shrinkage prediction

CHAPTER 6

SFRAME RESULTS COMPARED WITH SITE MEASUREMENTS

6.1 Introduction

Predicting the complete time dependent response of this type of bridge structure is very complex. The response depends on time dependent material properties and the construction sequence. Accurate prediction of time dependent deflections of a concrete bridge structure due to creep and shrinkage is complicated by the wide range of physical properties of concrete. The creep and shrinkage characteristics of concrete are highly variable and are never exactly known.

In this chapter, analytical predictions were produced using the finite element analysis software SFRAME. Various combinations of material properties were considered. The results of these analyses were compared with the field measurements.

6.2 Long-term deflection

6.2.1 Introduction

The purpose of the base-line system is to monitor the span deflection as discussed in section 3.2.1. Twenty-five measurement stations were used to provide a representation of the viaduct behavior in Spans P8-9, P9-10, P11-12 and P12-13. The measurement stations are roughly 48 feet apart (Figure 3.2).

The initial base-line readings were taken on March 29th, 1995 along with an optical survey of the roadway. Subsequent readings were recorded at various dates up to November 8th, 1998. A followup optical survey was made on June 19th, 1997. The difference between the initial and subsequent readings represents the span deflection during each time period. For corresponding analytical deflections, the dates of the field readings were converted to an equivalent number of days after start of construction in the time domain of SFRAME.

For any given time period, the SFRAME output file gives the position of each node. To isolate pure span deflection, the y-position of the nodes in a span must first be normalized relative to a straight line joining the two ends of the span. Normalization along this straight line eliminates the effect of pier shortening and settlement. In this way, the pure span deflection can be isolated and compared with the base-line field measurements. The difference between the normalized y-position at the initial and subsequent dates represents the predicted deflection during each time period. Comparisons between the normalized base-line reading and predicted deflection are presented in this chapter.

6.2.2 T.Y. Lin As-built model

Section 5.4 presents the deflection prediction included in the NHVV maintenance manual. Figure 6.1 illustrates the span deflection comparison for the time period from March 29, 1995 to June 19, 1997 using the T.Y. Lin As-built model. The analytical model substantially underestimates long-term deflection for the longest span P8-9. This

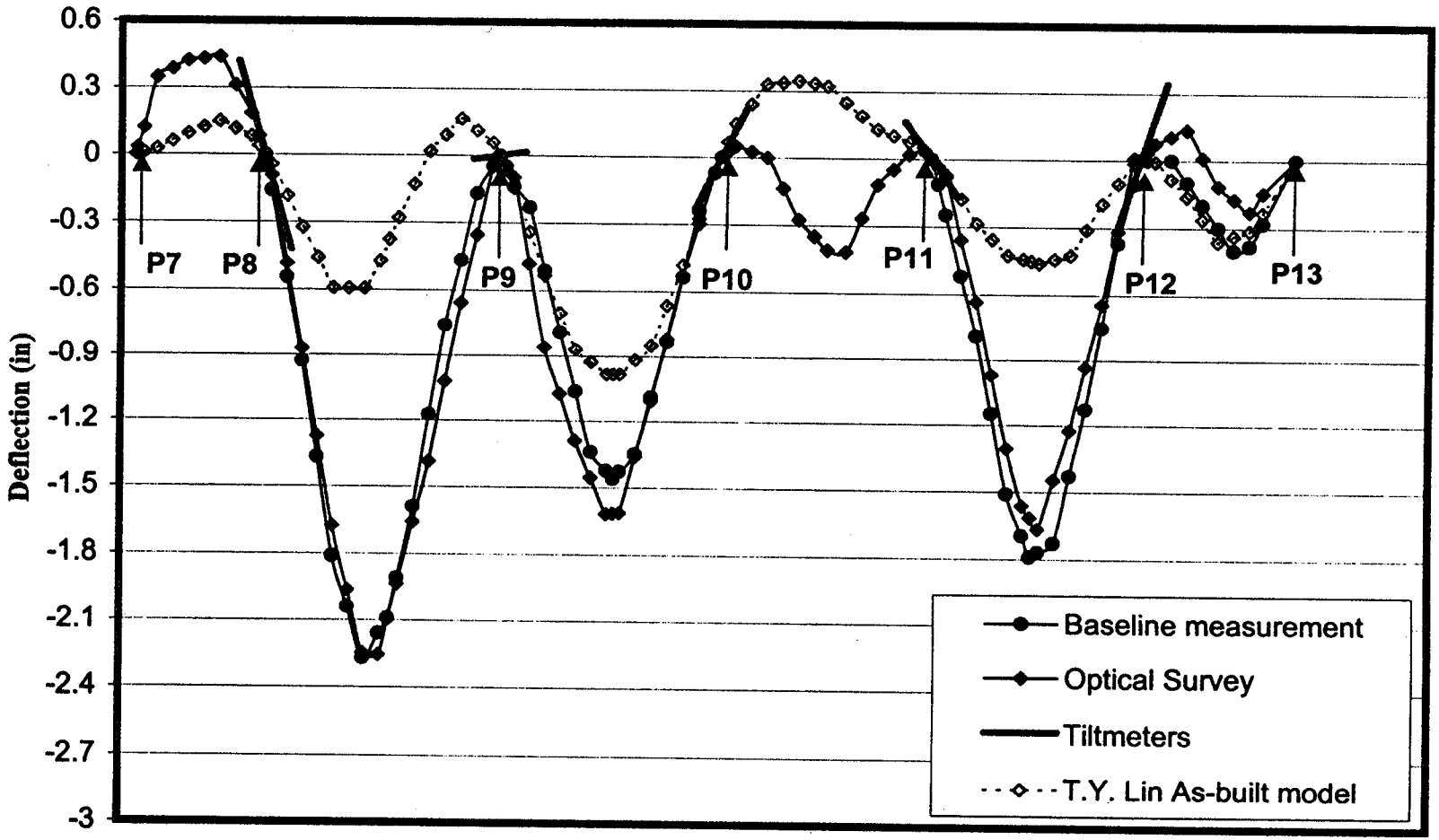

Figure 6.1: Long term deflection of T.Y. Lin As-built model (3/95-6/97)

disagreement between the analytical and observed deflections is attributed to the assumptions made regarding the anticipated concrete material properties. The CEB model used in the T.Y. Lin As-built model underestimates both the creep and shrinkage strain. It is expected that the deflections will increase if more accurate information on the concrete creep and shrinkage are available in the SFRAME material model.

6.2.3 Initial lab model

A more appropriate constitutive model for the long-term concrete behavior can be obtained following the procedures outlined in Chapter 5. The resulting lab model is based on the ACI revised modulus of elasticity prediction, the modified Bazant creep model, and the modified Gardner shrinkage model for long term concrete material properties. All other variables were the same as in the T.Y. Lin As-built model. In particular, the prestressing tendon forces were not adjusted in this initial lab model, although the prestressing forces observed in the field load cell readings were generally less than anticipated from the design.

The long-term deflection between March 29, 1995 and June 19, 1997 based on this initial lab model is plotted in Figure 6.2. As expected, the lab model predicts the long term deflection more accurately than the T.Y. Lin As-built model. Correlation is good for spans P9-10 and P12-13, with the analytical predictions in close agreement with the field measurements. However, the analytical predictions for span P8-9 and span P11-12 differ significantly from the measured deflections. In addition, both T.Y. Lin As-built and

initial lab models predict an upward deflection in span P10-11 whereas the optical survey recorded a downward deflection.

This difference between the analytical results and field measurements makes a parametric study necessary in order to investigate the time-dependent deflection. The main priority of this parametric study is that it can determine the parameter effects separately.

6.2.4 Parametric study

Because of the poor predictions obtained from both the T.Y. Lin As-built and the initial lab models, a parametric study was performed. The intent of this study was to evaluate the effects of variations in several material parameters on the behavior of the bridge and to study the expected range of behavior for this bridge based on a possible range for each parameter.

In this chapter, the parametric study is focused on improving the long-term prediction for the March 1995 to June 1997 deflection. The parameters considered here include field environmental conditions, concrete material properties such as creep, shrinkage and self-weight of the concrete, prestress tendon forces, prestressing steel properties and their combinations. In Chapter 7, possible ranges for each variable are considered and deflection envelopes are developed.

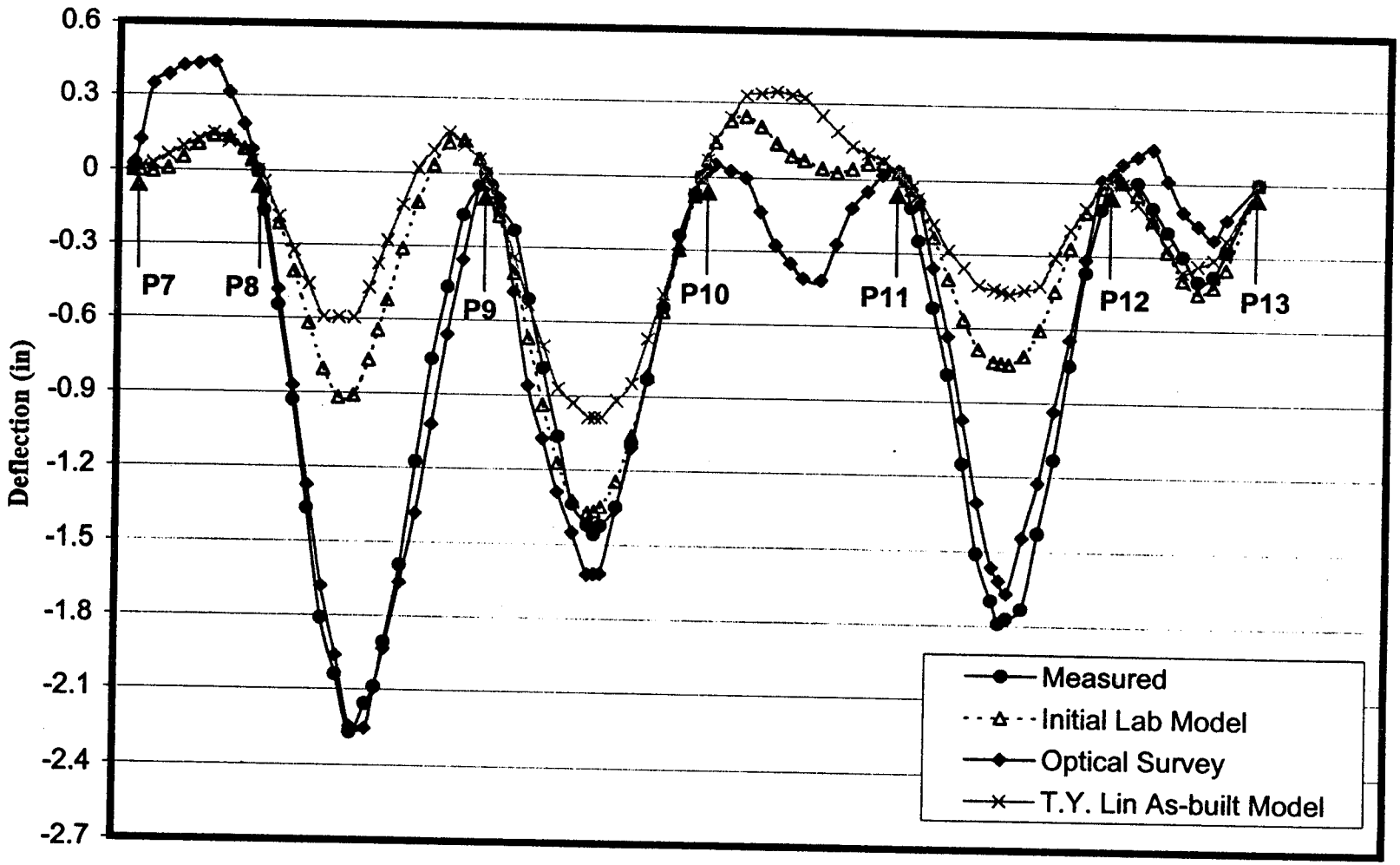

Figure 6.2: Long term deflection of initial lab model (3/95-6/97)

6.2.4.1 Relative humidity

Relative humidity has a large effect on the creep and shrinkage strain. Increasing the relative humidity will substantially decrease both the creep and shrinkage strains.

In the field, the recorded humidity varied over a one year period from 72% to 94% as shown in Figure 6.3. The relative humidity inside the box girder had an annual average of 83.3%, while that outside the box girder averaged 86%. The relative humidity used in SFRAME was 85%. The resulting effect on the 3-day shrinkage prediction is shown in Figure 5.17. The effect on the 3, 28 and 90-day creep predictions are shown in Figures 5.12, 5.13, and 5.14. It should be noted that the change in relative humidity significantly affects shrinkage, with a lesser effect on the creep strain.

6.2.4.2 Ambient temperature

The CTL laboratory ambient temperature is held constant at $73 \pm 1^\circ F$ ($23 \pm 1^\circ C$). As shown in Figure 6.4, the range of field ambient temperature for 1995 was from $66^\circ F$ ($19^\circ C$) to $80^\circ F$ ($26^\circ C$) with a one-year average of $74.7^\circ F$ ($23.7^\circ C$) and $74.3^\circ F$ ($23.5^\circ C$) inside and outside the box girder respectively. Hence, no adjustment was made for ambient temperature.

6.2.4.3 Self-weight of the concrete

A typical self-weight of normal weight plain concrete is 145pcf. The SFRAME model does not include the 3 feet 1inch high barriers on both sides of the bridge deck in its

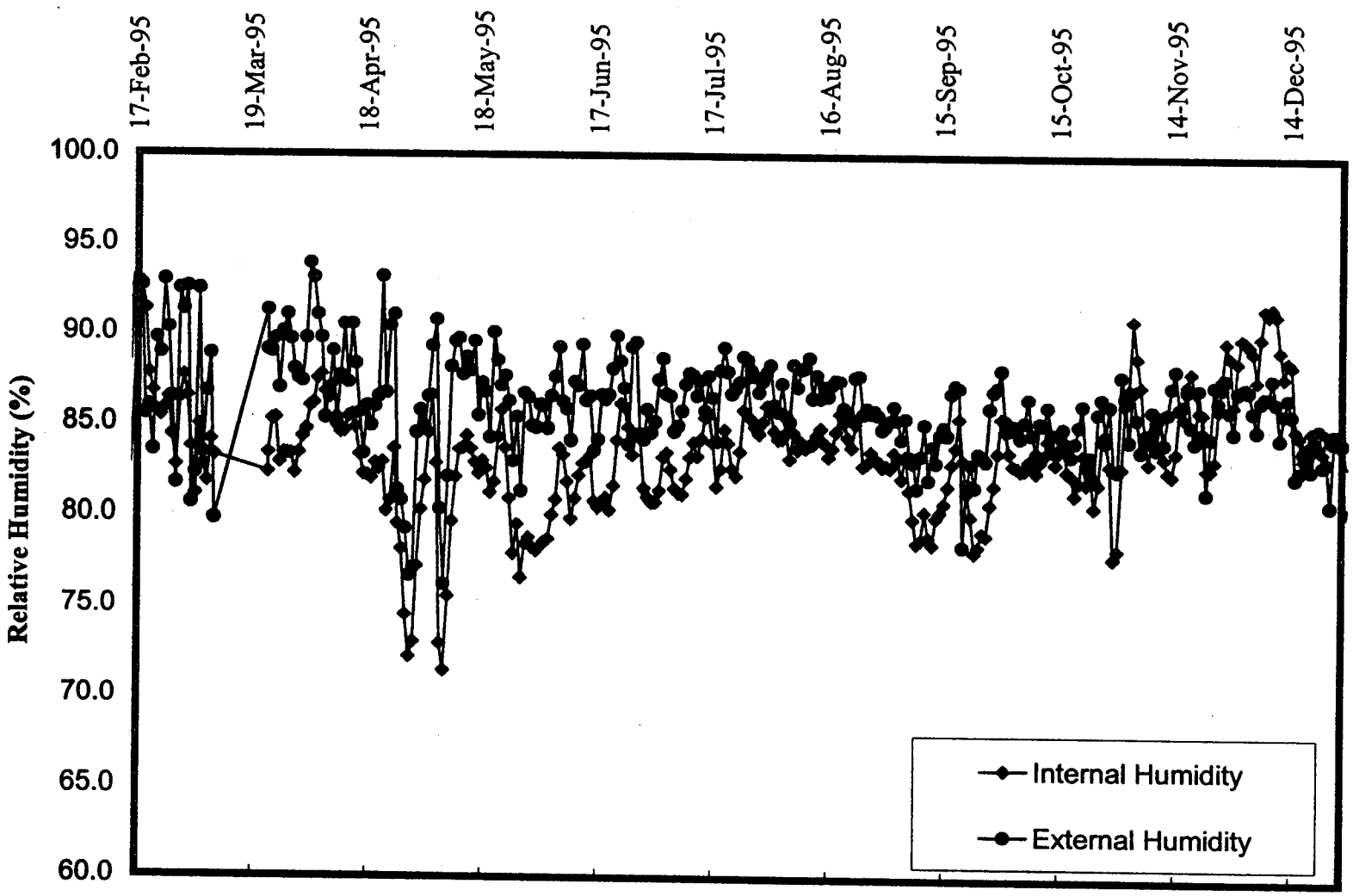

Figure 6.3: One-year relative humidity

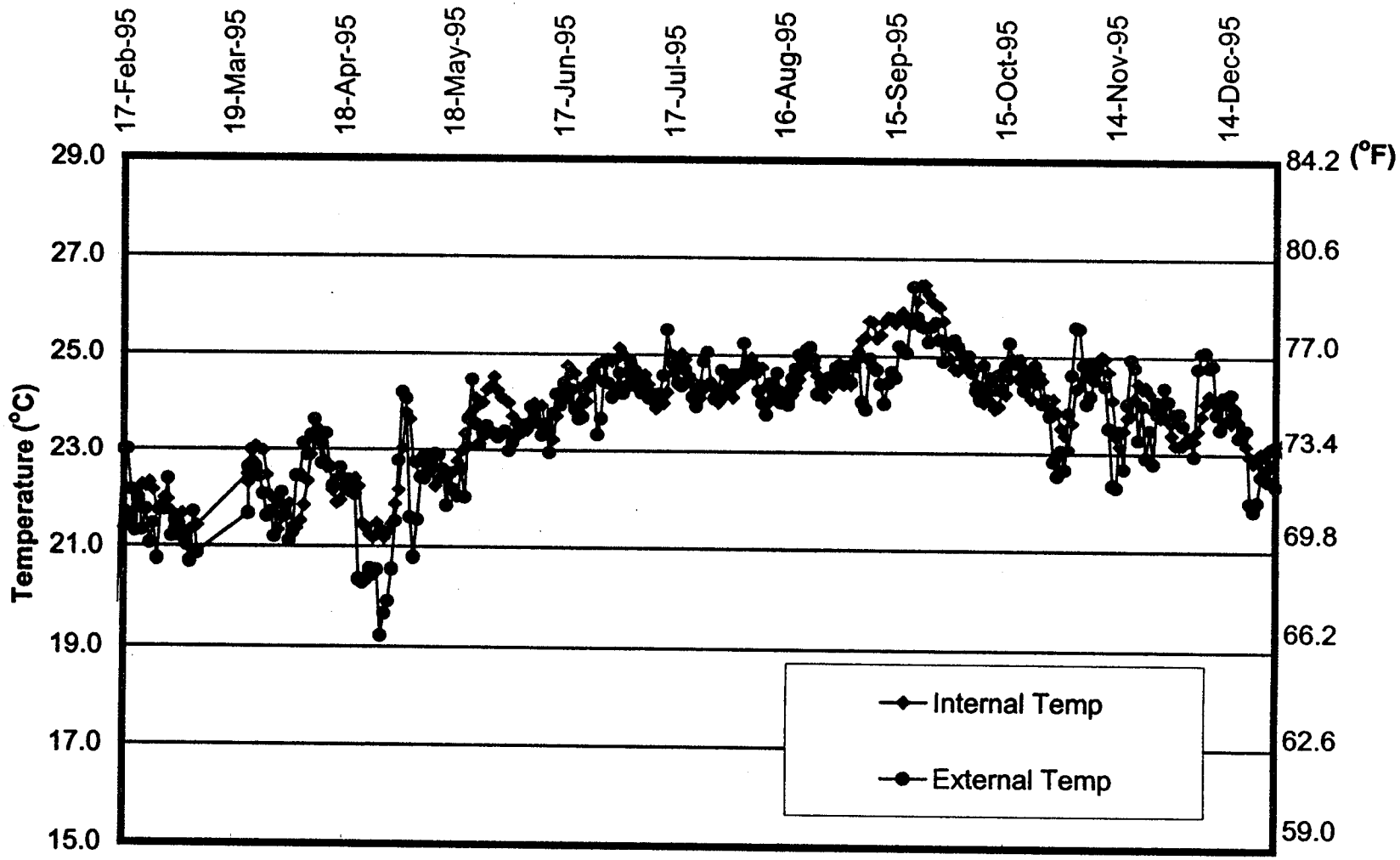

Figure 6.4: One-year temperature

section properties as shown in Figure 5.4. Anchorage blocks for the span tendons and the concrete encasement of utility lines under the North cantilever slab are also not included. In addition, to include the effect of reinforcing and of any over-pouring of the stem and slab thicknesses, the T.Y. Lin As-built model assumed a concrete self-weight of 155 pcf. To improve the analytical prediction, the self-weight of concrete was increased to 165pcf.

6.2.4.4 Volume-to-Surface area ratio

The volume-to-surface area (V/S) ratio for the laboratory cylinders (6 inch diameter by 12 inch long) is 1.5 inch. The corresponding ratio for the viaduct box girder varies from 6.35 to 8.55 in. with the variation in cross-section shape. Therefore, an average V/S ratio of 7.5 is used to calculate the creep and shrinkage strains in the lab material model of SFRAME. The adjusted creep predictions were developed for concrete 3, 28 and 90-day loading as shown in Figures 6.5, 6.6 and 6.7 respectively. The adjusted shrinkage prediction is shown in Figure 6.8. Both creep and shrinkage decrease with increasing volume-to-surface area ratio. This is due to slower drying that occurs with a greater volume-to-surface area ratio.

6.2.4.5 Pier concrete material properties

In the T.Y. Lin As-built model, the same concrete properties were assumed for the pier as used for the box girder. However, the average volume-to-surface area (V/S) ratio for the box girder is 7.5 in., while the same ratio for the pier cross-section is approximately 8.5 in.

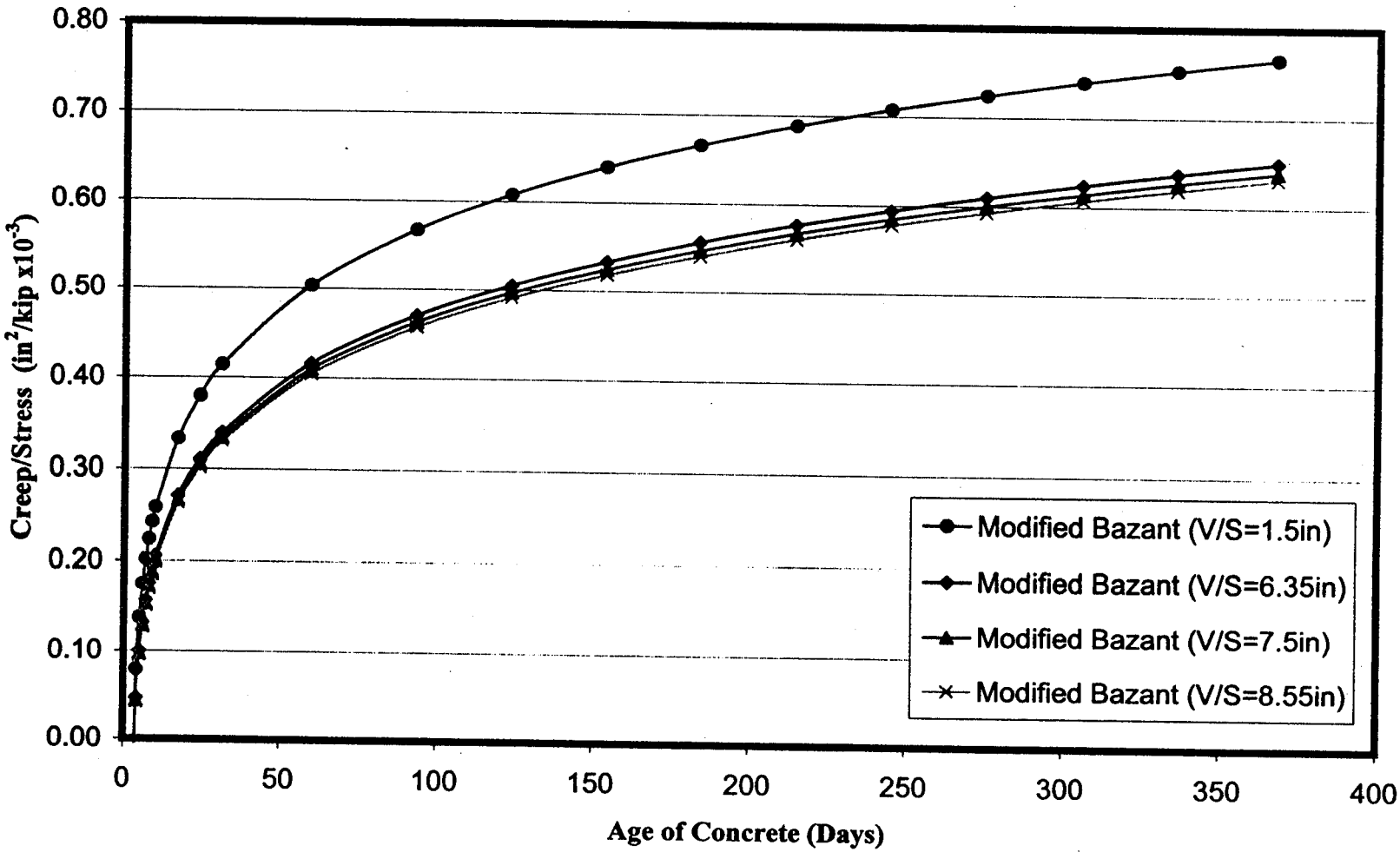

Figure 6.5: Modified Bazant 3-day creep prediction for V/S ratio

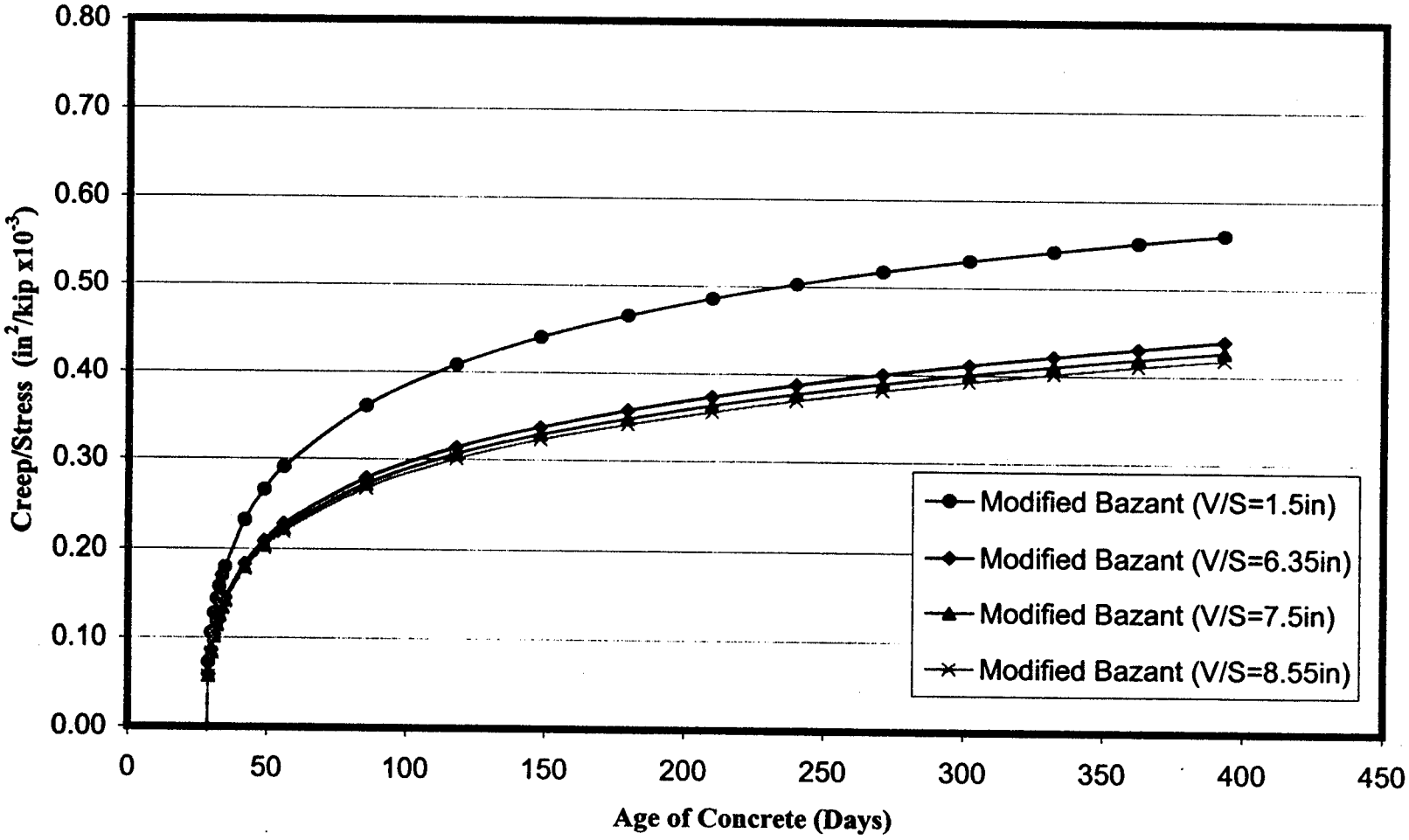

Figure 6.6: Modified Bazant 28-day creep prediction for V/S ratio

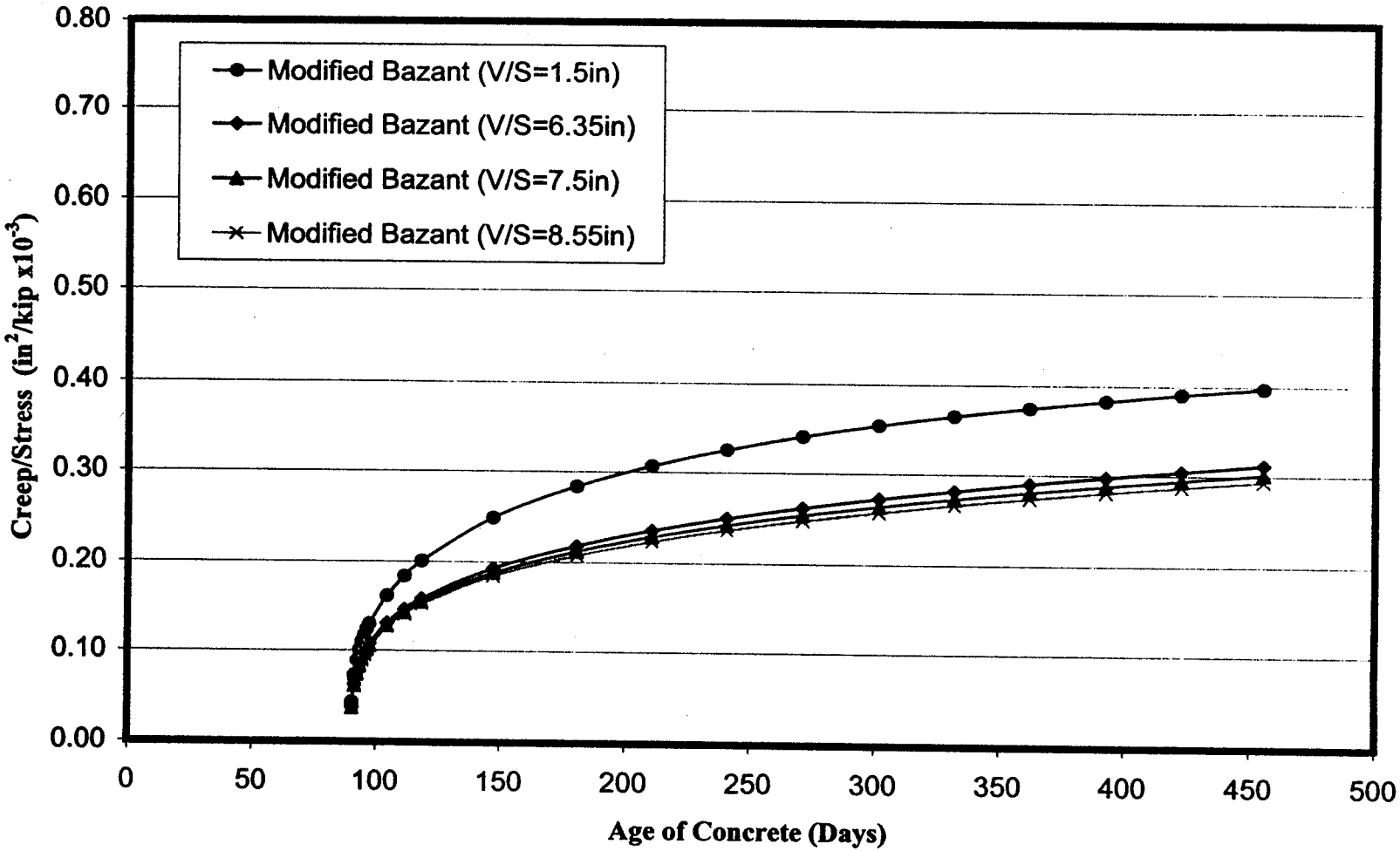

Figure 6.7: Modified Bazant 90-day creep prediction for V/S ratio

Therefore, different creep and shrinkage strains for the superstructure and piers were considered in the SFRAME lab material model. This change affects the absolute deflection of the box girder, but has only a minor effect on the normalized long-term defection as shown in Figure 6.9. As explained earlier, the pier shortening is eliminated by normalizing the displacements to zero vertical displacement at the top of the piers.

6.2.4.6 Creep effect

The amount of creep that concrete will exhibit is difficult to estimate accurately unless tests are conducted to determine the creep characteristics. Without specific tests, accuracies of better than ± 30% should not be expected. Even with short term test results, the actual creep under field conditions may still vary by ± 20%. Numerous SFRAME trials with creep scaling factors from 0.7 to 1.3 were performed. The best prediction of long-term deflection was achieved with a creep scaling factor of 1.3.

6.2.4.7 Isolating the effect of shrinkage

In order to isolate the effect of shrinkage on the box girder deflections, all other parameters were set to zero. Creep, self-weight of the bridge and prestressing effects are therefore not considered in this SFRAME analysis. This was achieved by defining the creep scaling factor as zero, self-weight of the concrete as zero, and prestressing ratio as zero. Figure 6.10 shows the long-term deflection due to the shrinkage effect alone. It is interesting to note that spans P8-9 and P10-11 show upward deflection, while span P9-10, between the fixed piers at P9 and P10, moves downward.

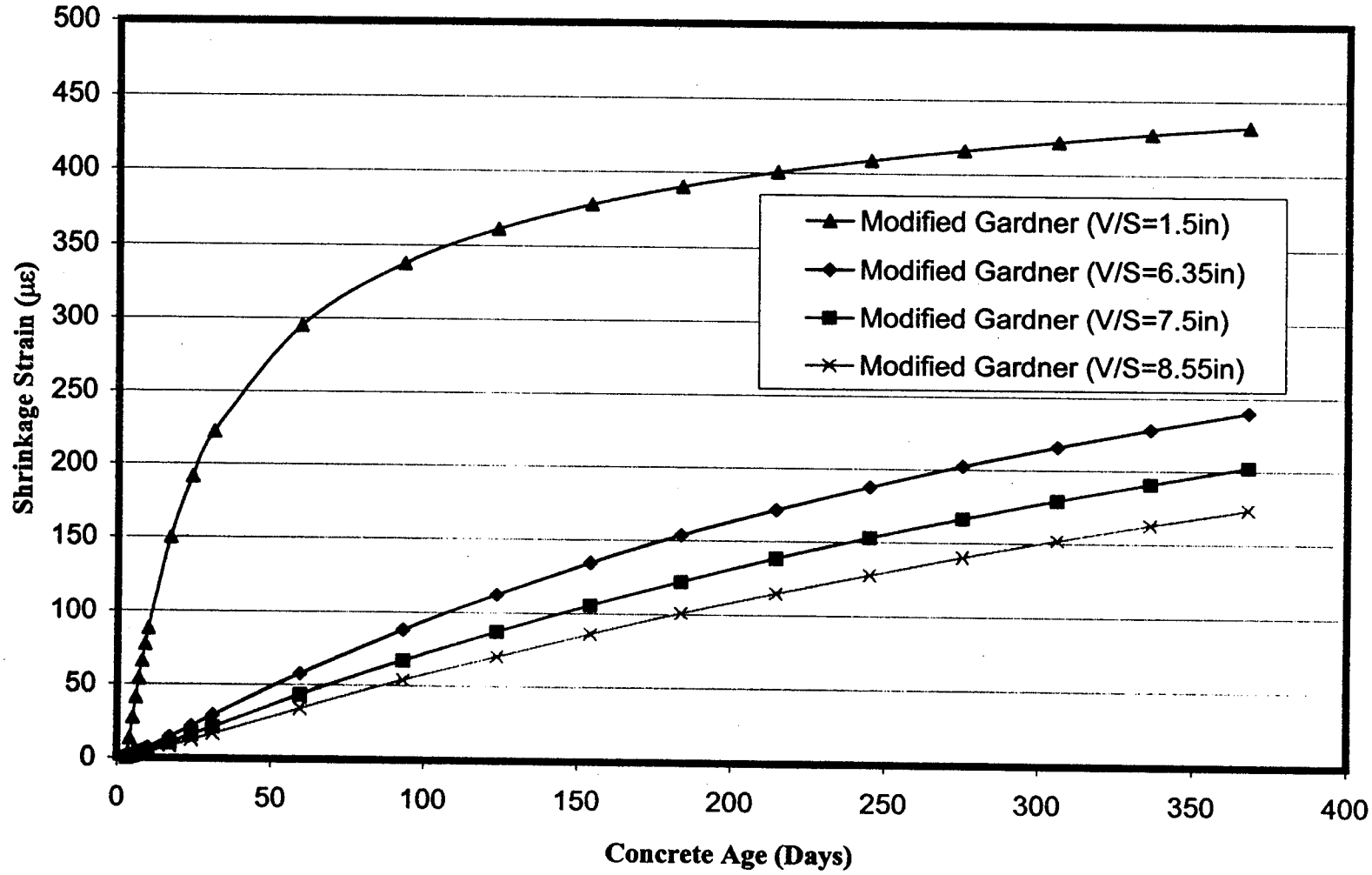

Figure 6.8: Modified Gardner 3-Day shrinkage prediction for V/S ratio

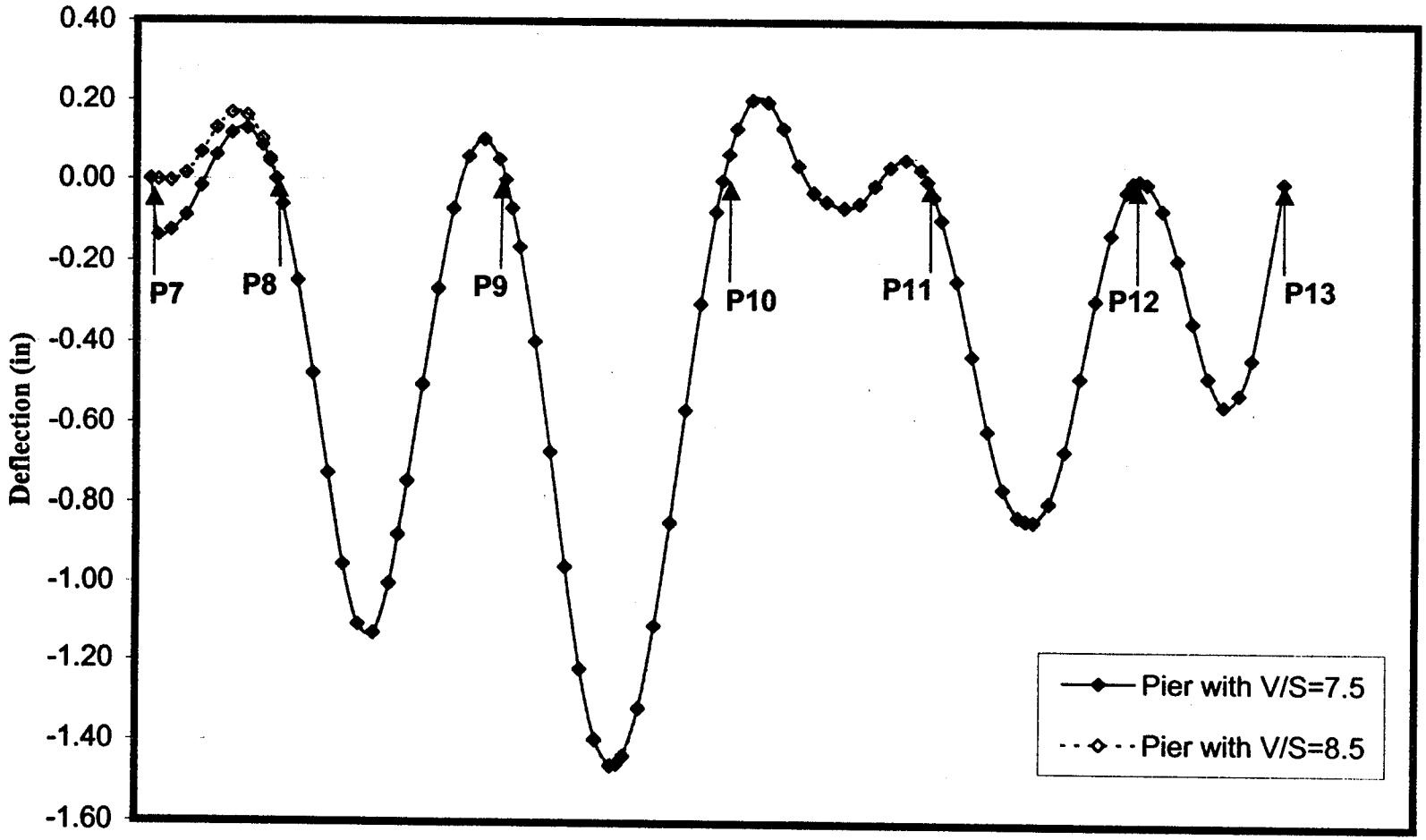

Figure 6.9: Long term deflection (3/95-6/97) effect of pier V/S ratio

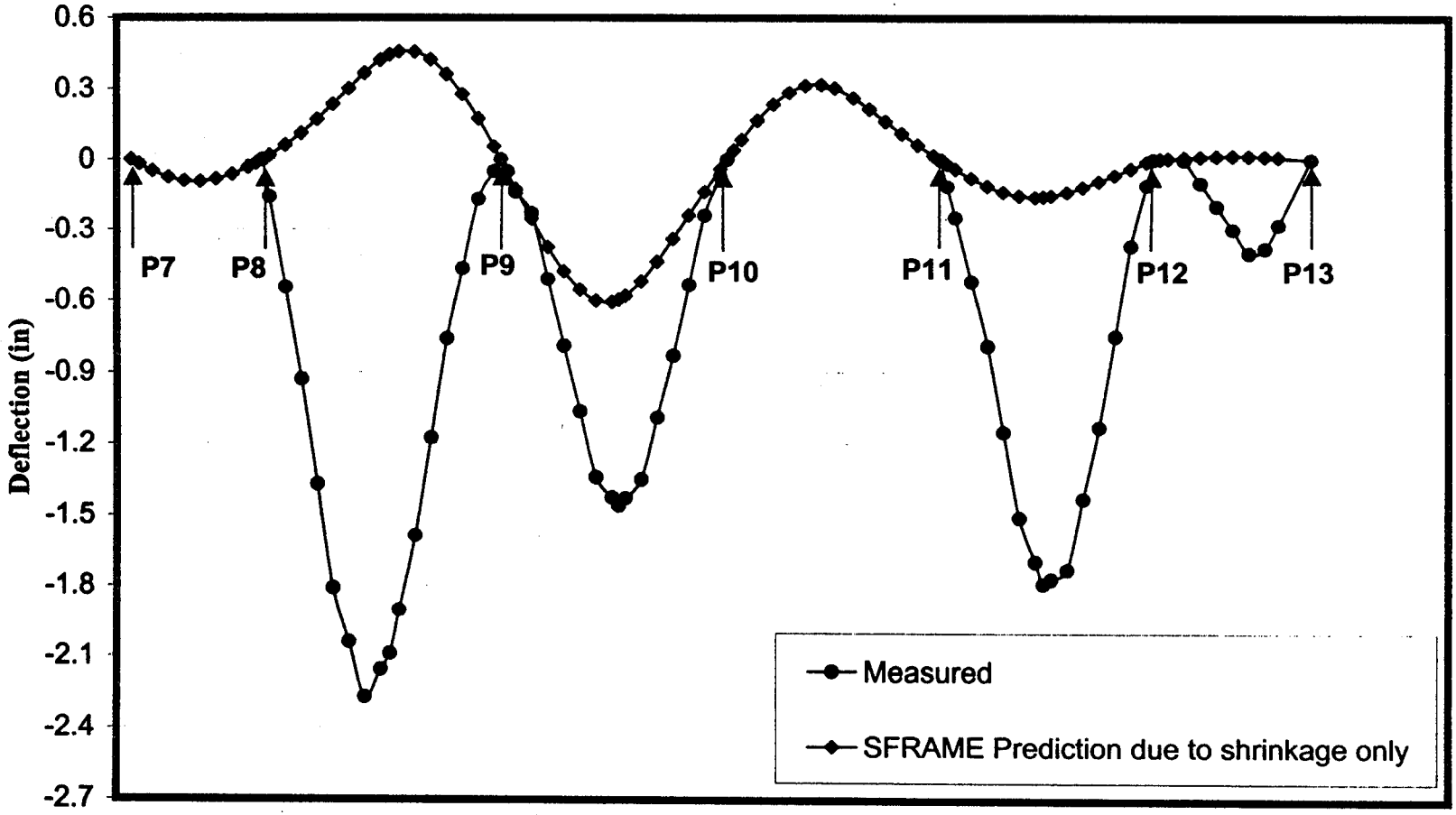

Figure 6.10: Long term deflection due to shrinkage effect only (3/95-6/97)

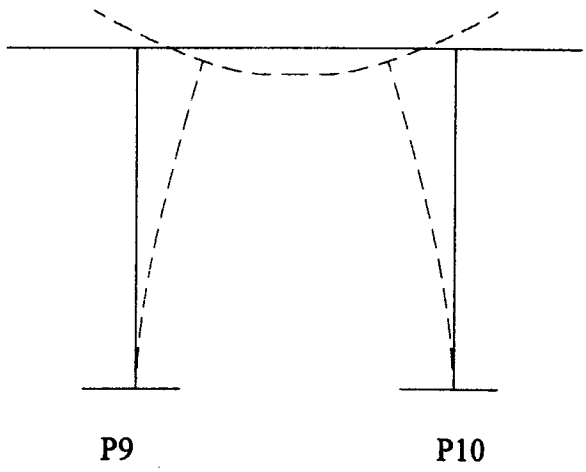

Figure 6.11: Deformation of pier 9 & 10

As shown in Figure 6.11, shrinkage-induced span shortening pulls the fixed piers together, resulting in inward rotations at the top of the piers. The effect is downward deflection between the piers, but upward deflection in the adjacent spans. This influence decreases with distance from the fixed piers. This could in part explain the large deflections predicted by the T.Y. Lin As-built model for span P9-10 compared with the longer span P8-9. In order to improve the analytical prediction, a shrinkage scaling factor of 0.7 was used.

6.2.4.8 Isolating the effect of prestressing

In order to investigate the influence of prestressing on the deflections, two conditions were analyzed. First, all prestress was removed from the analysis. The prestressing can be removed by defining the prestressing ratio as zero in SFRAME. Thus the bridge is subjected to self-weight, creep and shrinkage only. The resulting absolute deflection is shown in Figure 6.12. Second, only the prestress was considered. This can be achieved

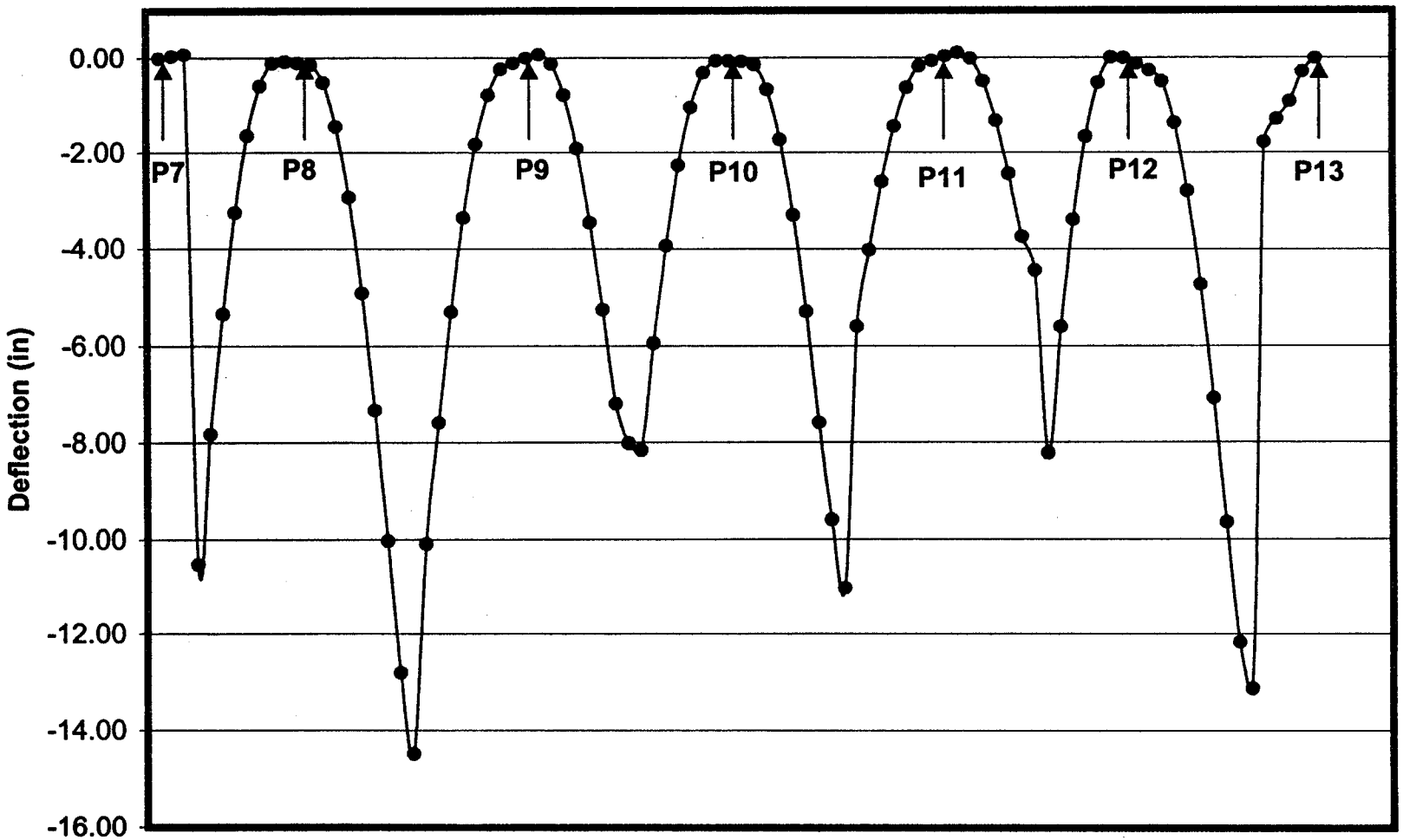

Figure 6.12: Absolute deflection without prestressing (June 97)

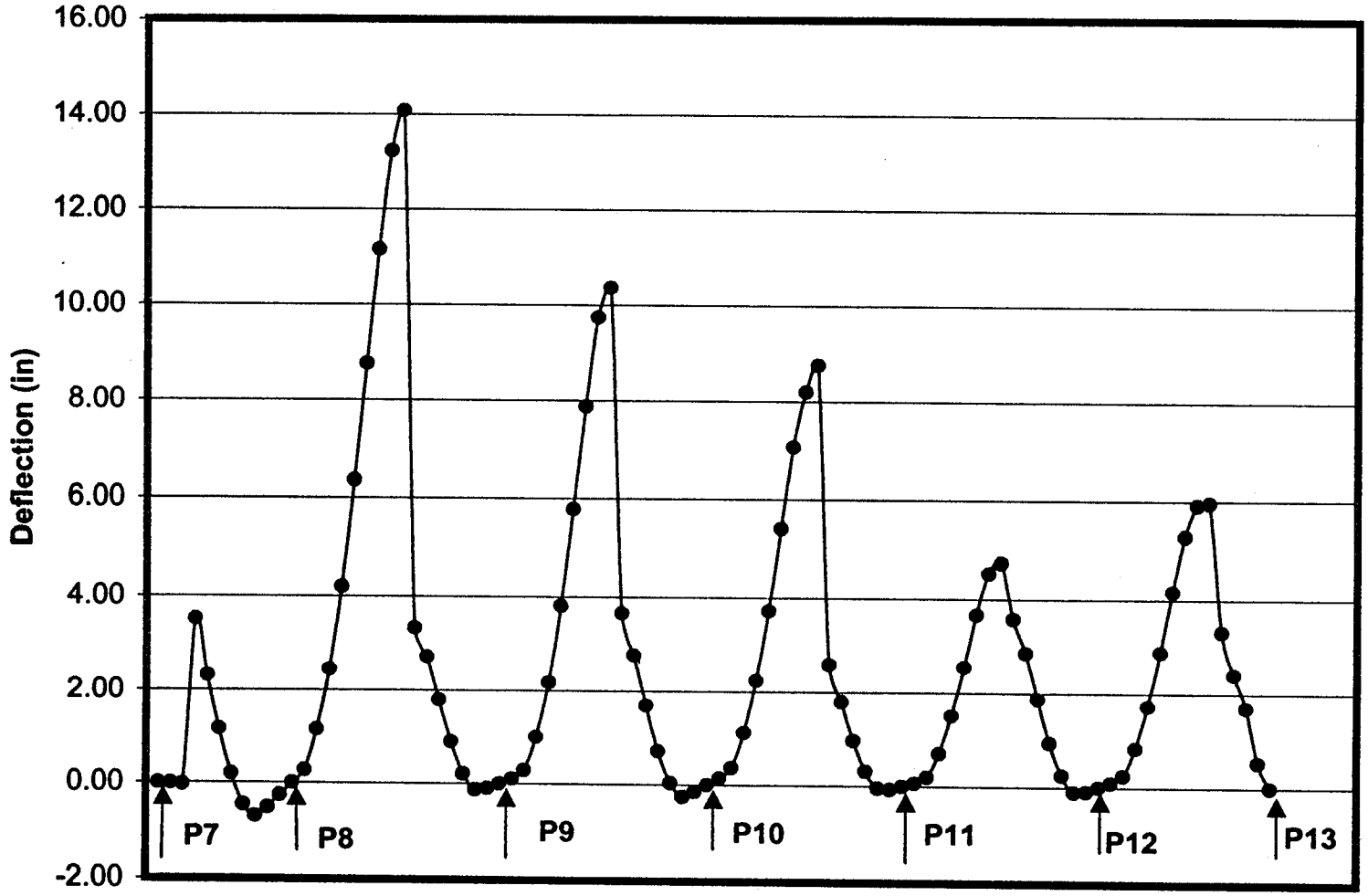

Figure 6.13: Absolute deflection due to prestress alone (June 97)

in SFRAME by defining creep and shrinkage scaling factors and self-weight of the concrete as zero. The resulting absolute deflection is plotted in Figure 6.13. It is noted that prestressing results in an upward deflection, while without prestressing, the bridge shows a downward deflection. The relative deflection can be obtained approximately by subtracting these two absolute deflections. A small error in one or both of these absolute deflections would cause significant differences in the relative deflection. Therefore, it can be noted that the accurate prediction of vertical deflections is complicated by the small difference between these large values.

6.2.4.9 Prestressing loss

Load cells are used to measure the span tendon forces. During tendon stressing, the load cell readings were recorded using a manual readout box. Subsequently, the load cell lead wires were connected to the nearest datalogger with available data for automated reading. As described in Section 3.3 friction at the first anchor plate affected the readings from load cells 1 and 2 during prestressing. In a similar way, the friction has affected the load cell readings during prestress loss, resulting in the step-type plot in Figure 6.14 for load cell 1. The datalogger at section A was unable to read load cell 2 automatically, so manual readings were taken at various intervals. Load cells 3 to 6 recorded smoothly decreasing prestress forces as shown in Figures 6.16 to 6.19.

SFRAME gives the predicted tendon segment force in its idealized tendon force profile. Extracting the prestress forces in the span tendons and comparing them with the load cell

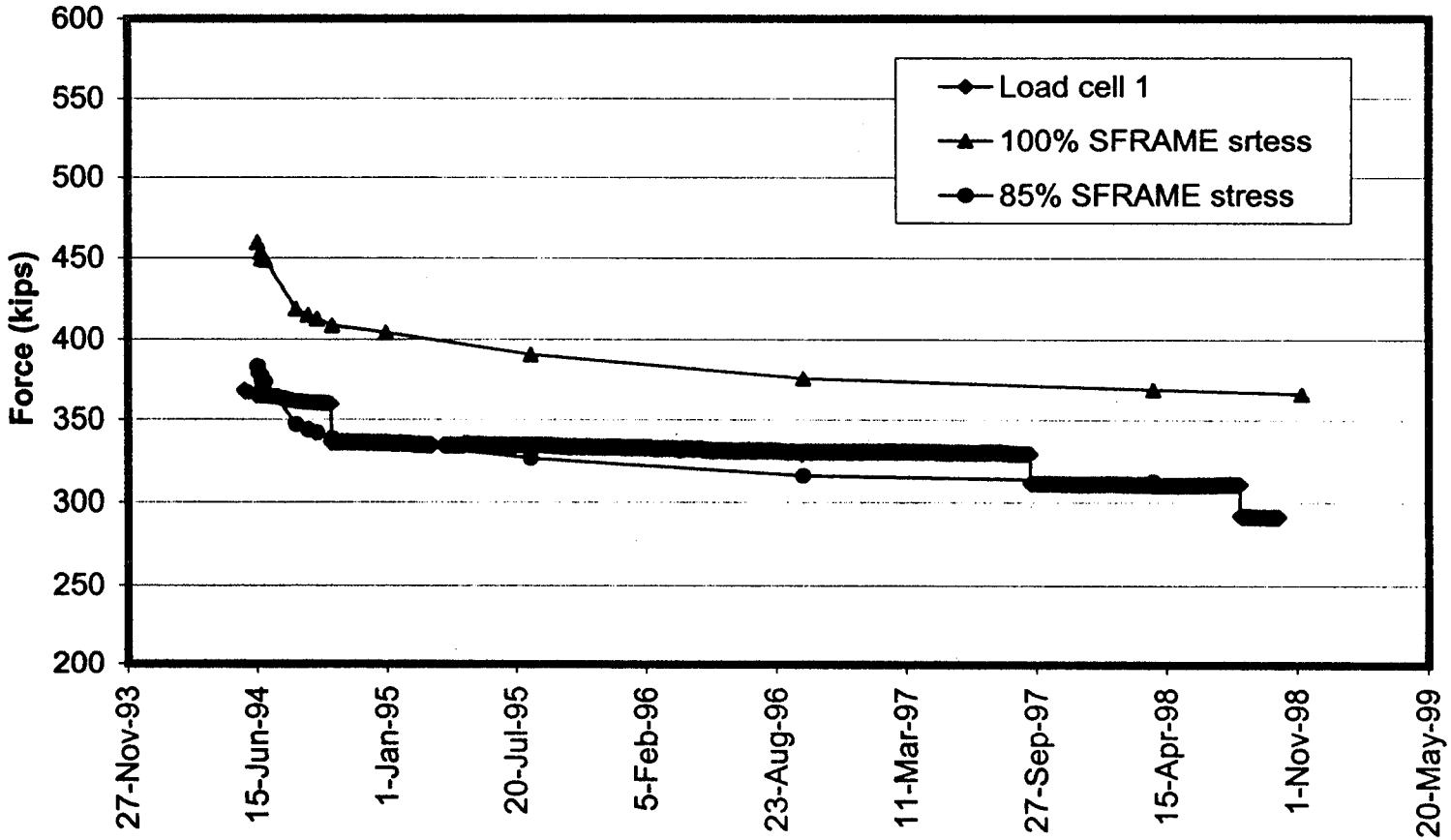

Figure 6.14: Prestress loss prediction for load cell 1

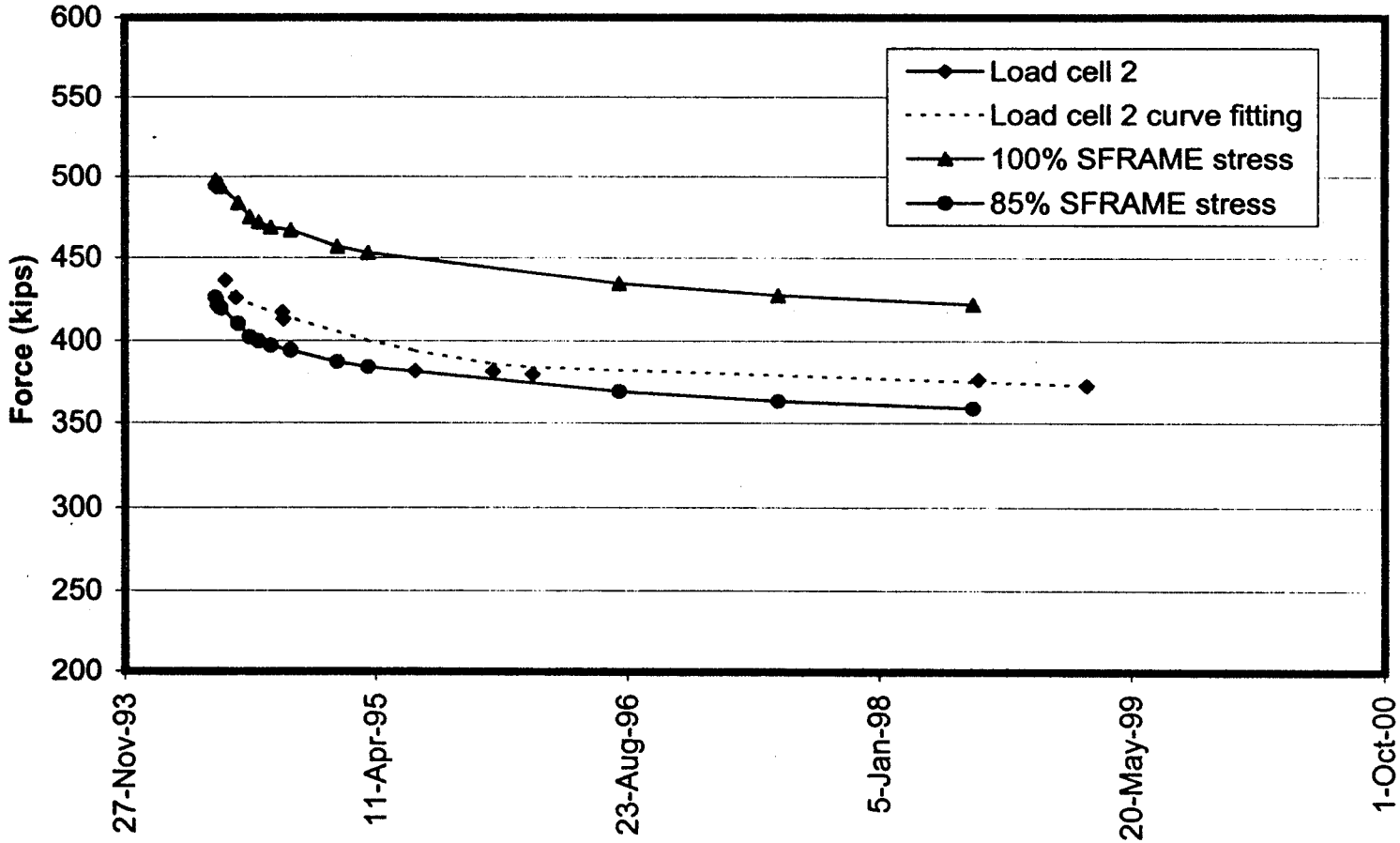

Figure 6.15: Prestress loss prediction for load cell 2

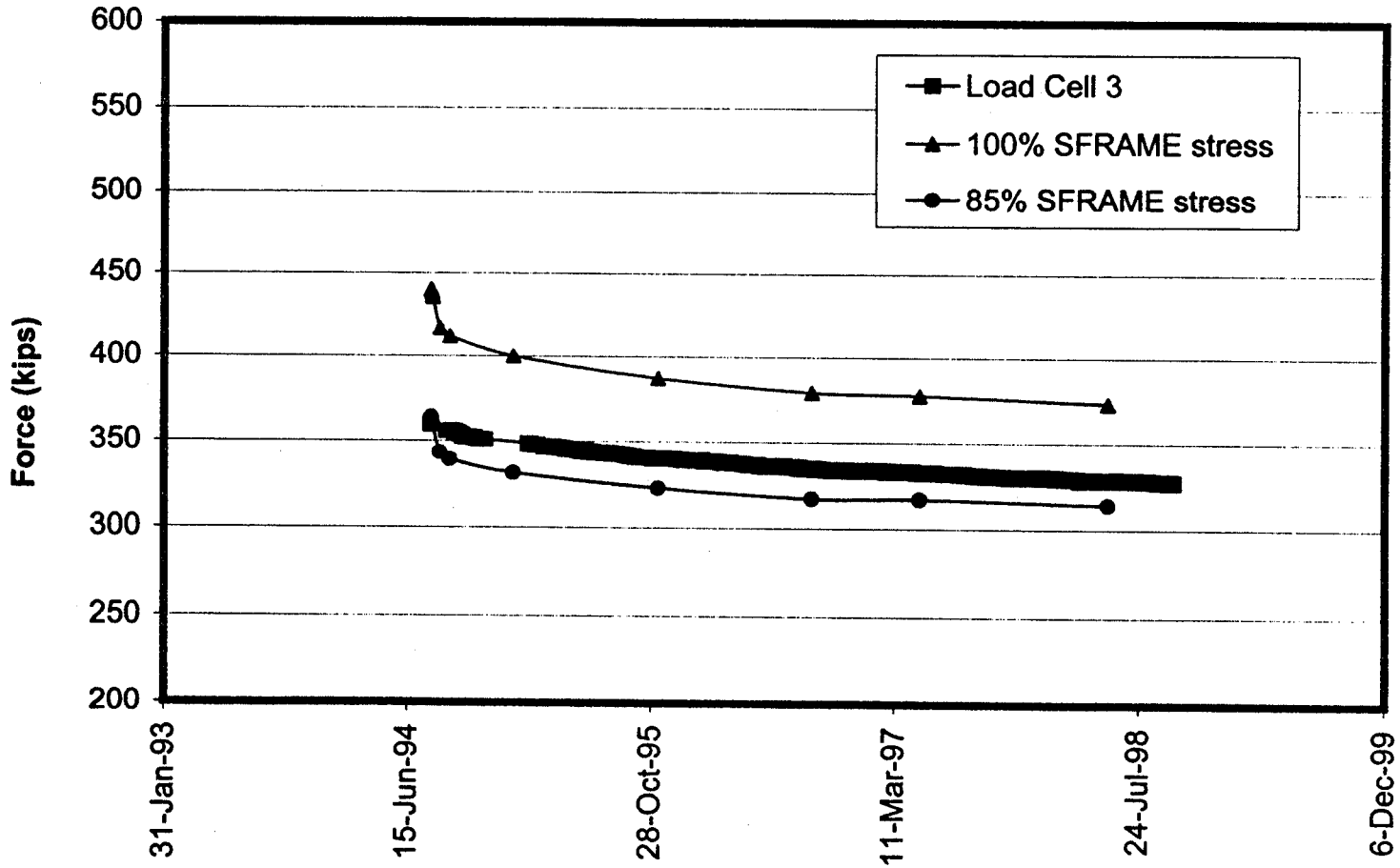

Figure 6.16: Prestress loss prediction- load cell 3

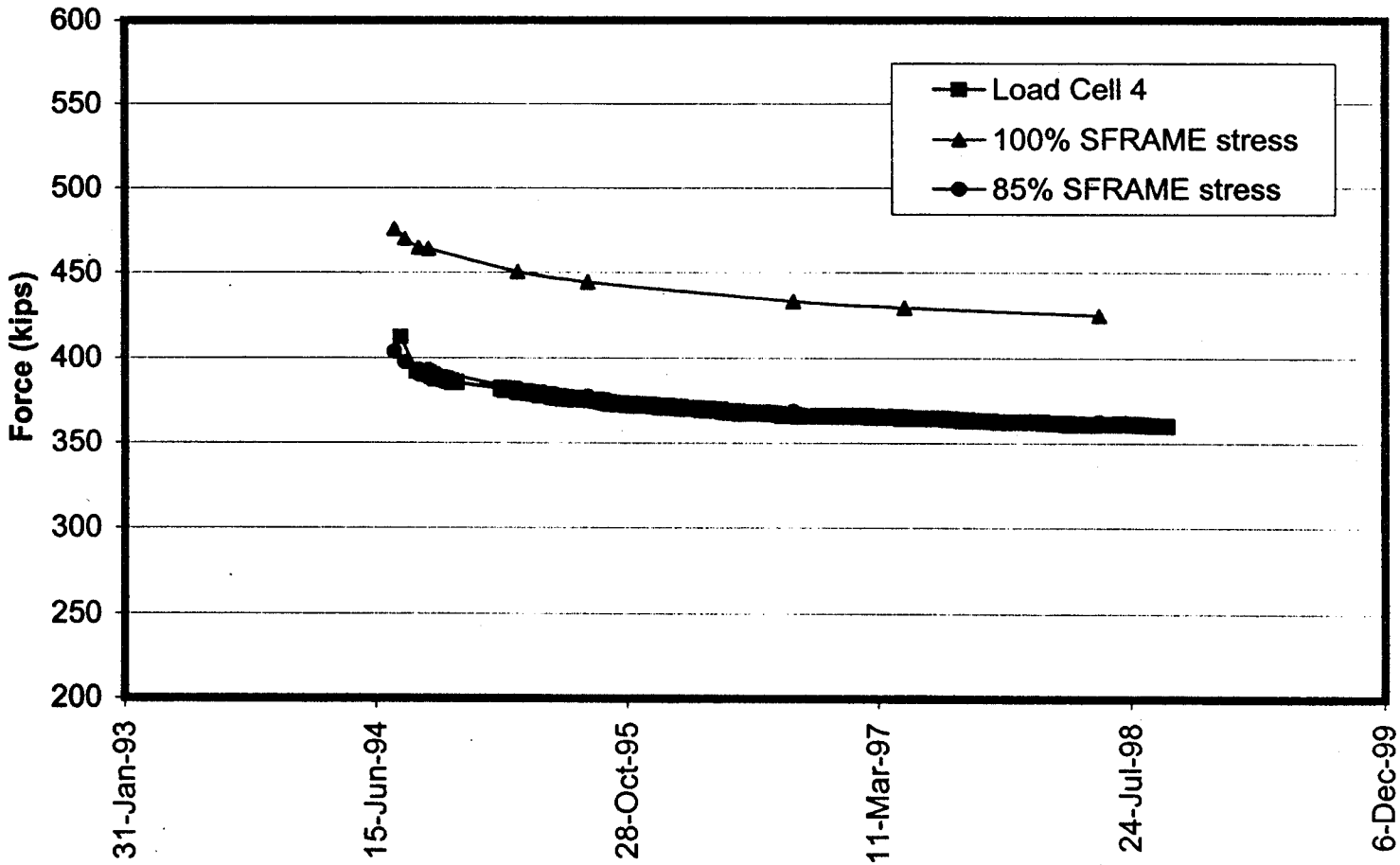

Figure 6.17: Prestress loss prediction- load cell 4

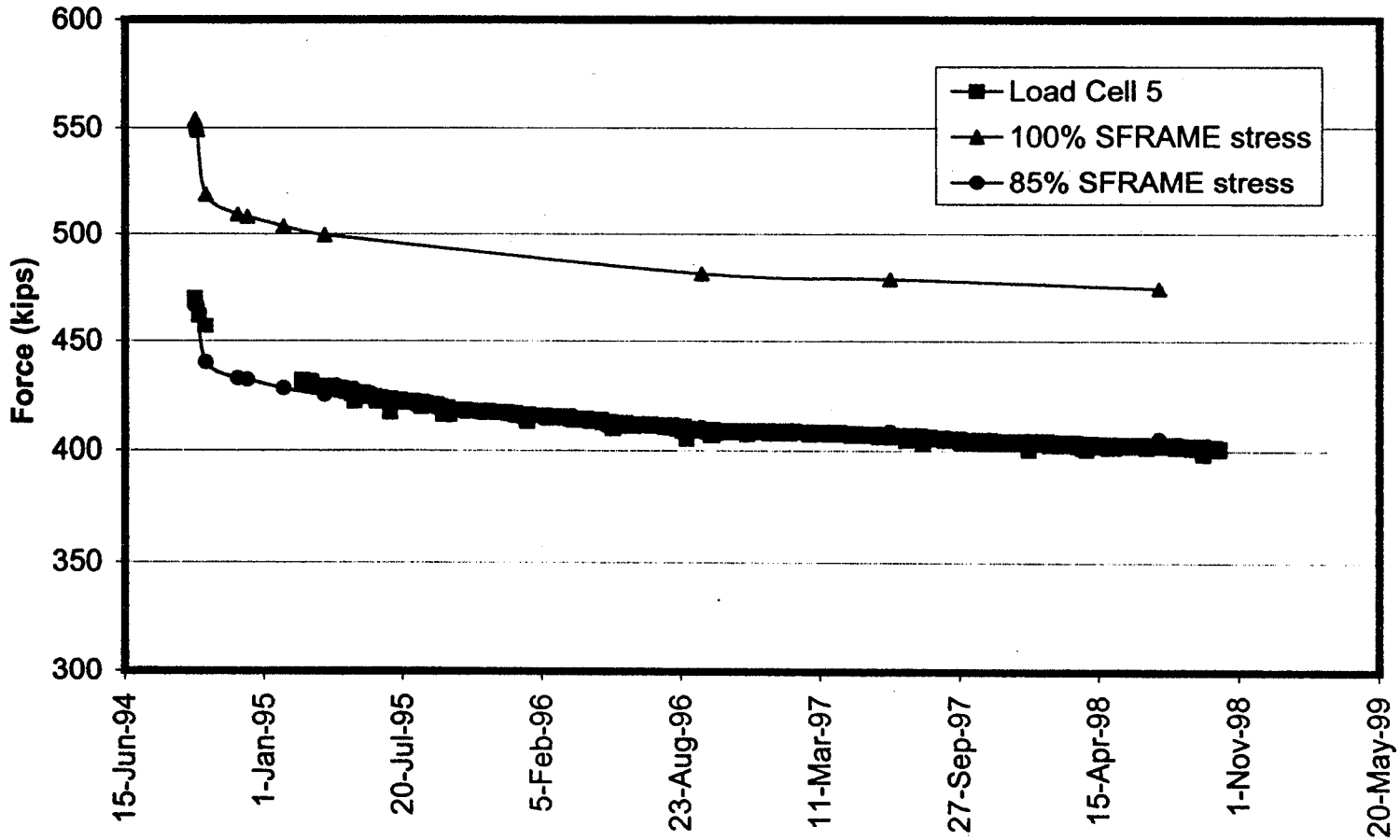

Figure 6.18: Prestress loss prediction- load cell 5

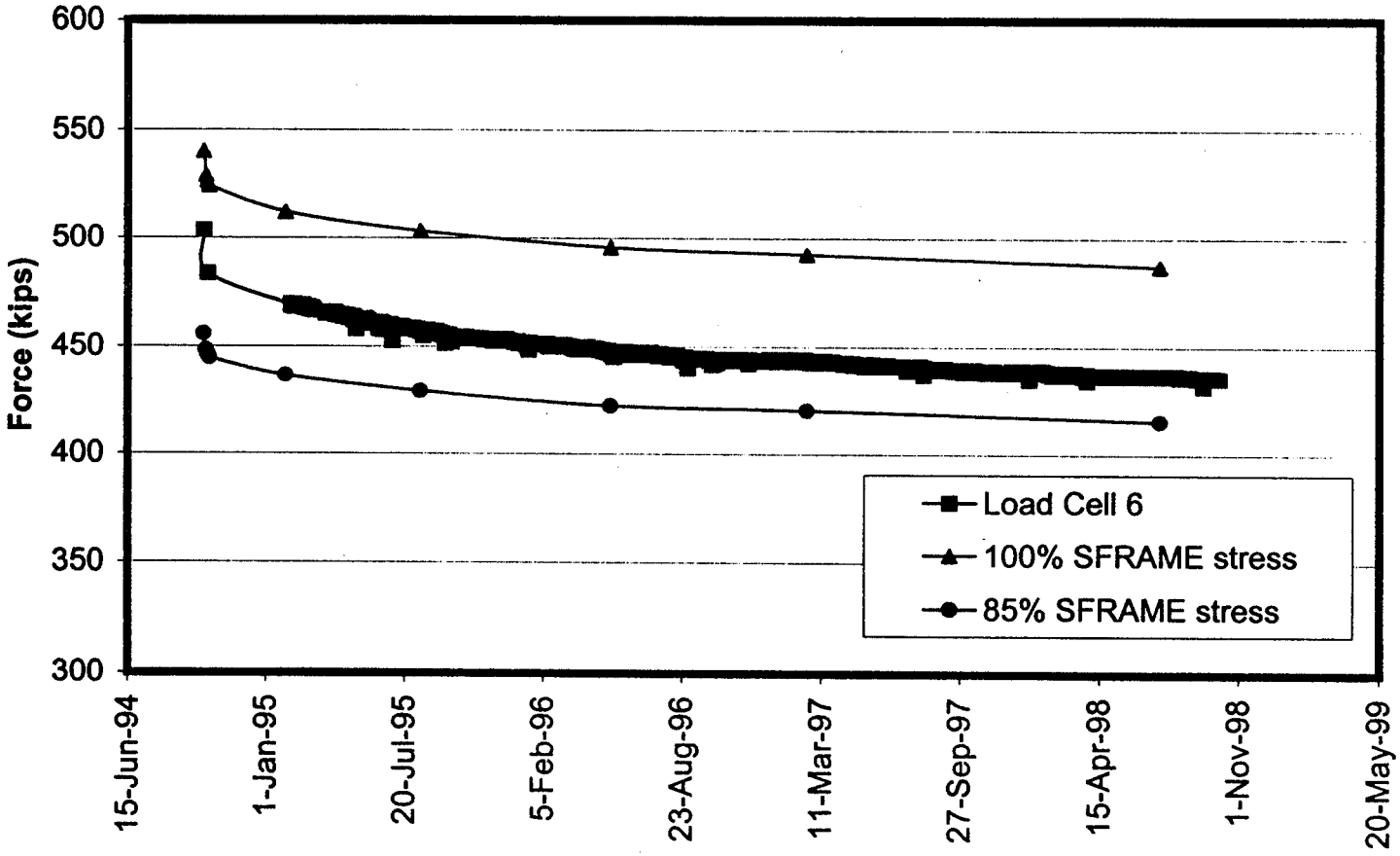

Figure 6.19: Prestress loss prediction- load cell 6

readings shows fairly good agreement between the shapes of the prestress loss plots. However, the field measurements were always lower than SFRAME predictions as shown in Figures 6.14 through 6.19. As discussed in Section 3.3, discrepancies in load cell readings during prestressing lead to an investigation of the various load cells and prestressing rams used in the construction. The results of this investigation by Russell and Hunter are included in "Instrumentation of the North Halawa Valley Viaduct: Progress Report" (Shushkewich et al, 1998). The study indicated that four load cells on the fixed ends of span tendons indicated forces that were 82% to 89% of the theoretical values. After numerous SFRAME analyses with various values of prestress for continuity, cantilever and span tendons, a prestressing reduction factor of 0.85 was assumed for all prestress tendons. Figures 6.14 to 6.19 show the effect of this reduction factor on the SFRAME prestress loss predictions. The resulting predictions are generally in better agreement with the measured values.

6.3 Final lab model

The intent of this parametric study was to investigate the effects of variations in the model parameters. In order to better predict the long term deflection over the two year period from March 1995 to June 1997, parameter adjustments were made as follows:

Creep scaling factor of 1.3

Shrinkage scaling factor of 0.7

Pretressing reduction factor of 0.85

Concrete self-weight of 165 pcf (instead of 155 pcf in initial lab model)

Same concrete constitutive model for the box-girder and piers

The resulting model is referred to as the final lab model. Figure 6.25 displays span deflection between March 29th,1995 and June 19th, 1997 using this final lab model. It shows good improvement compared to the initial lab model and T.Y. Lin As-built models except for span P12-13. The parameters used in this final lab model have been selected to produce the best possible overall deflection. However, without selecting different properties for each span, it is not possible to match the deflections in each span. The variability of properties in the actual construction lead to variations from one span to the next.

Using the final lab model, deflections were computed for various intervals after the initial survey in March 1995. The predicted deflections are plotted in Figures 6.20 through 6.28 together with the corresponding site measurements for June 1995, September 1995, May 1996, August 1996, October 1996, June 1997, December 1997, March 1998 and November 1998. In September 1996, a 2 inch thick overlay was poured over the entire roadway of Unit 2IB. Figures 6.23 and 6.24 show the deflected shape before and after placing the 2 inch overlay. As noted earlier, the deflections for the longest span P8-9 match the site measurements almost exactly. These SFRAME results confirm the design parameters chosen for the final lab model based on the two year deflection from March 1995 to June 1997. This series of plots indicates that with the correct material parameters, SFRAME is able to predict the long-term deflection at any age with reasonable accuracy.

It can therefore be assumed that predictions of future deflections based on the final lab model will be reasonably accurate.

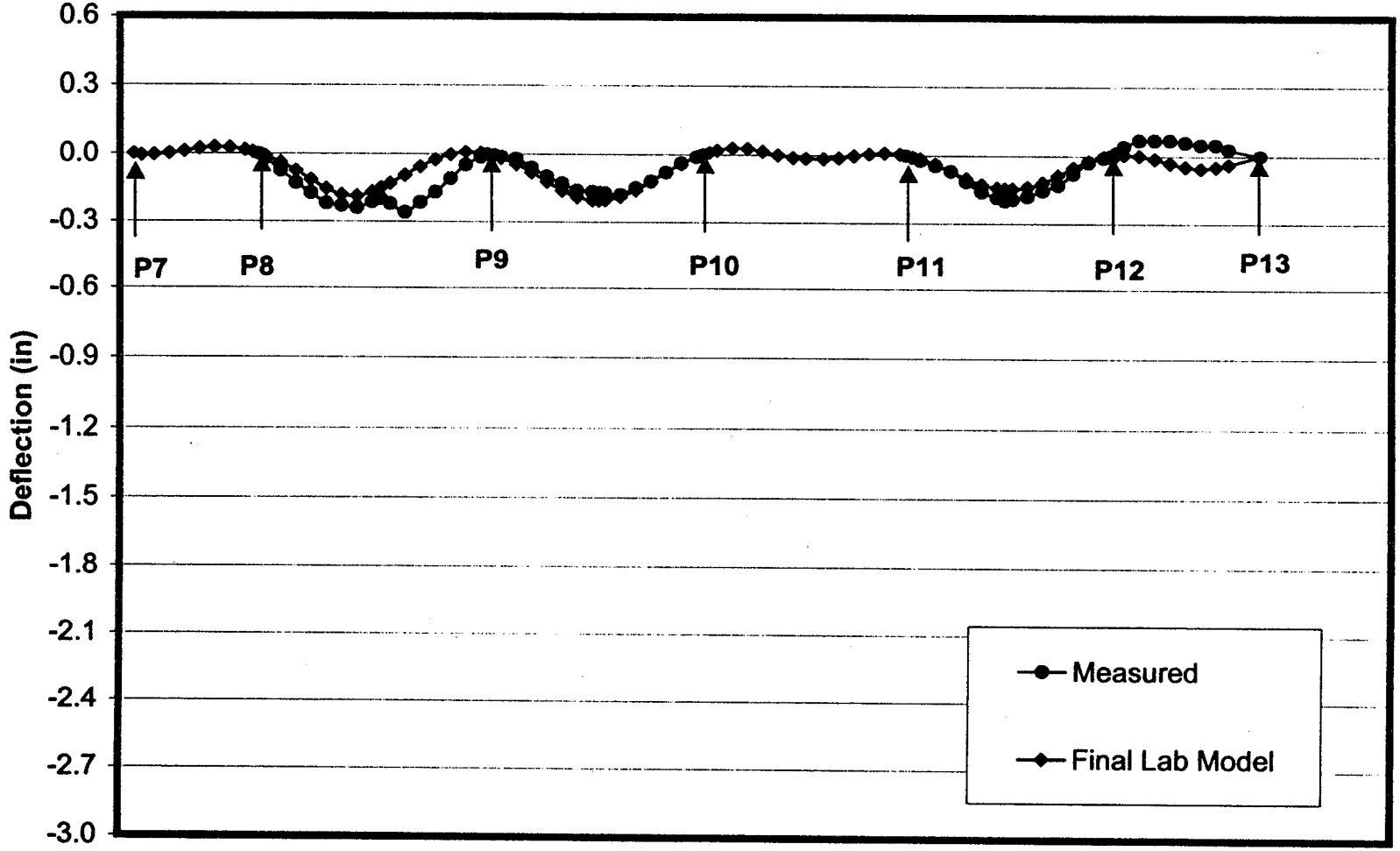

Figure 6.20: Deflection of final lab model (3/95-6/95)

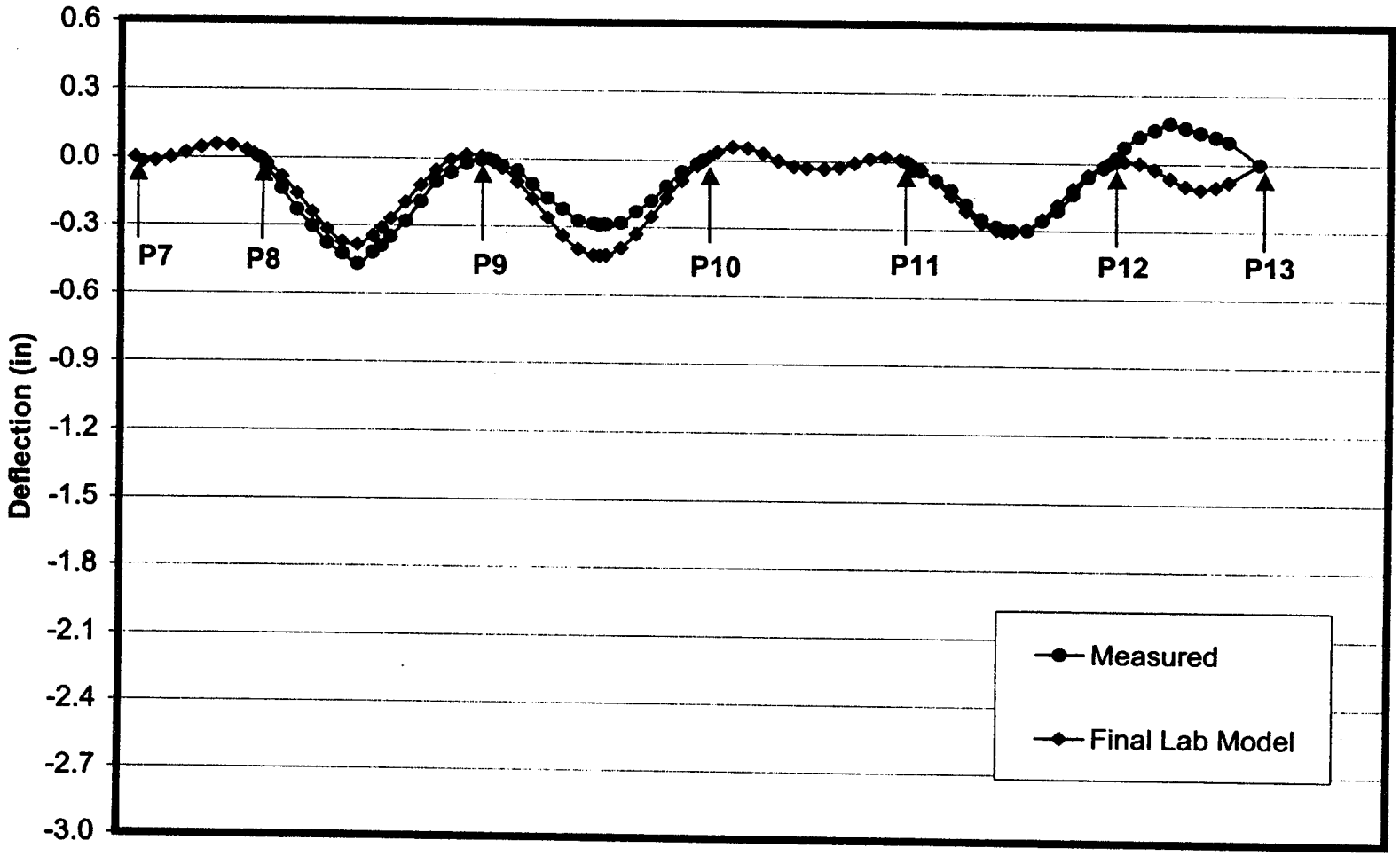

Figure 6.21: Deflection of final lab model (3/95-9/95)

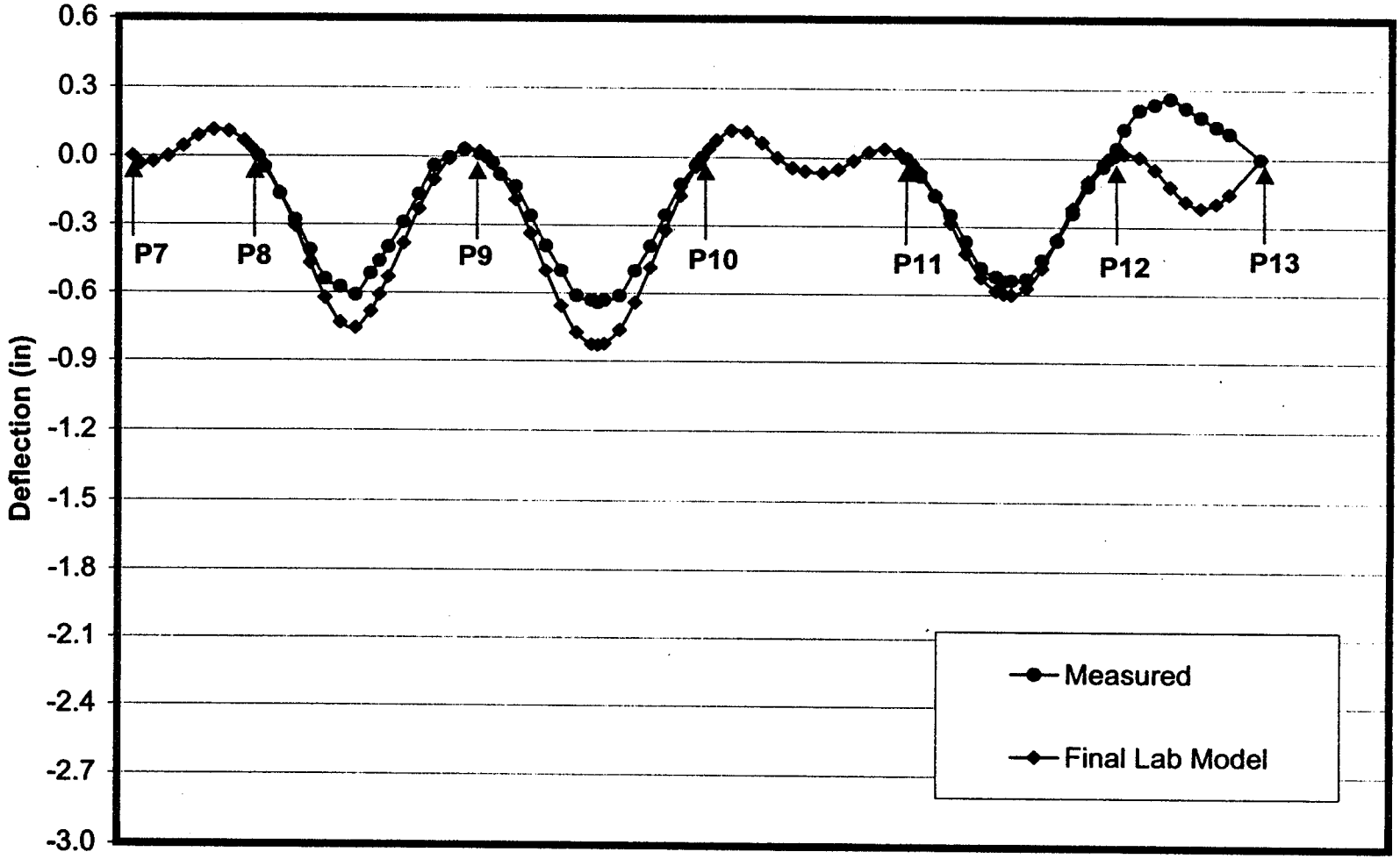

Fiugure 6.22: Deflection of final lab model (3/95-5/96)

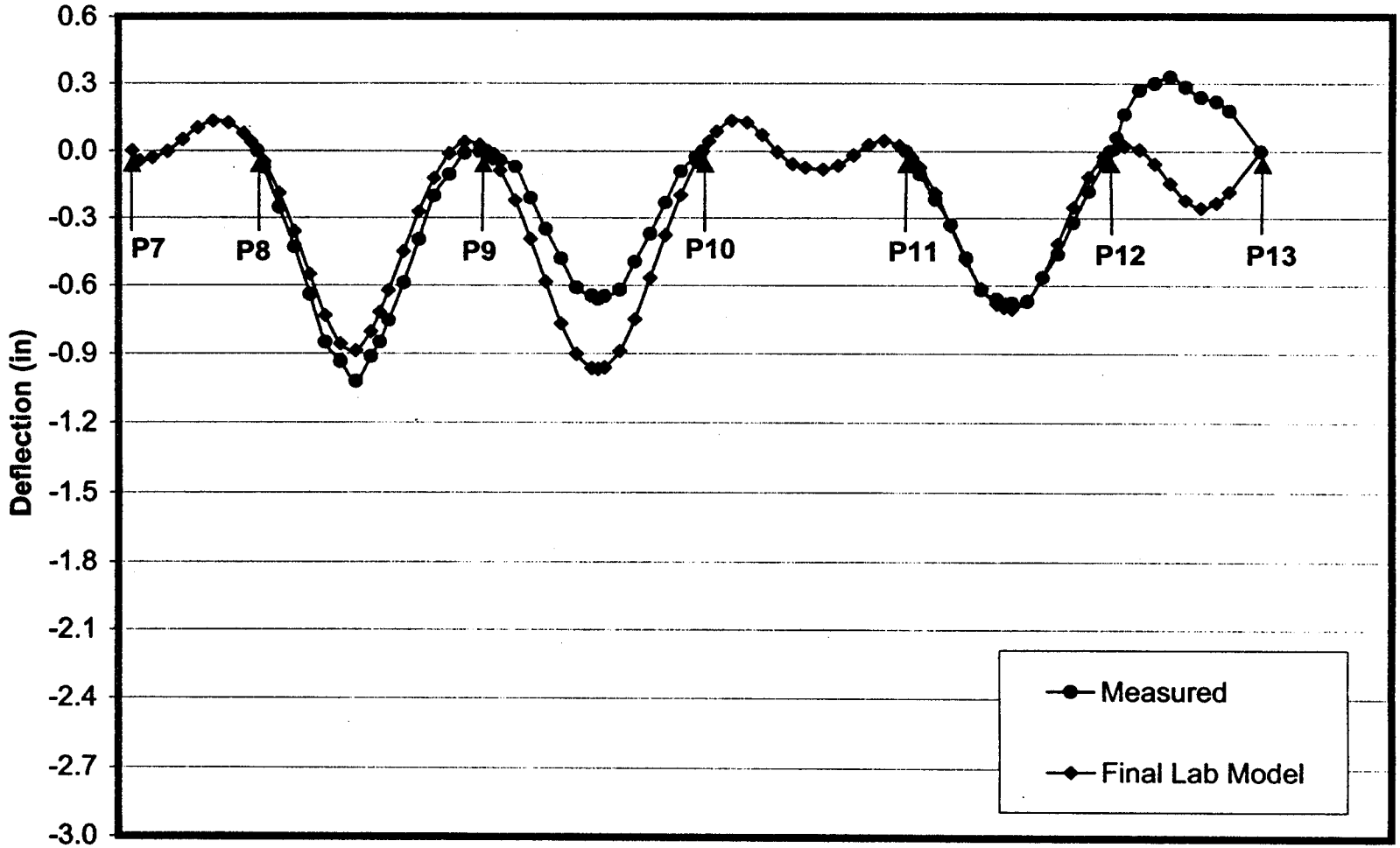

Figure 6.23: Deflection of final lab model (3/95-8/96 before 2" overlay)

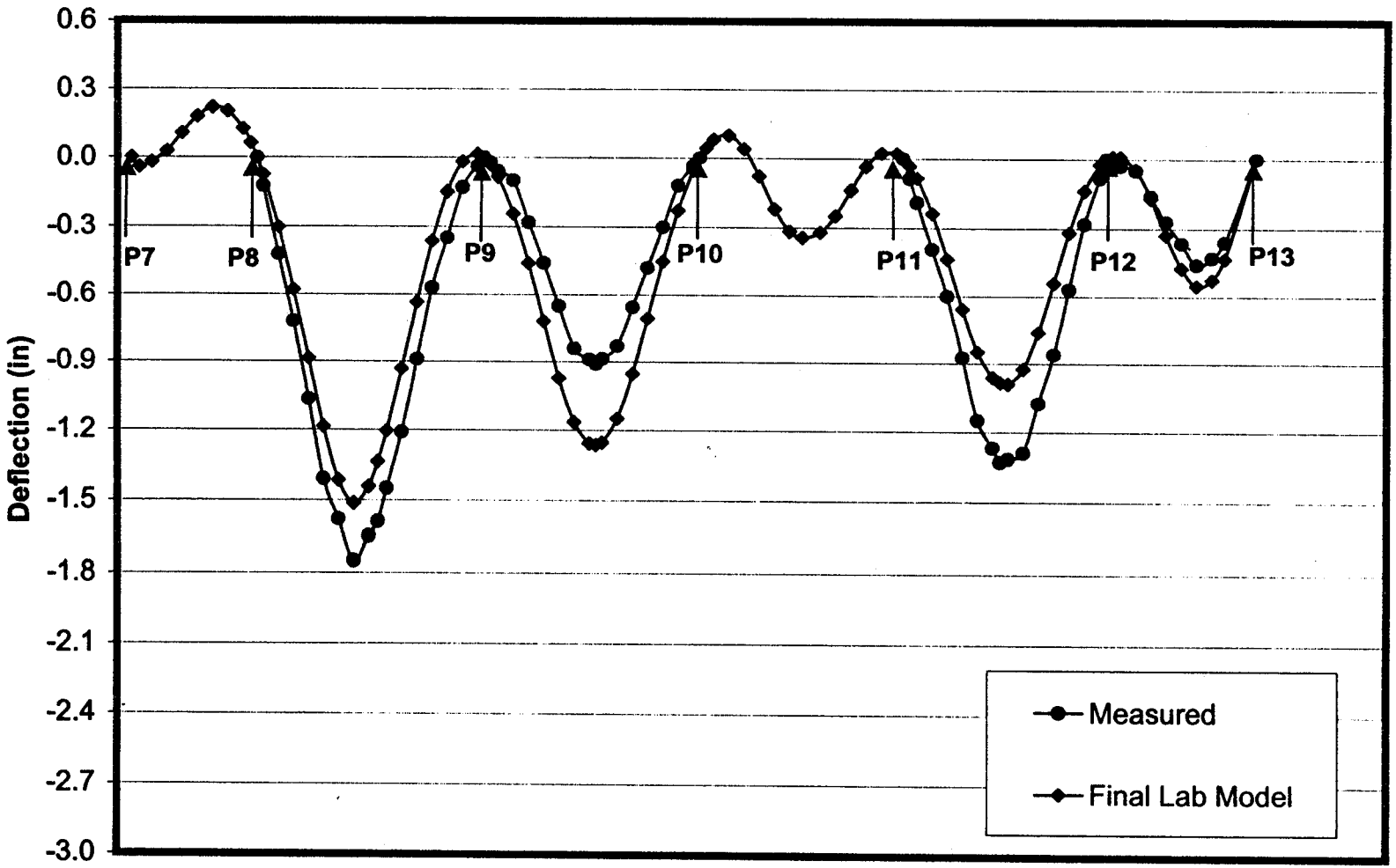

Figure 6.24: Deflection of final lab model (3/95-10/96 after 2" overlay)

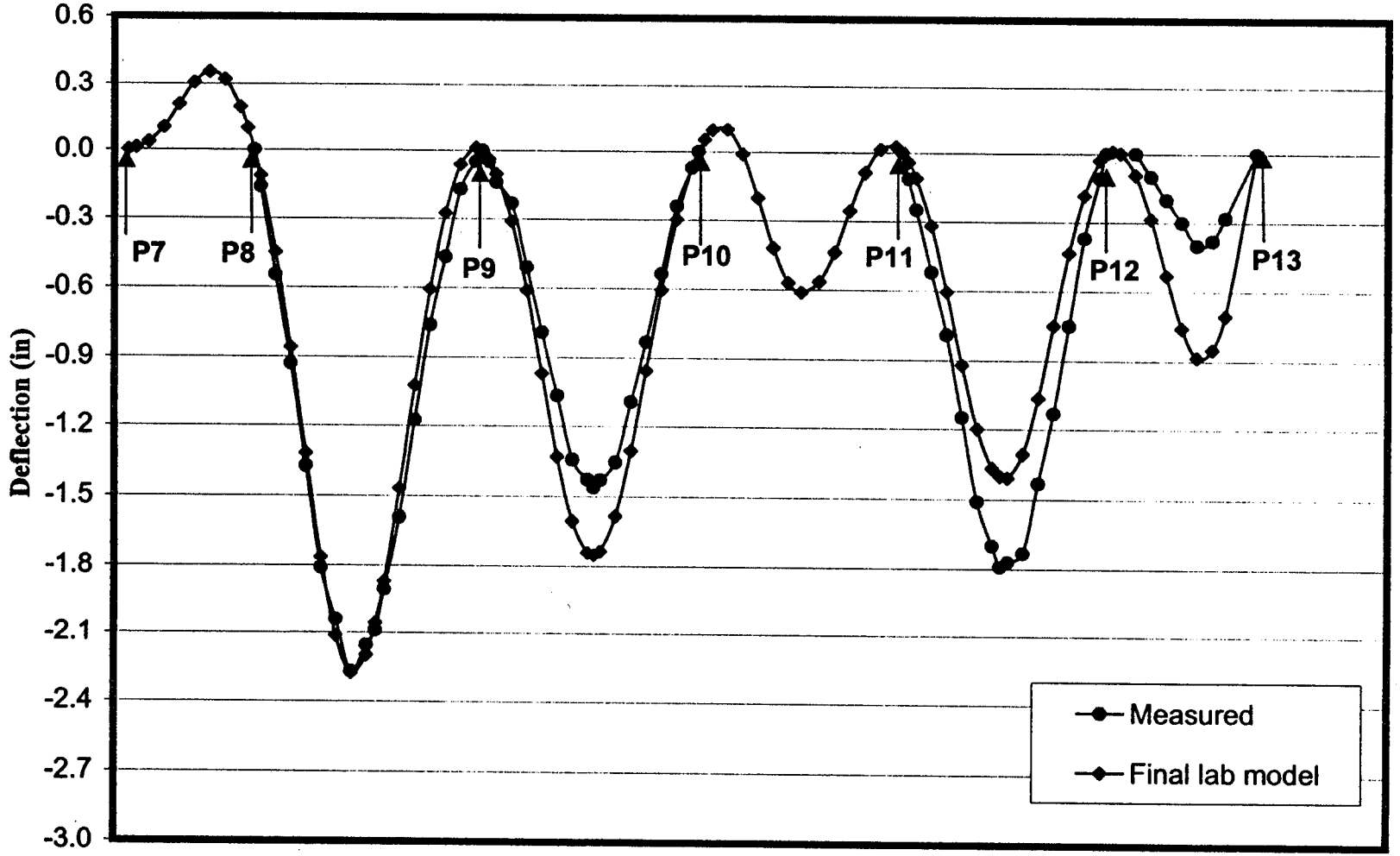

Figure 6.25: Deflection of final lab model (3/95-6/97)

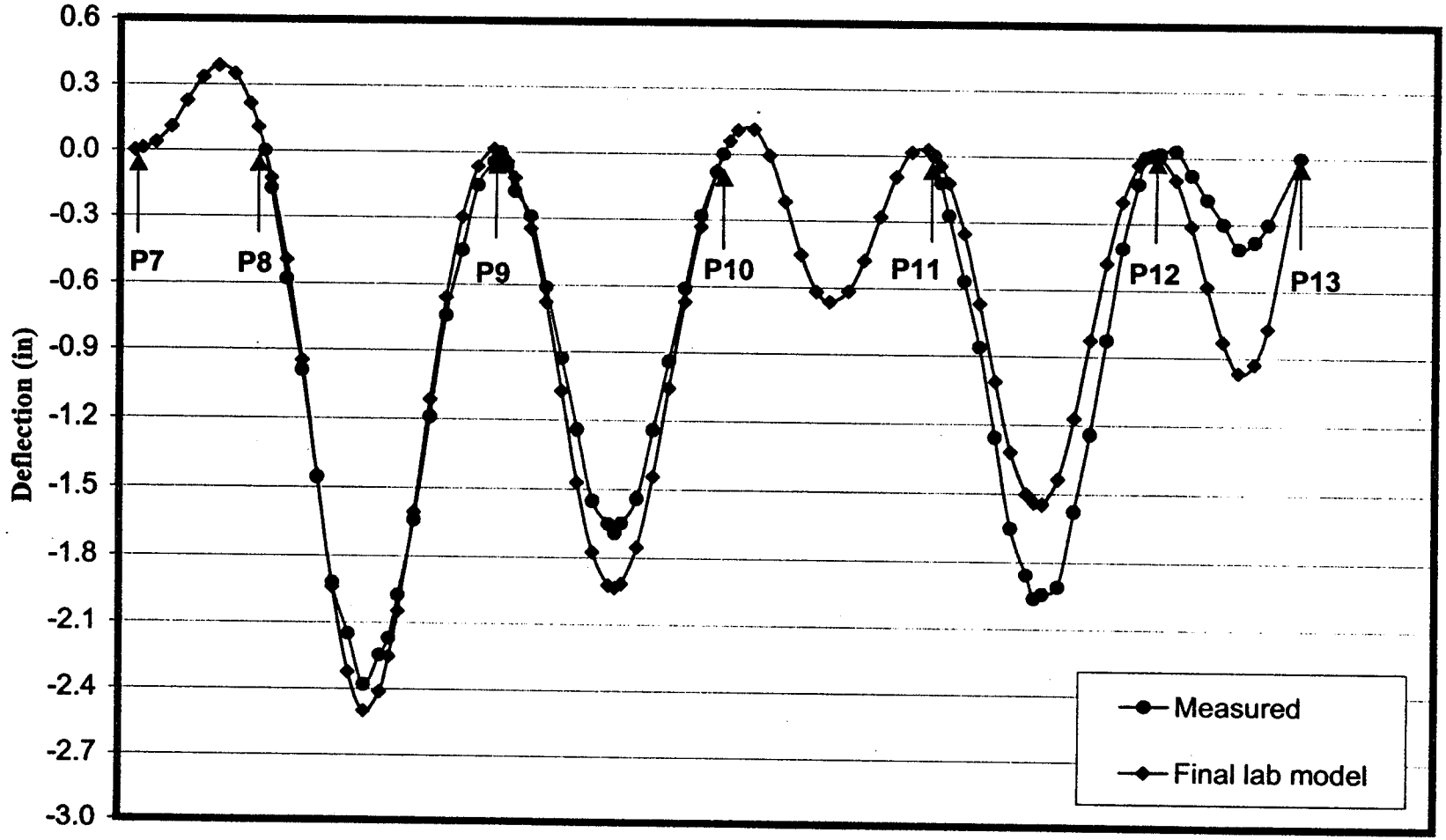

Figure 6.26: Deflection of final lab model (3/95-12/97)

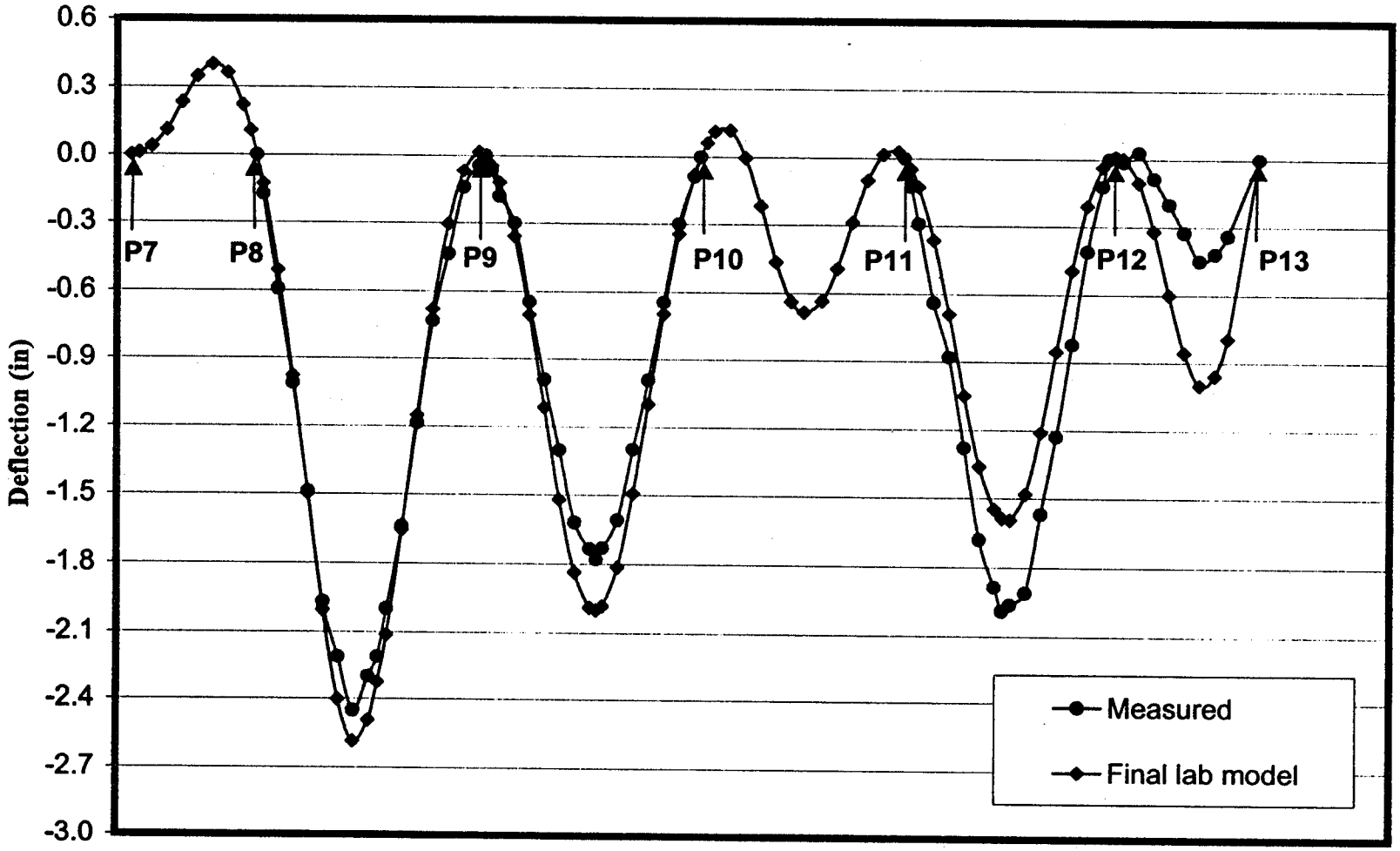

Figure 6.27: Deflection of final lab model (3/95-3/98)

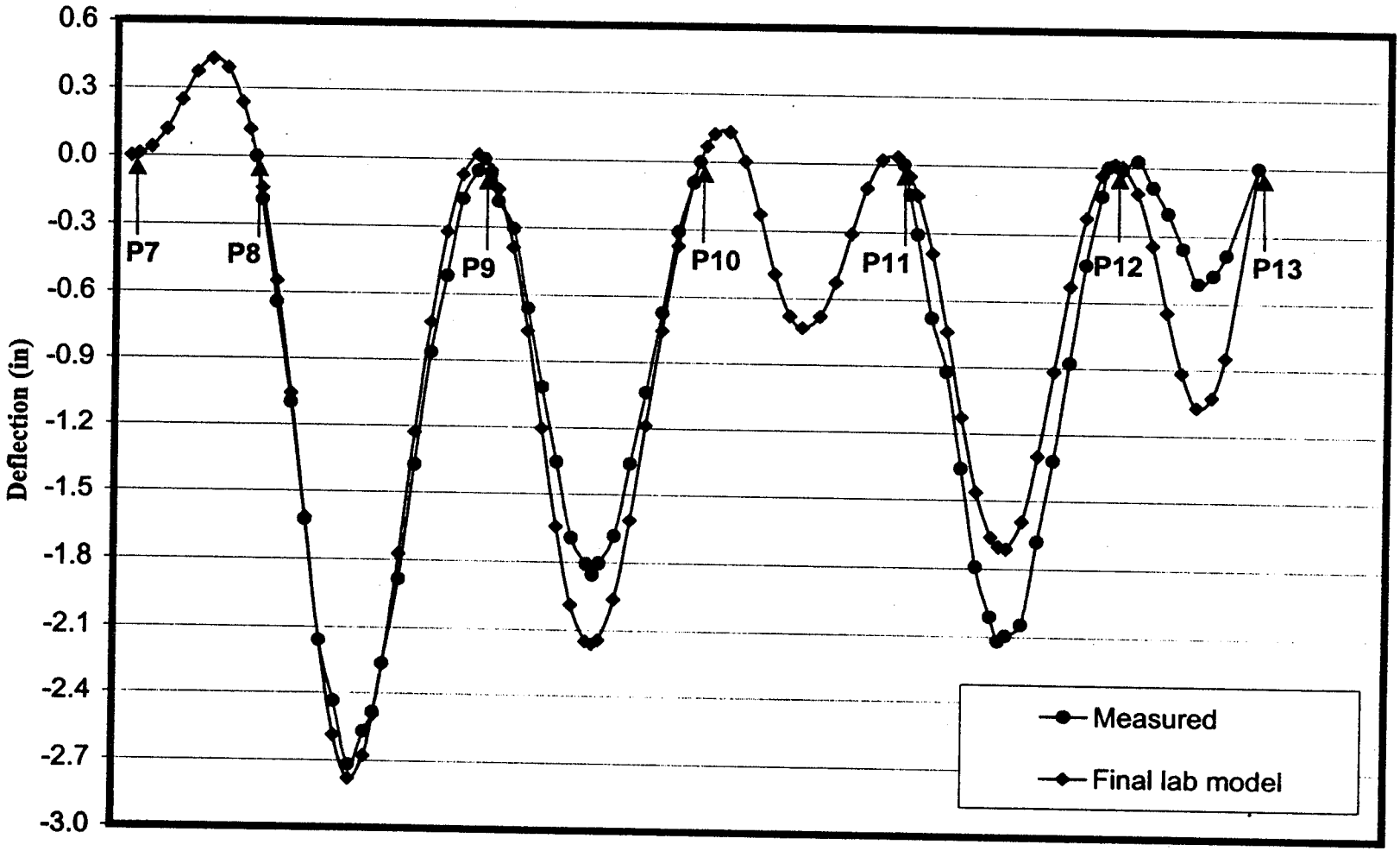

Figure 6.28: Deflection of final lab model (3/95-11/98)

6.4 Midspan deflection

Under the influence of time-dependent concrete creep and shrinkage, the bridge will continue to deform over time. The final lab model can be used to predict the maximum midspan deflection with time. Figures 6.29 through 6.32 illustrate the increase in deflection for midspan P8-9, P9-10, P11-12 and P12-13 for 40 years after the end of construction. The deflection continues to increase for a long period of time, but the rate of increase decreases with time. The measured midspan deflections for the first four years are shown for comparison.

6.5 Span shortening

The purpose of the extensometers was to measure axial shortening of the instrumented spans. Readings were recorded once a day at 6:00 AM. Axial shortening was determined by comparison of two measurements. First, a set of initial readings was recorded. Subsequent measurements were modified for thermal effects on the graphite rod. The span shortening for a given date was then calculated by subtracting the adjusted measurement on that day from the initial reading.

For any given time period, the SFRAME output file gives the X-direction position of each node. The relative X-position was then calculated by taking the difference between the two bearing nodes at the ends of each span. Therefore, the predicted axial shortening for a given date was determined by taking the difference between the initial and final relative X-displacements.

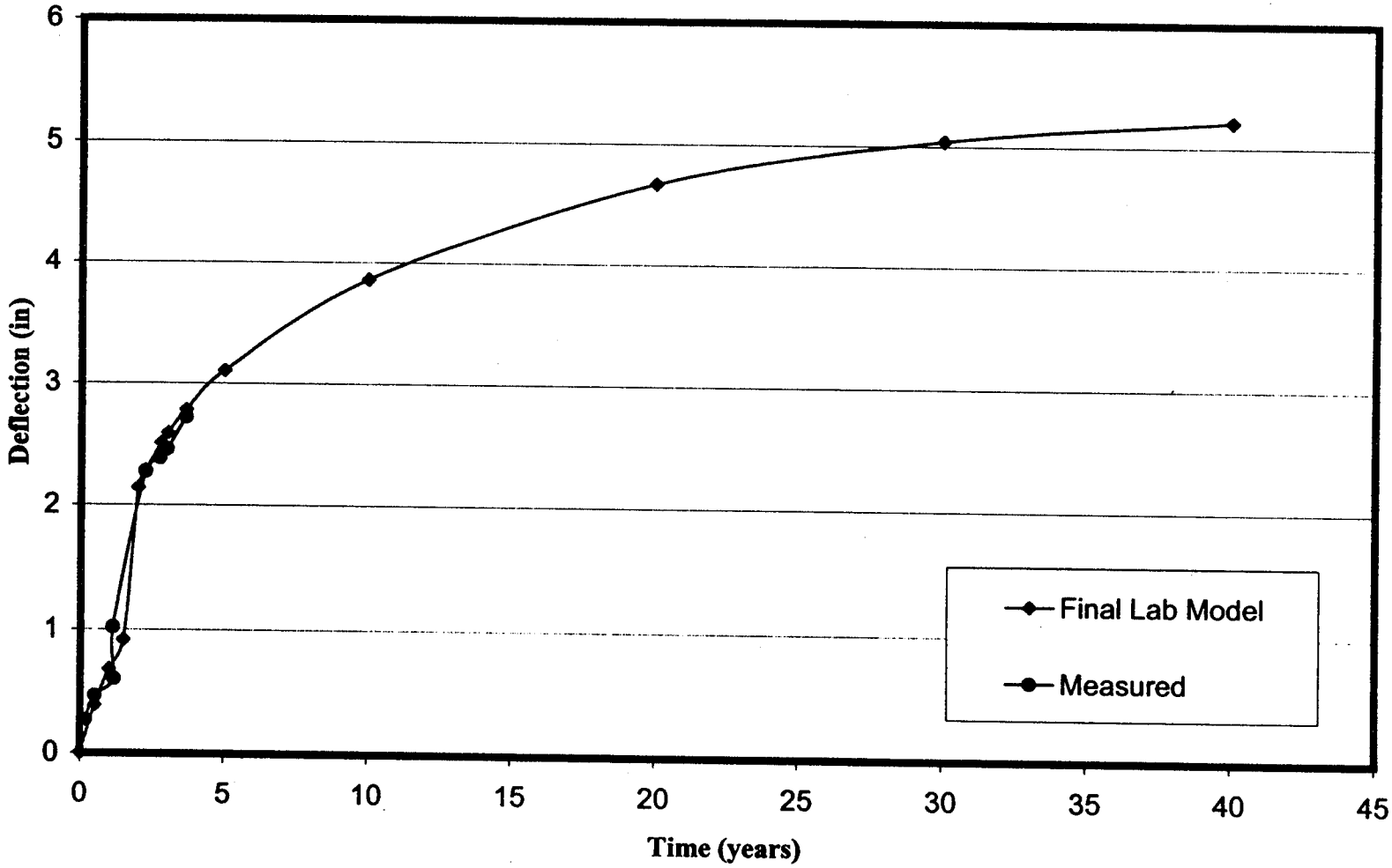

Figure 6.29: Midspan P8-9 deflection with time

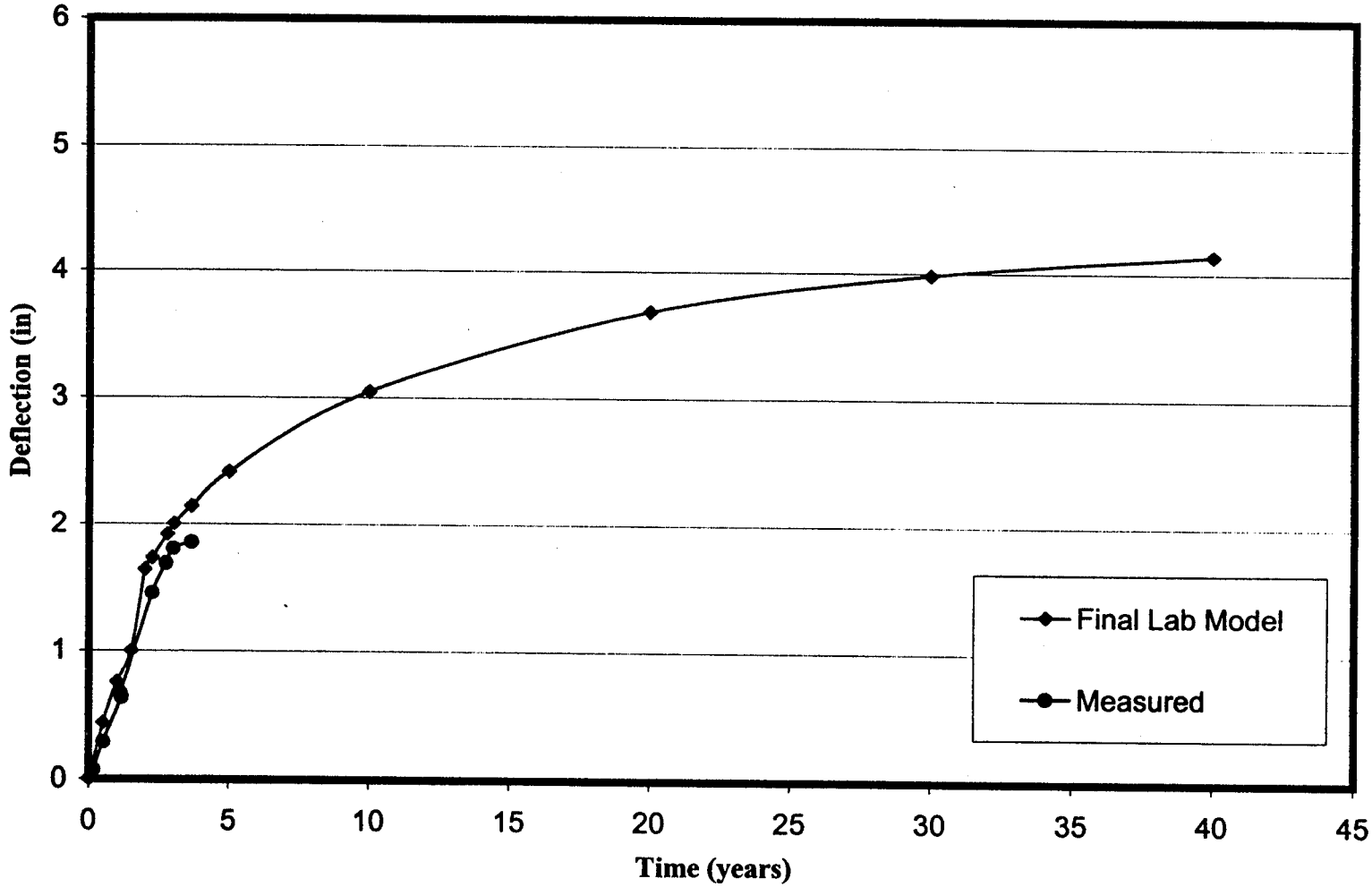

Figure 6.30: Midspan P9-10 deflection with time

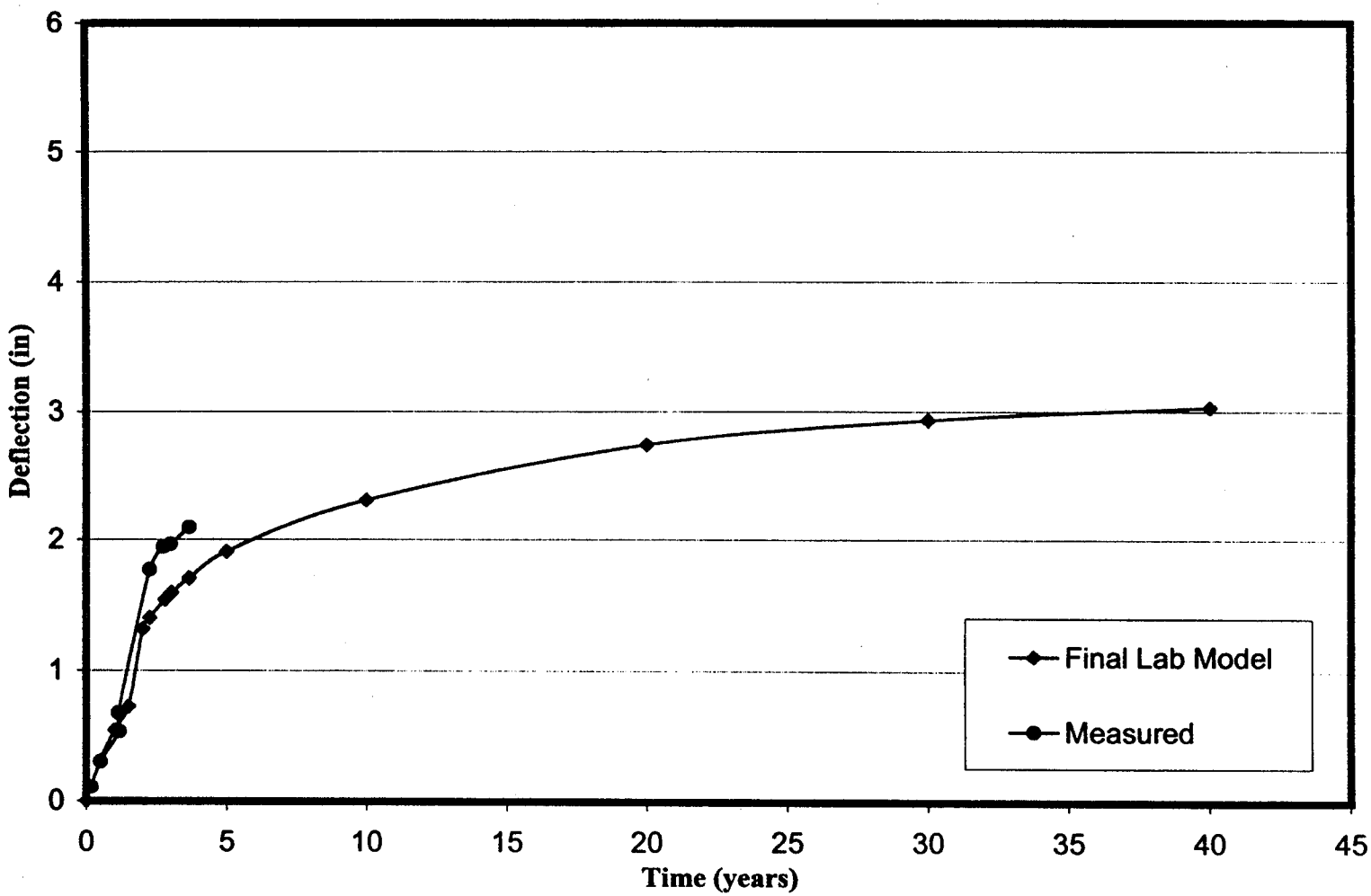

Figure 6.31: Midspan P11-12 deflection with time

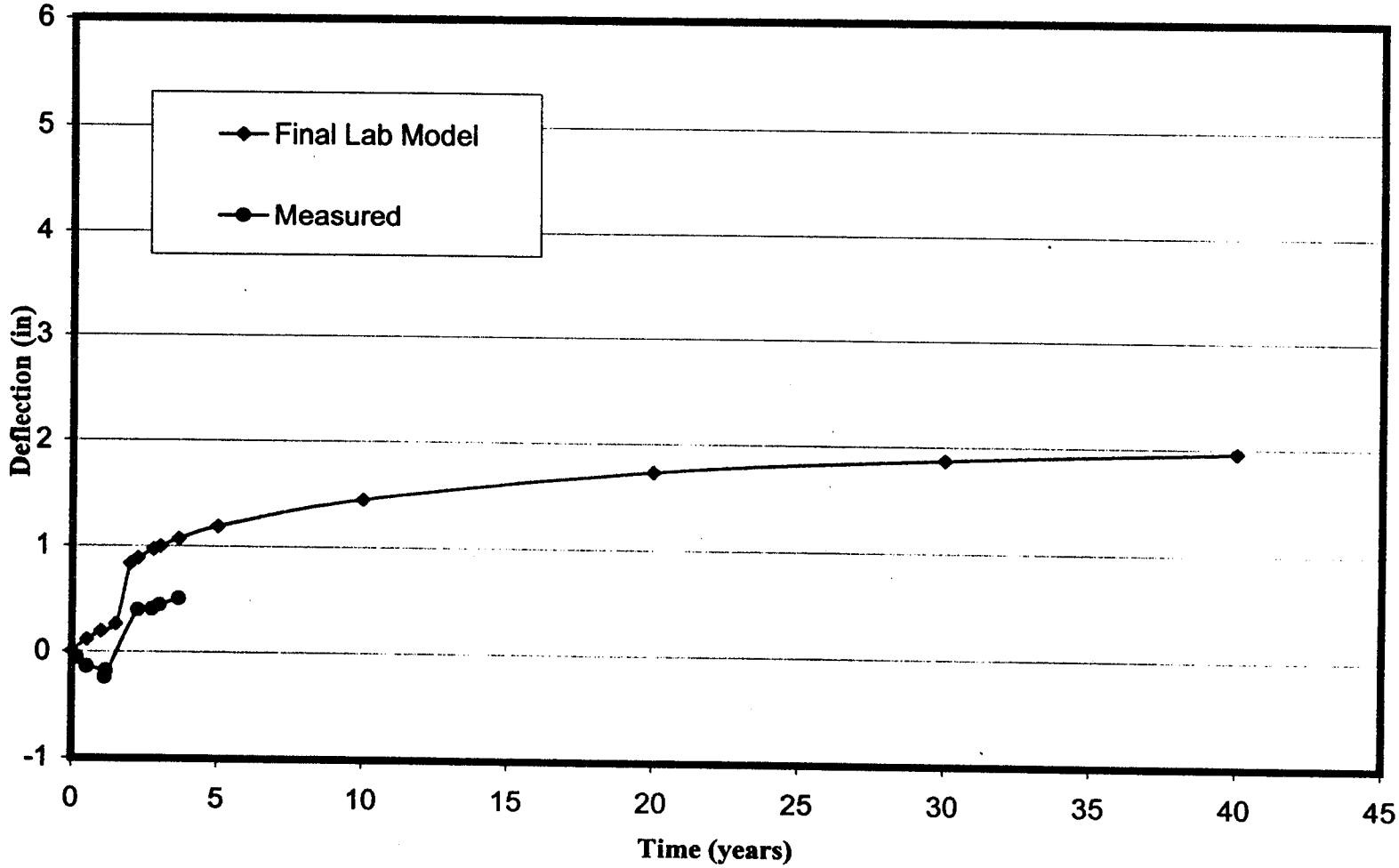

Figure 6.32: Midspan P12-13 deflection with time

Figures 6.33 to 6.36, show the axial shortening measurements for spans P8-9, P9-10, P11-12 and P12-13. It can be noted that the field measurements fluctuate on a daily and seasonal basis. The SFRAME predictions based on the T.Y. Lin As-built, initial lab and final lab models are also shown in Figures 6.33 to 6.36.

On the whole, the final lab model provides a very good prediction of the span shortening for all instrumented spans. Moreover, the final lab model predictions are generally an improvement over the initial lab model and the T.Y. Lin As-built model.

It is reassuring to note that the material parameters selected for SFRAME based on vertical deflection predictions have also produced the best estimate of span shortening.

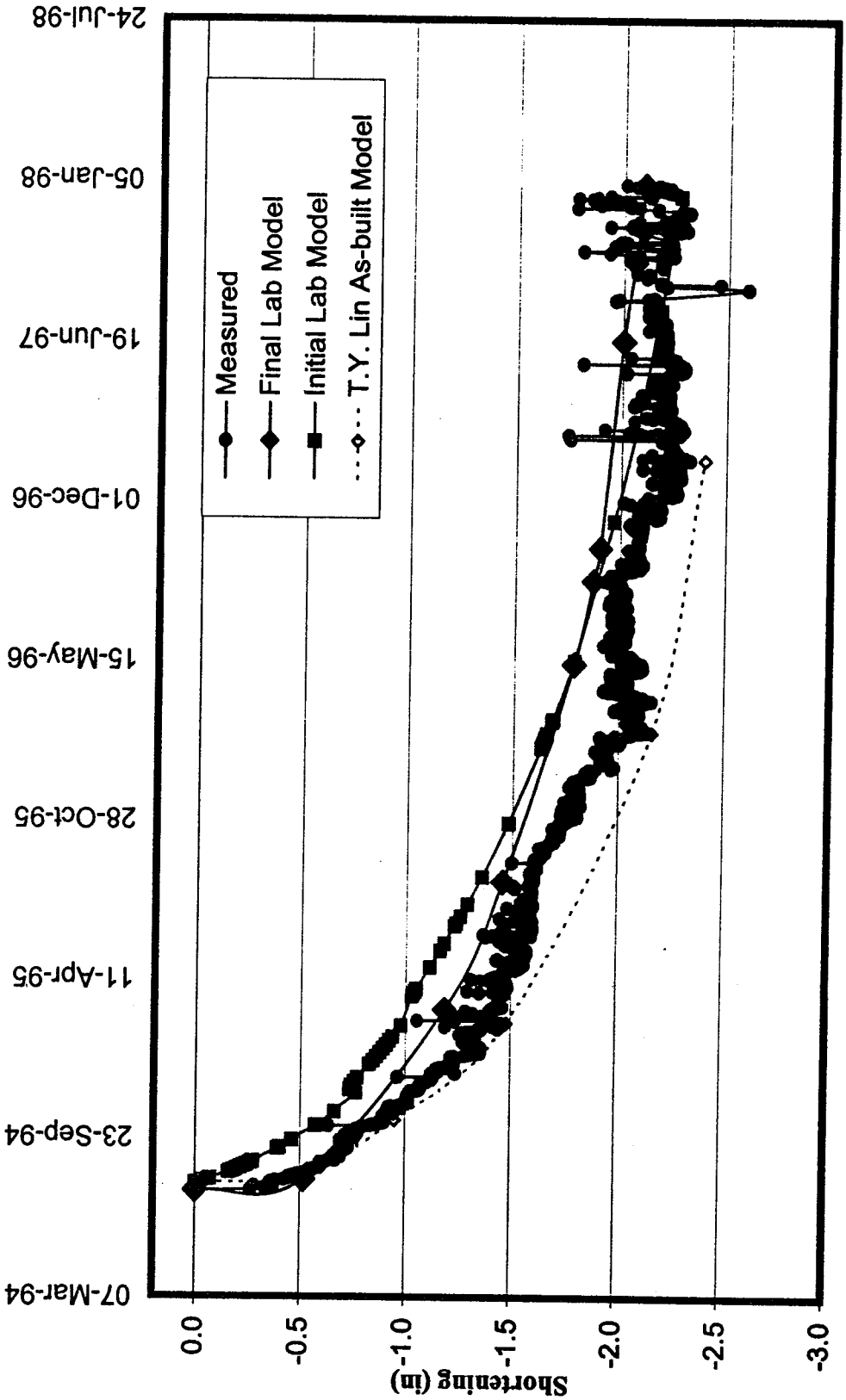

Figure 6.33: Span P8-9 Shortening

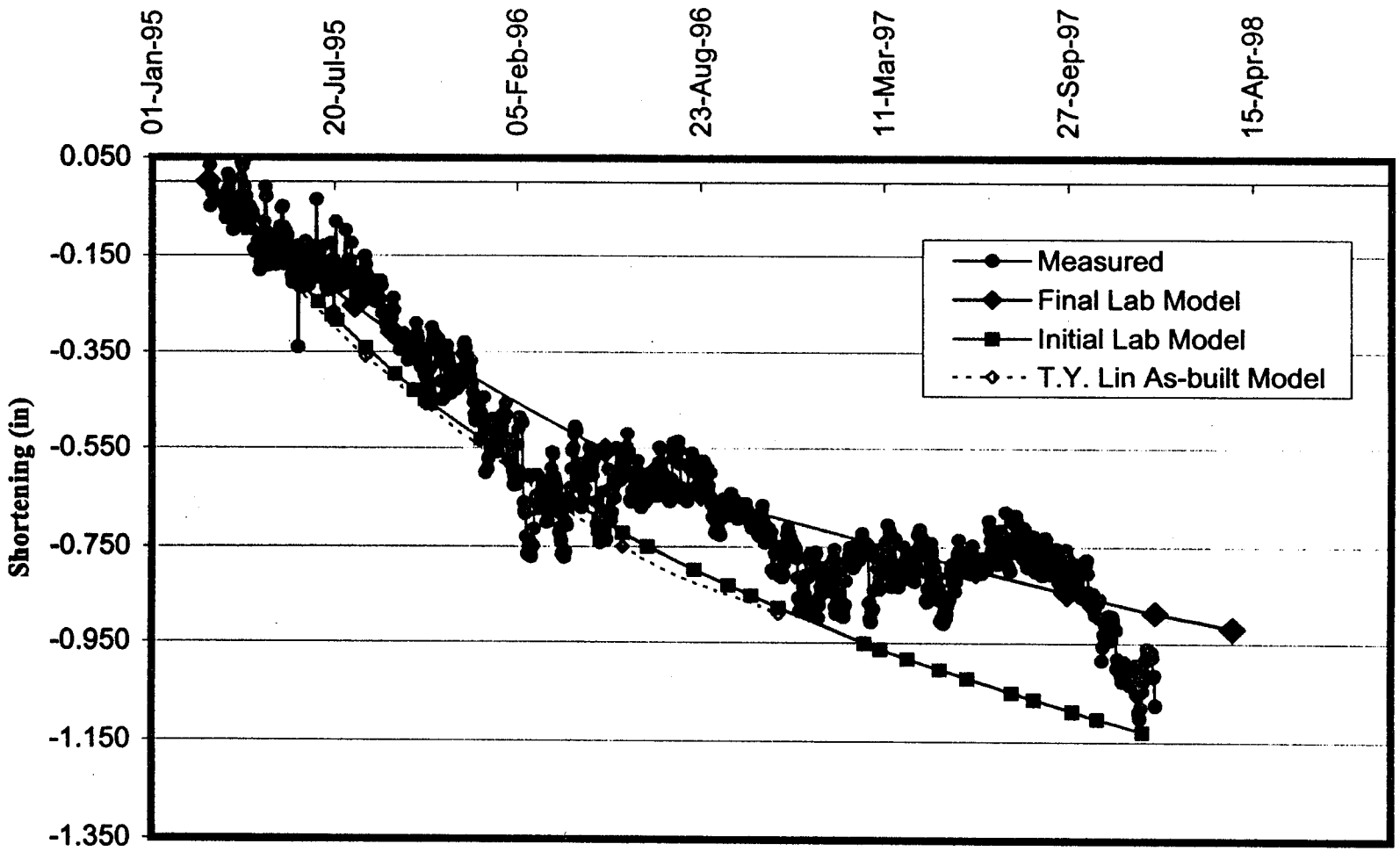

Figure 6.34: Span P9-10 shortening

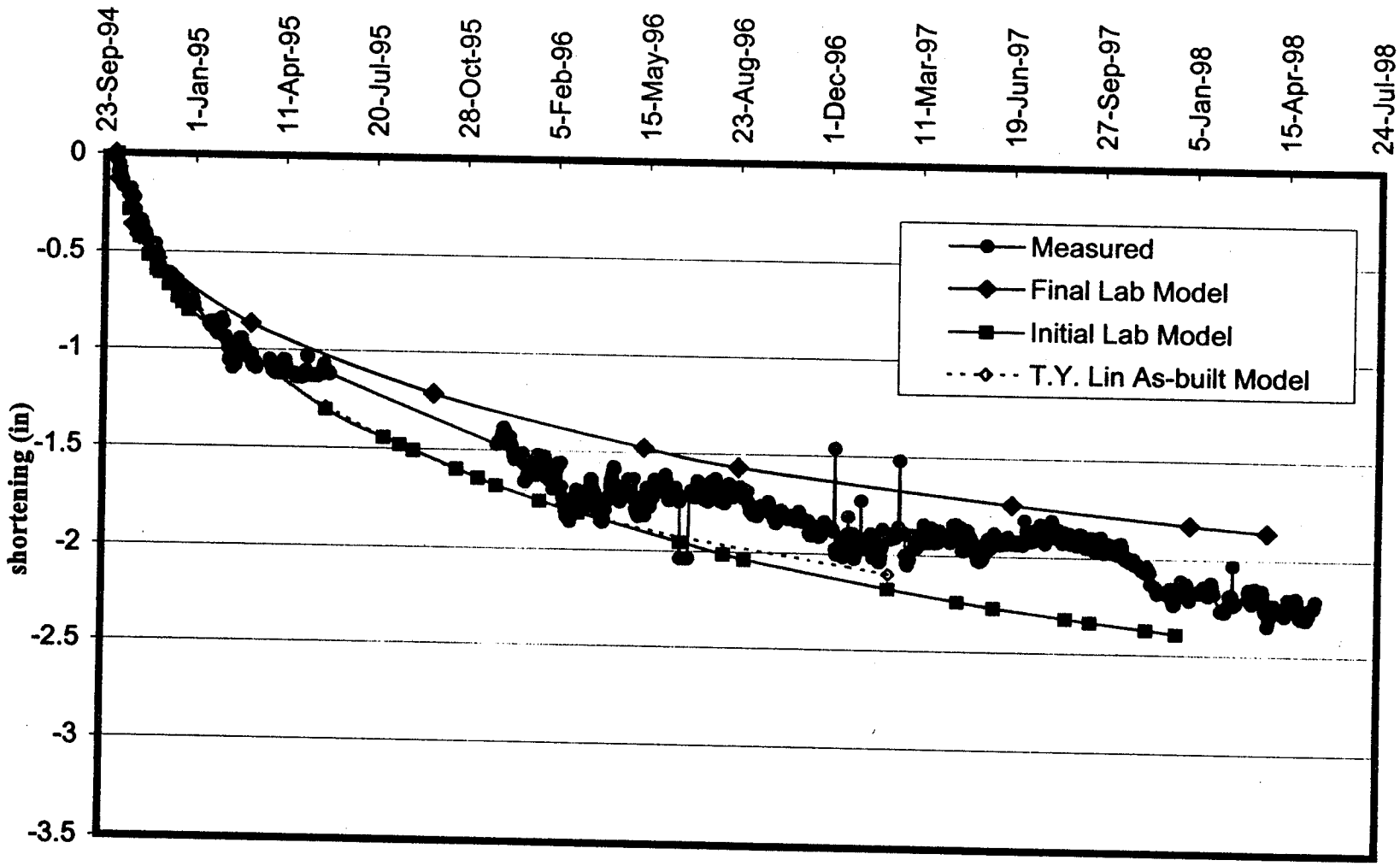

Figure 6.35: Span P11-12 Shortening

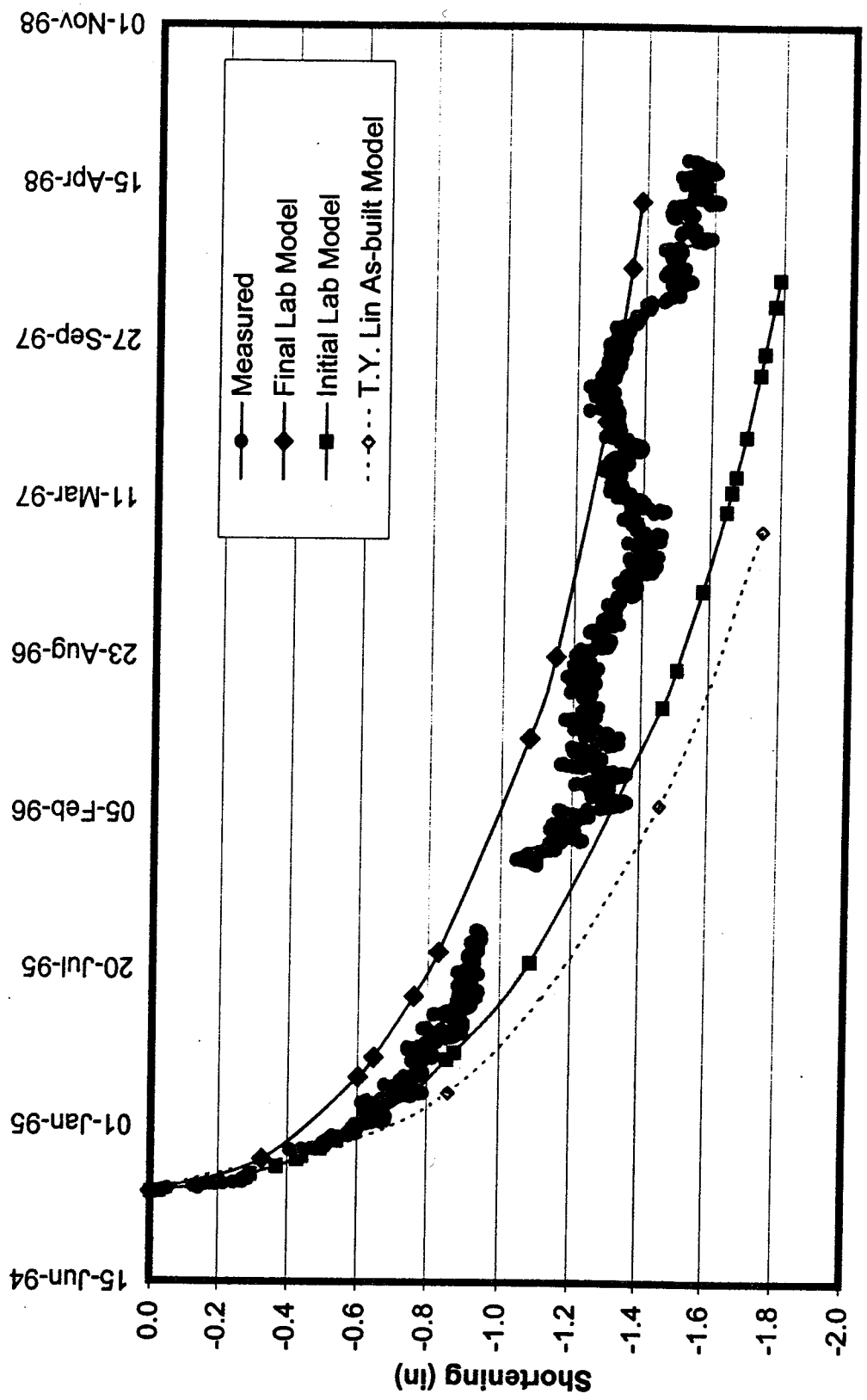

Figure 6.36: Span P12-13 shortening

CHAPTER 7

DEVELOPMENT OF DEFLECTION ENVELOPE

7.1 Introduction

Chapter 6 presented the results of various SFRAME models compared with the measured viaduct deflections. Neither the T.Y. Lin As-built model or the initial laboratory model was able to predict the long-term structural response for all spans of the viaduct. Inclusion of creep and shrinkage predictions based on short-term laboratory tests improved the predictions for the initial laboratory model, but the results are still inadequate as predictors of the structural response.

It is therefore necessary for the designer to estimate likely ranges for each of the critical parameters and develop upper and lower deflection envelopes which can be anticipated to encompass any potential structural response. This chapter presents the development of such envelopes for the NHVV.

7.2 Parameter ranges

Ranges for all critical parameters are chosen to reflect the anticipated variability of the parameter under field construction conditions.

7.2.1 Relative humidity

The daily average relative humidity measured in the field varied from about 80% to 90% (Figure 6.3). Hence, the upper and lower limits of the relative humidity are taken to be 90% and 80% respectively. The creep and shrinkage components of the concrete constitutive model were modified accordingly. The resulting range of creep and shrinkage values are shown in Figures 7.1 to 7.4.

7.2.2 Self-weight of the concrete

As discussed in Section 6.2.4.3, self-weight components not included in the cross-section used in the SFRAME model must be included by increasing the apparent concrete density. A value of 165 pcf represented the high end of the range and 145 pcf was used for the low end value.

7.2.3 Creep and shrinkage

Creep and shrinkage of concrete are known to have variability of ± 30% (Gilbert, 1988). The concrete creep and shrinkage measured under constant temperature and humidity conditions in the laboratory show variations of ± 25% (Durbin and Robertson, 1998). In addition, the mathematical models used to predict the long-term values based on short-term creep and shrinkage tests are not able to extrapolate the response perfectly. Adjusting the model predictions for field atmospheric conditions and V/S ratio will also be imperfect. Therefore, it is likely that creep and shrinkage predictions could vary by

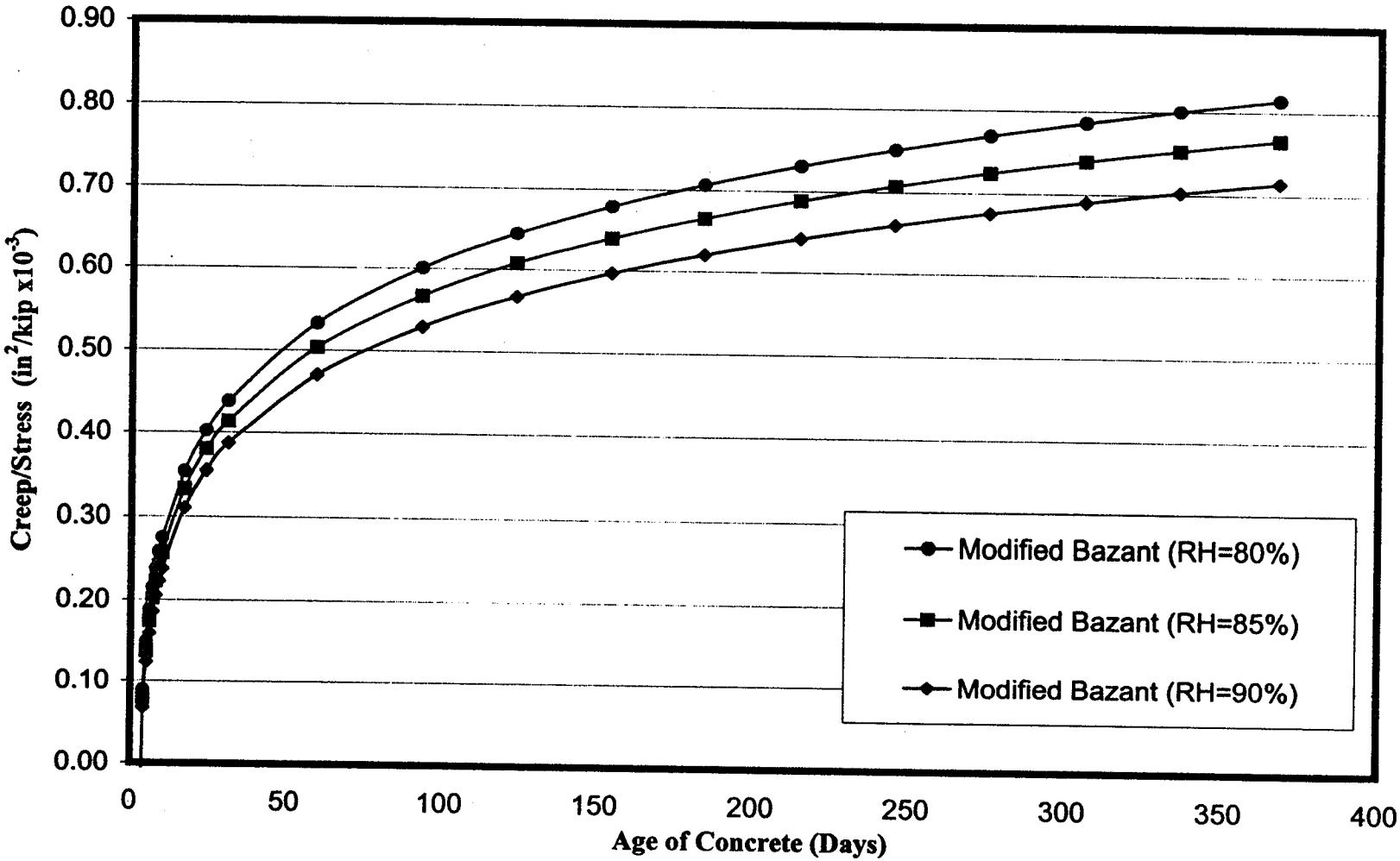

Figure 7.1: Modified Bazant 3-day creep prediction for varying relative humidity

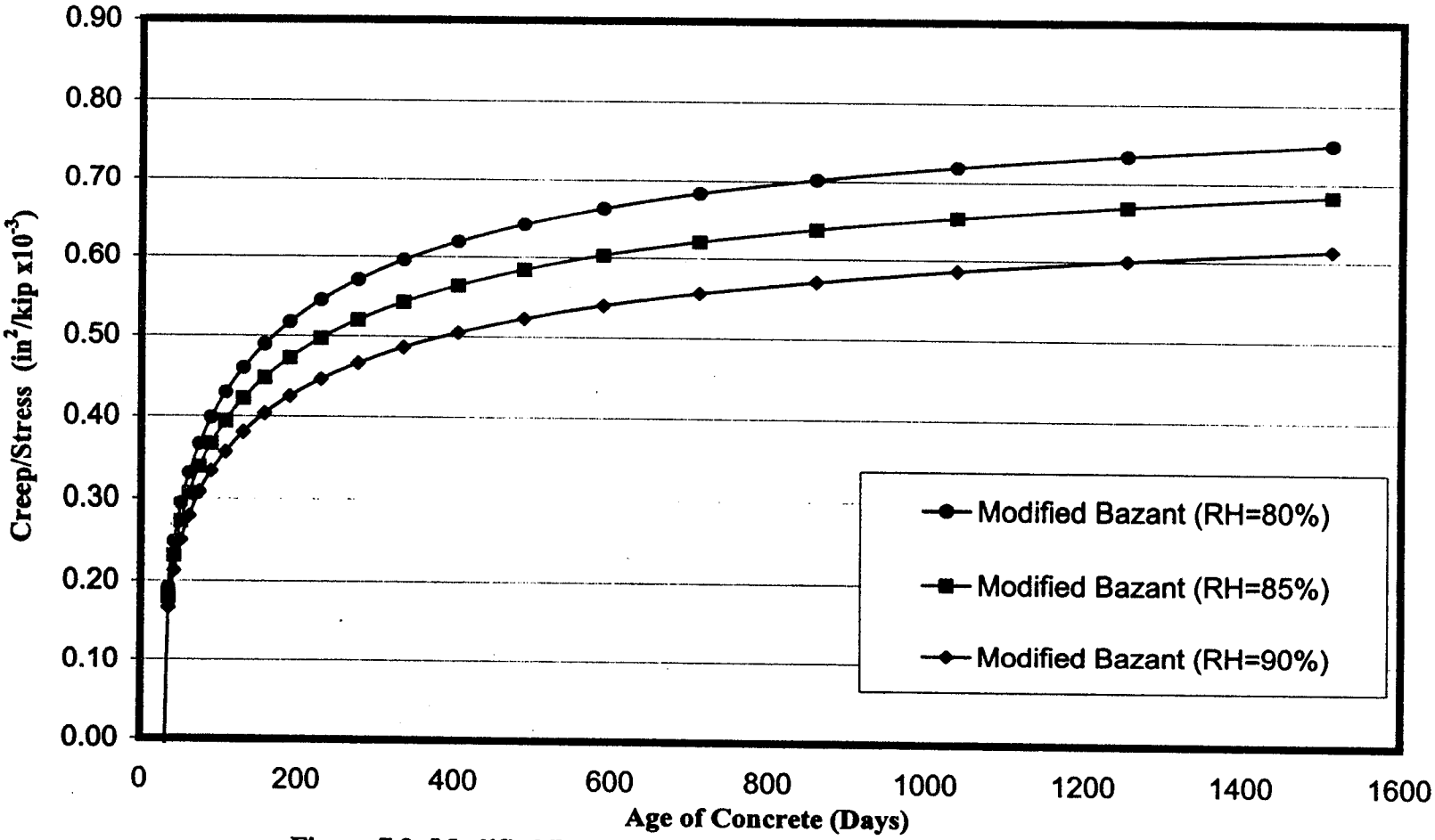

Figure 7.2: Modified Bazant 28-day creep prediction for varying relative humidity

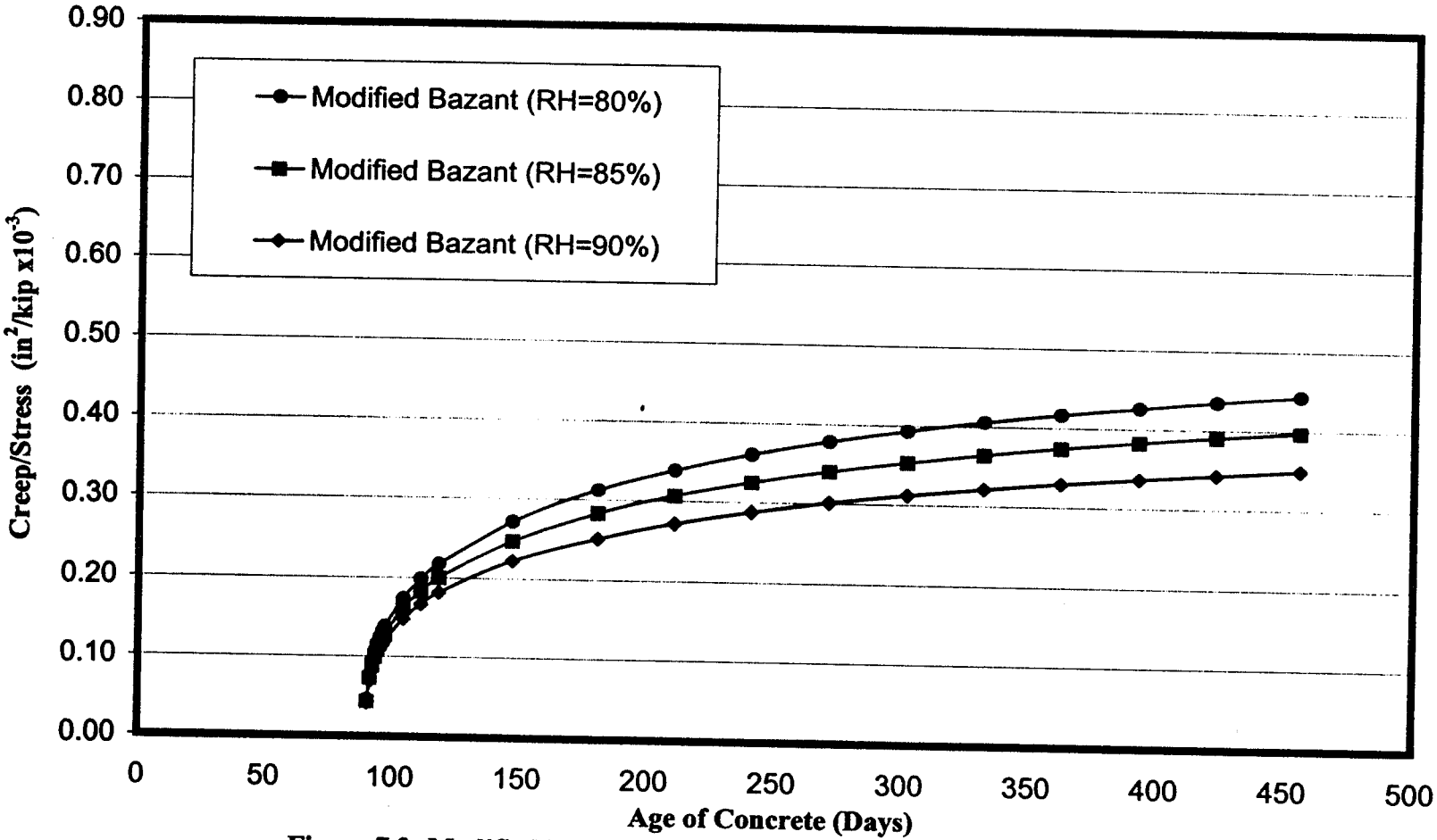

Figure 7.3: Modified Bazant 90-day creep prediction for varying relative humidity

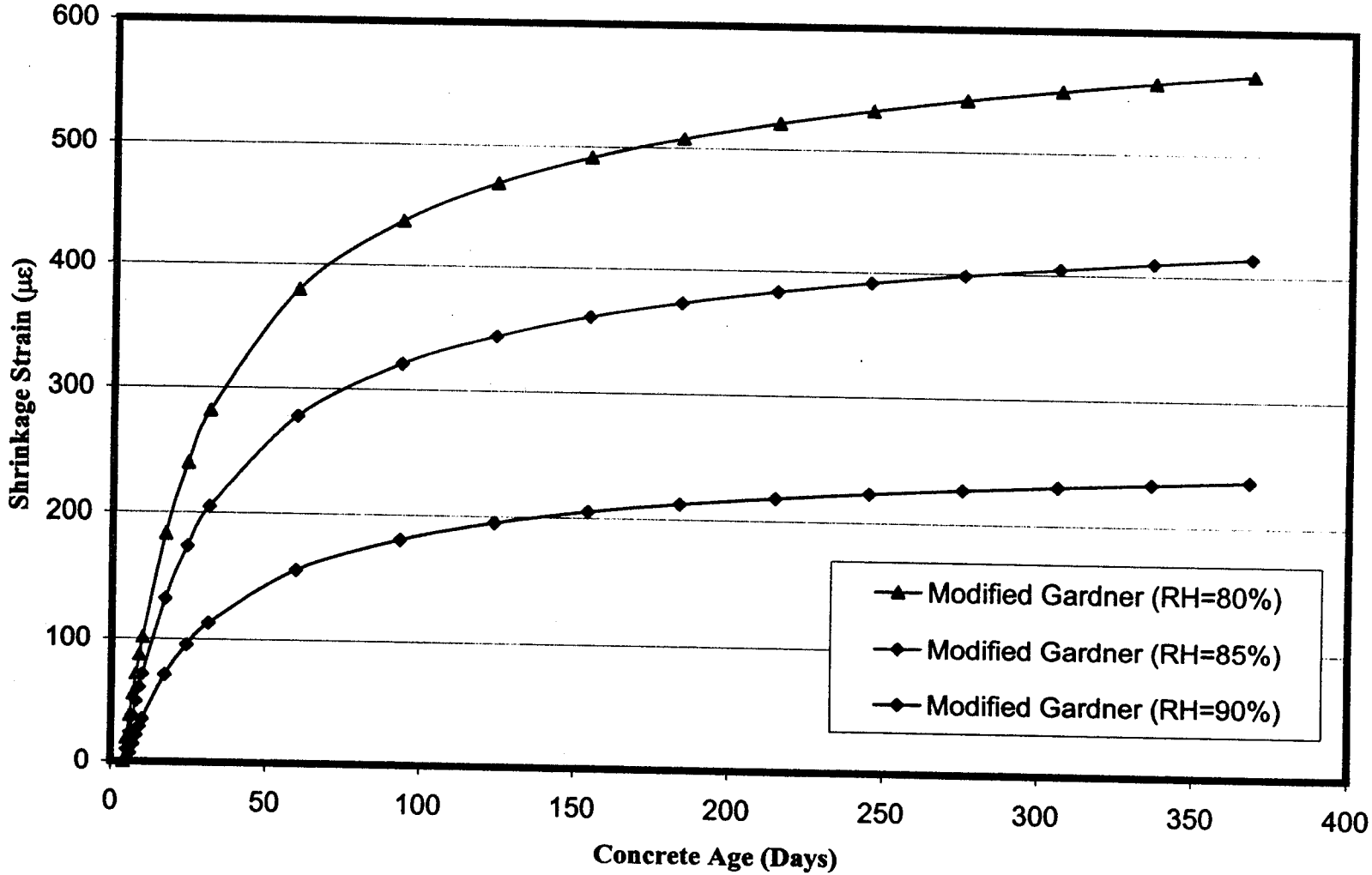

Figure 7.4: Modified Gardner 3-day shrinkage prediction for varying ralative humidity

± 30%. The upper and lower ranges for creep and shrinkage scaling factors are therefore taken as 1.3 and 0.7 respectively.

7.2.4 Prestressing force

As observed in the span tendon stressing, prestressing forces in tendons may be less than the design values. Based on the load cell measurements discussed in Section 6.2.4.9, 85% of the design prestressing force is a reasonable lower bound. Since both prestress force and extension measurements are used to prevent overstressing, it is unlikely that prestress forces will exceed the design values by more than about 5%. Hence 105% is used as the upper bound.

7.3 Deflection envelope

With the above parameter ranges, different parameter range combinations were applied in SFRAME in order to determine the extreme upper and lower limits of the deflection. Various combinations were considered until the absolute maximum and minimum deflections were found for each span.

The parameters providing the lower bound (maximum) deflections for all spans except span P8-9 are:

relative humidity 80%,

concrete self-weight of 165 pcf,

creep scaling factor 1.3,

shrinkage scaling factor 1.3,

prestressing force scaling factor 0.85.

For span P8-9, the same parameters were used except with a shrinkage scaling factor of 0.7.

The upper bound (minimum) deflections for all but span P8-9 were obtained using the following:

relative humidity 90%,

concrete self-weight of 145 pcf,

creep scaling factor 0.7,

shrinkage scaling factor 0.7,

prestressing force scaling factor 1.05.

For span P8-9, the upper bound (minimum) deflection was obtained with the same parameters except with a shrinkage scaling factor of 1.3.

Figure 7.5 displays the resulting span deflection envelopes for the period from March 1995 to June 1997. The corresponding field measurements are also plotted.

On the whole, the observed deflections are all within the deflection envelopes. It can be noted that the observed deflections for spans P8-9 and P11-12 approach the analytical lower limit of deflection, while the deflections in span P9-10 are approximately midway between upper and lower limits. The observed deflection of span P12-13 tends toward the

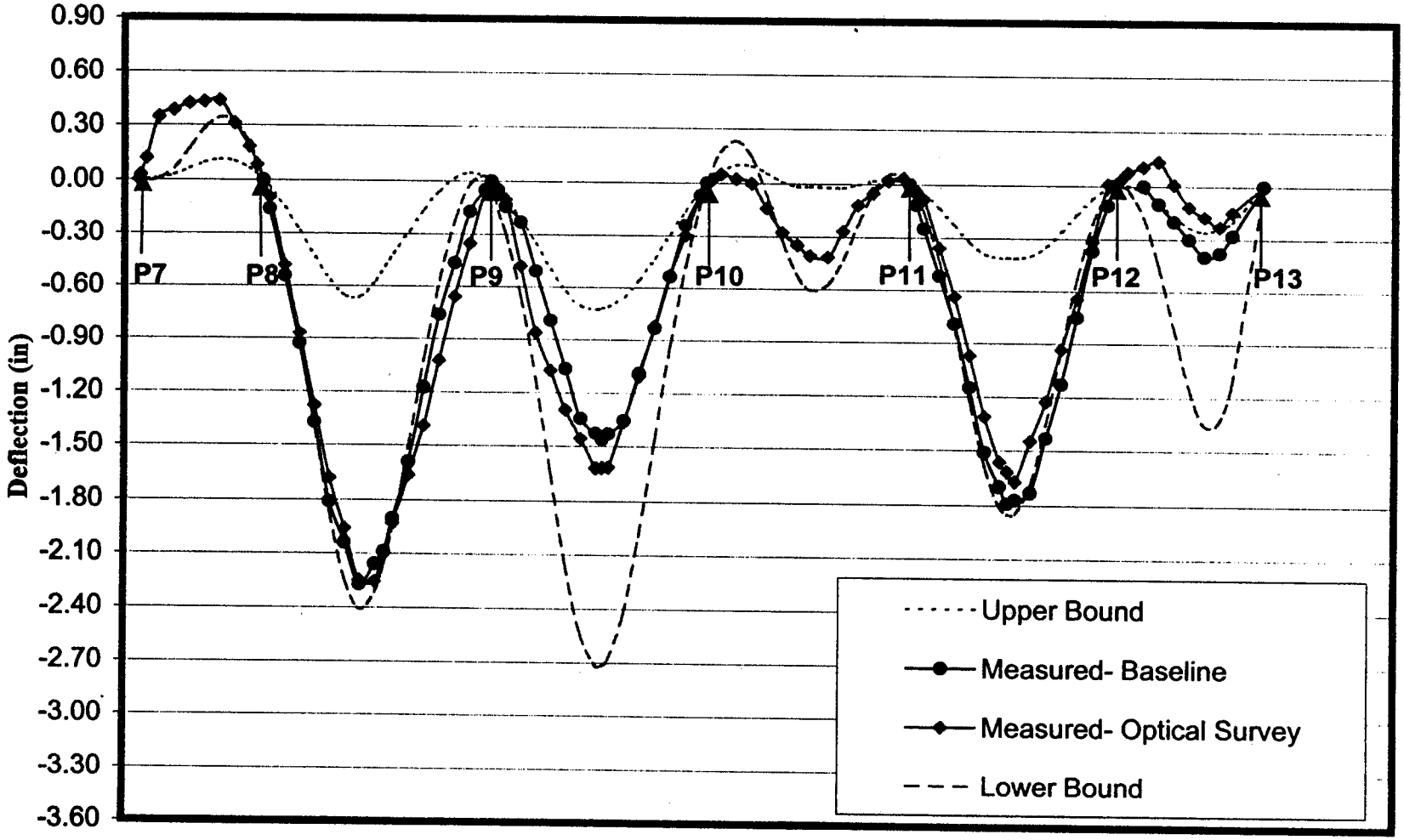

Figure 7.5: Long term deflection envelope (3/95-6/97)

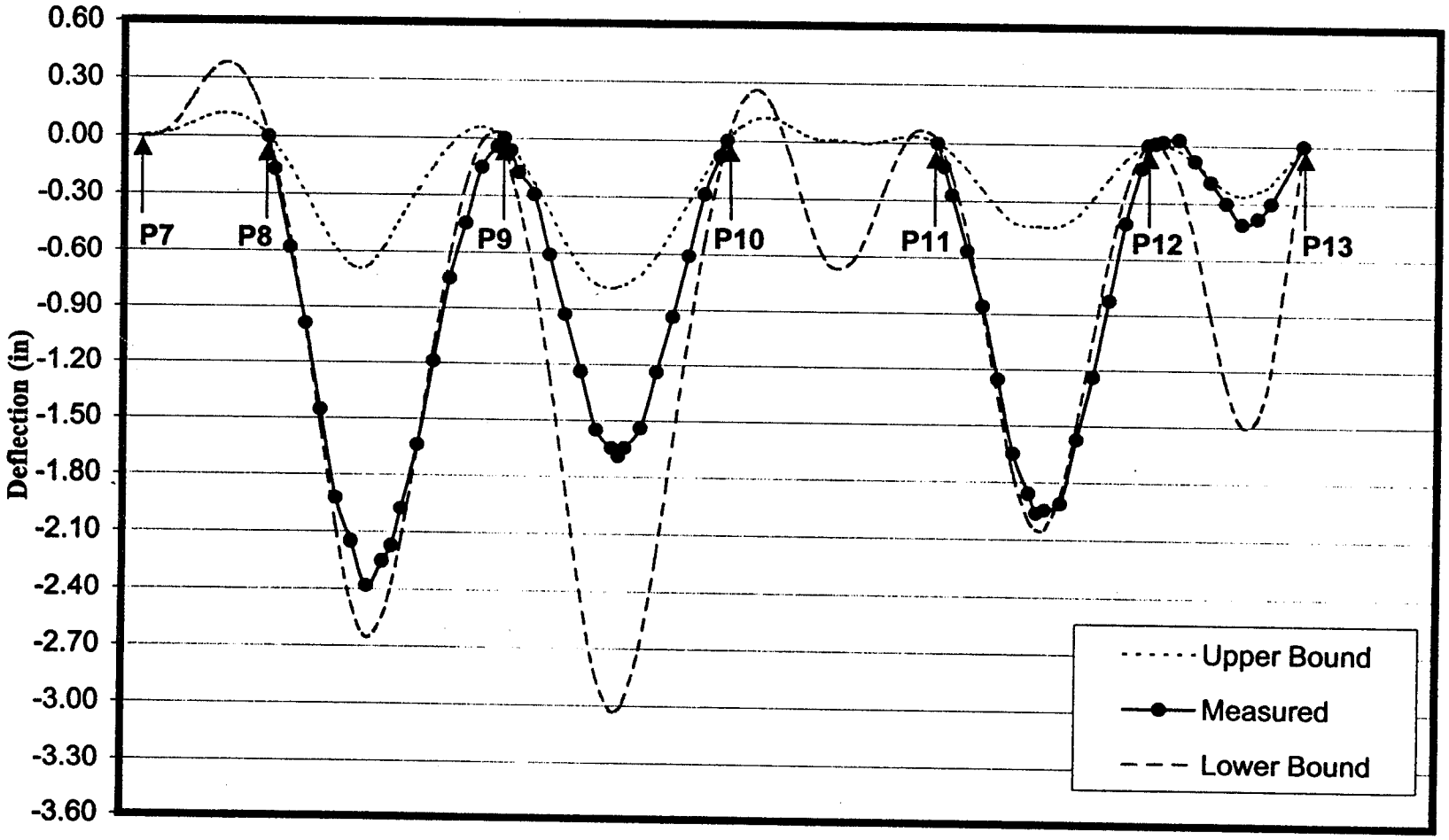

Figure 7.6: Long term deflection envelope (3/95-12/97)

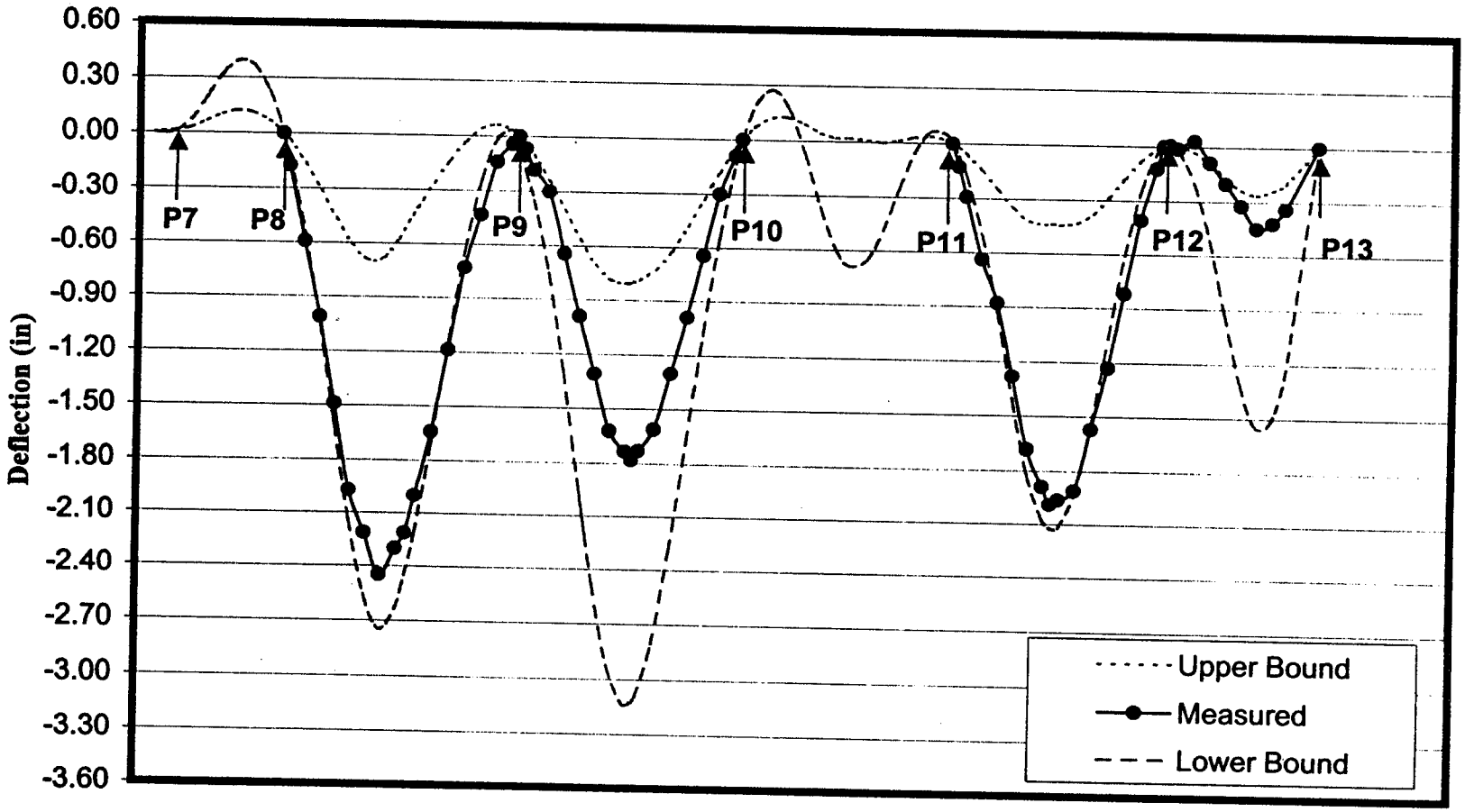

Figure 7.7: Long term deflection envelope (3/95-3/98)

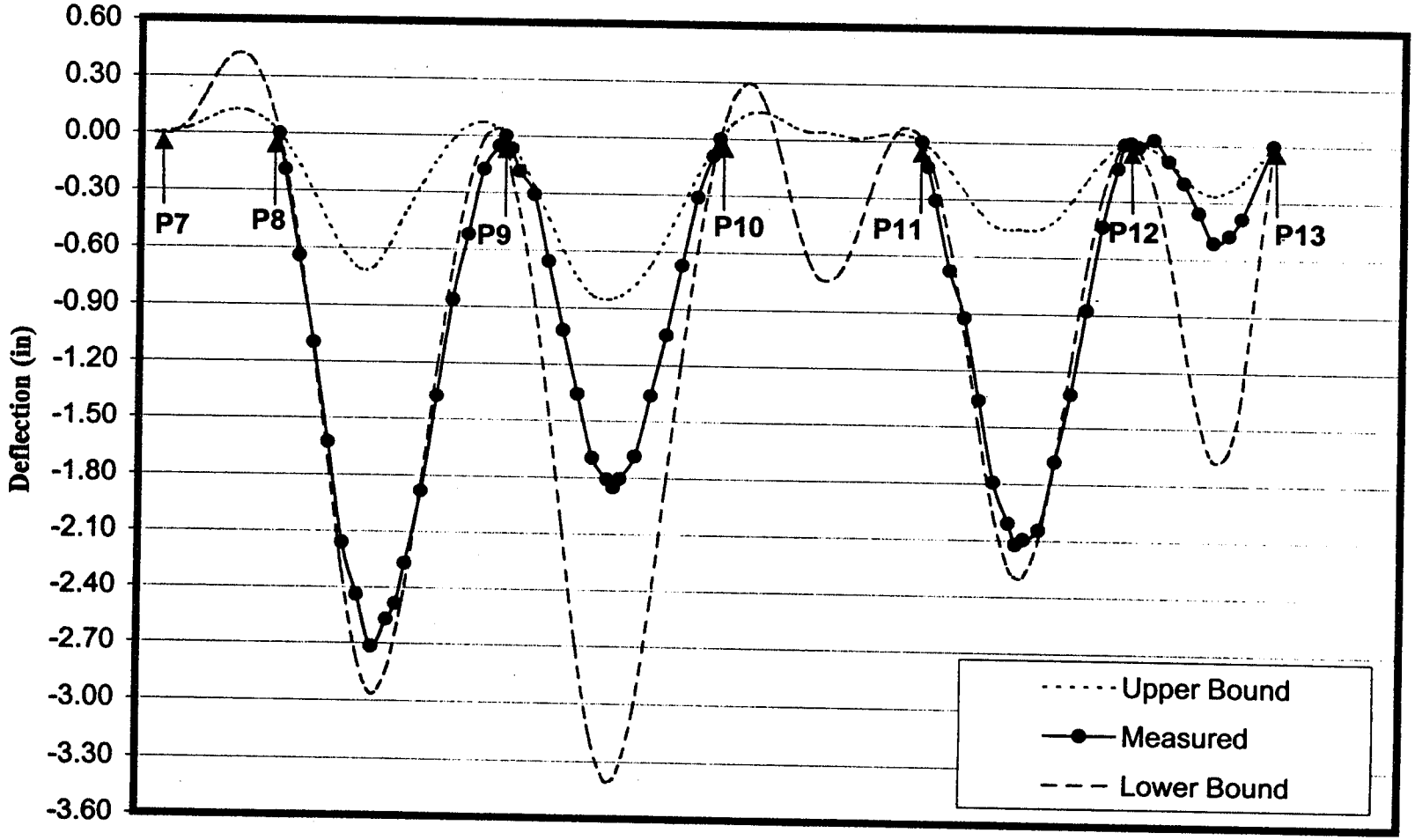

Figure 7.8: Long term deflection envelope (3/95-11/98)

upper deflection bound. Even though the parameter ranges considered here are all reasonable, it can be seen that their different combinations produce widely varying deflection bounds. In some spans the actual deflection approaches the maximum value, while elsewhere it approaches the minimum value. This illustrates why it is not easy to predict the deflection accurately using a single set of parameters for the entire structure.

The deflection envelopes for various other time periods after the end of construction, with the corresponding site measurements, are plotted in Figures 7.6 through 7.8. These plots also show that the measured deflections fall between the theoretical lower and upper limits.

7.4 Future deflection prediction

Having developed a final lab model and upper and lower deflection envelopes, it is now possible to predict the viaduct deflection in the future with some accuracy.

Figures 7.9 to 7.13, show the span deflection envelopes for 5-years, 10-years, 20-years, 30-years, and 40-years after completion of construction. The deflections predicted by the initial and final lab models are also plotted.

The final lab model has been calibrated to fit the deflected shape after two years (March 95 to June 97). It will therefore provide the best estimate of future deflected shapes. The maximum deflection after 40 years is expected to be 5.25 inch at midspan of P8-9 (Figure

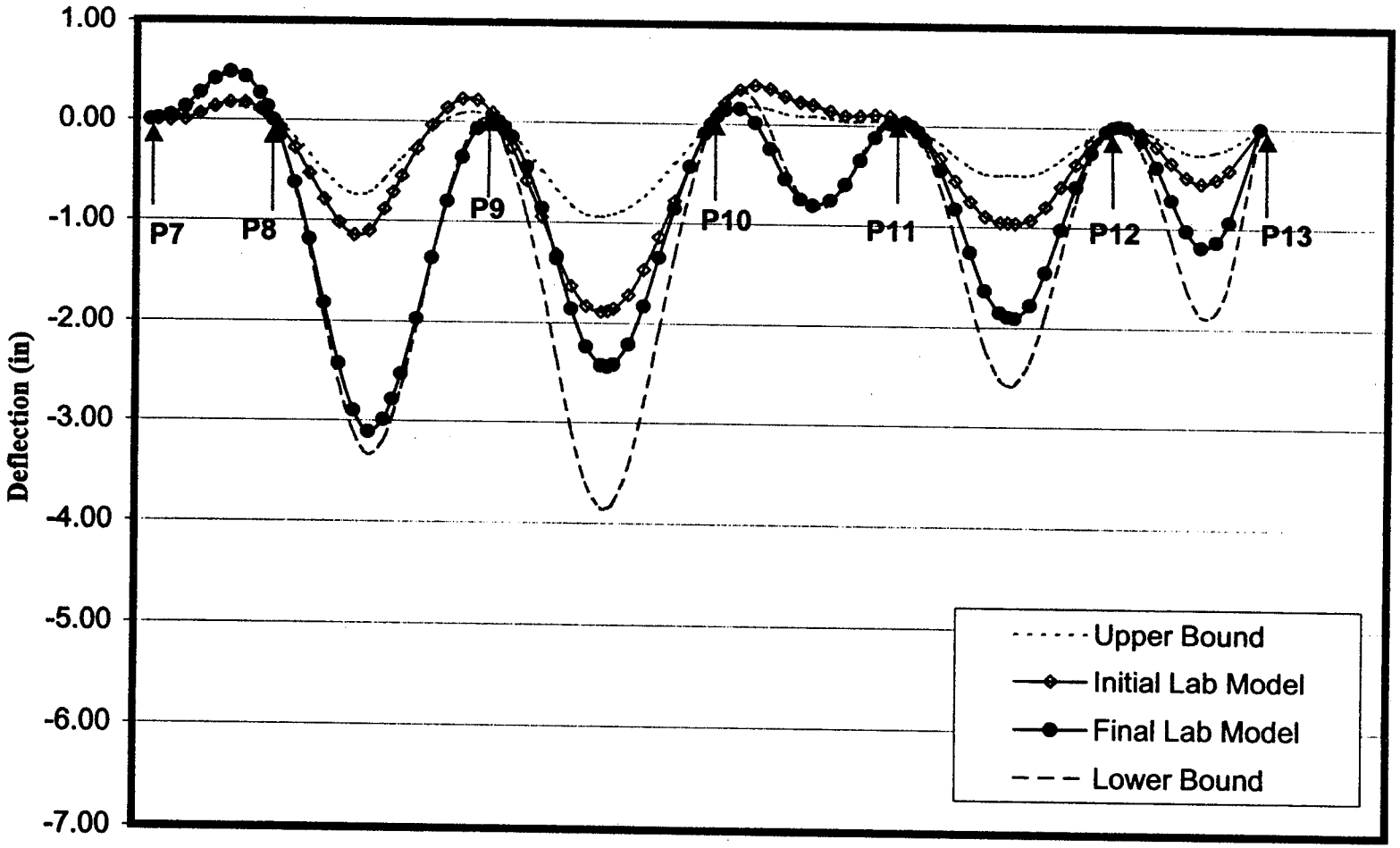

Figure 7.9: Long term deflection envelope (5 year; 3/95-3/2000)

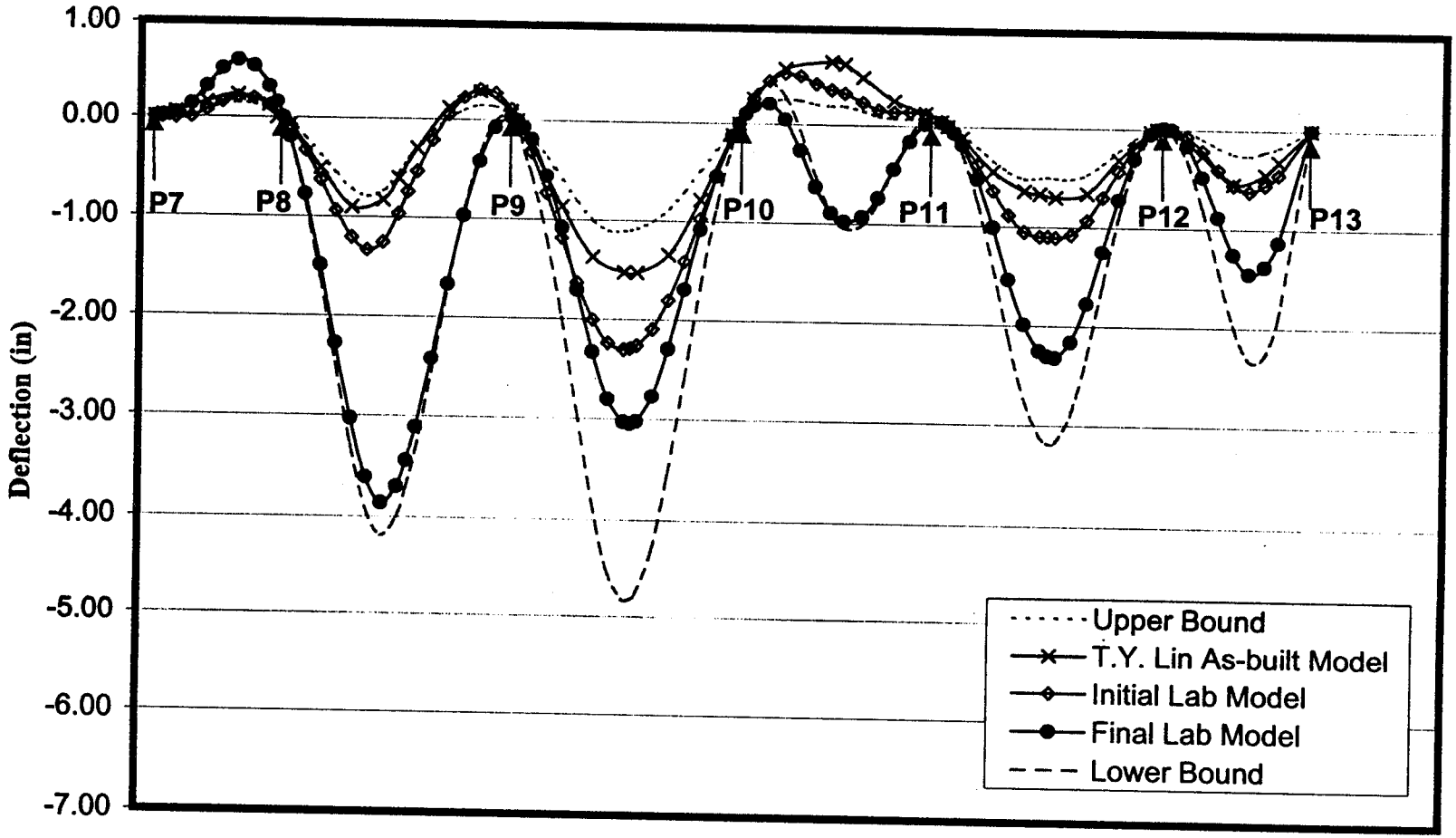

Figure 7.10: Long term deflection envelope (10 year; 3/95-3/2005)

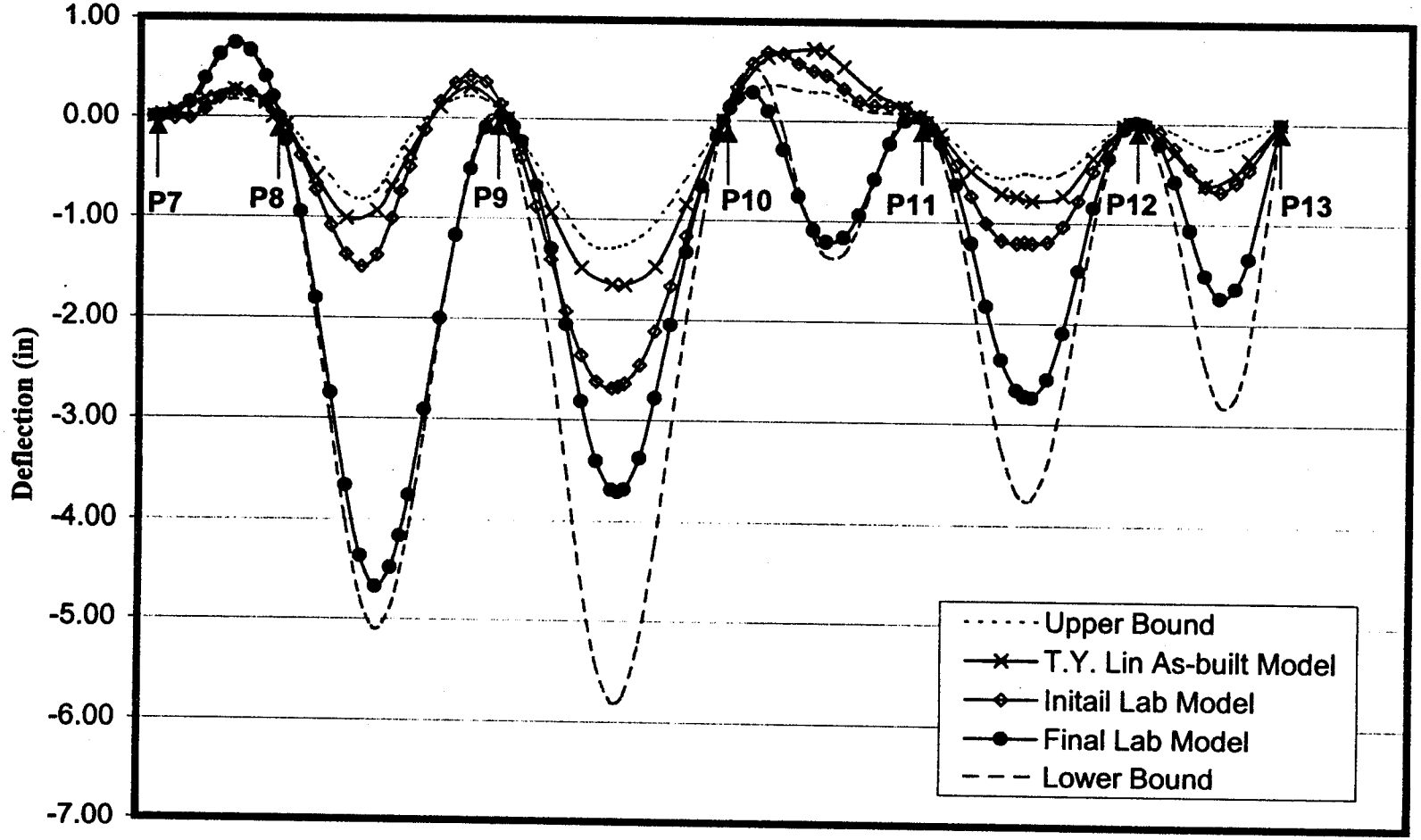

Figure 7.11: Long term deflection envelope (20 years; 3/95-3/2015)

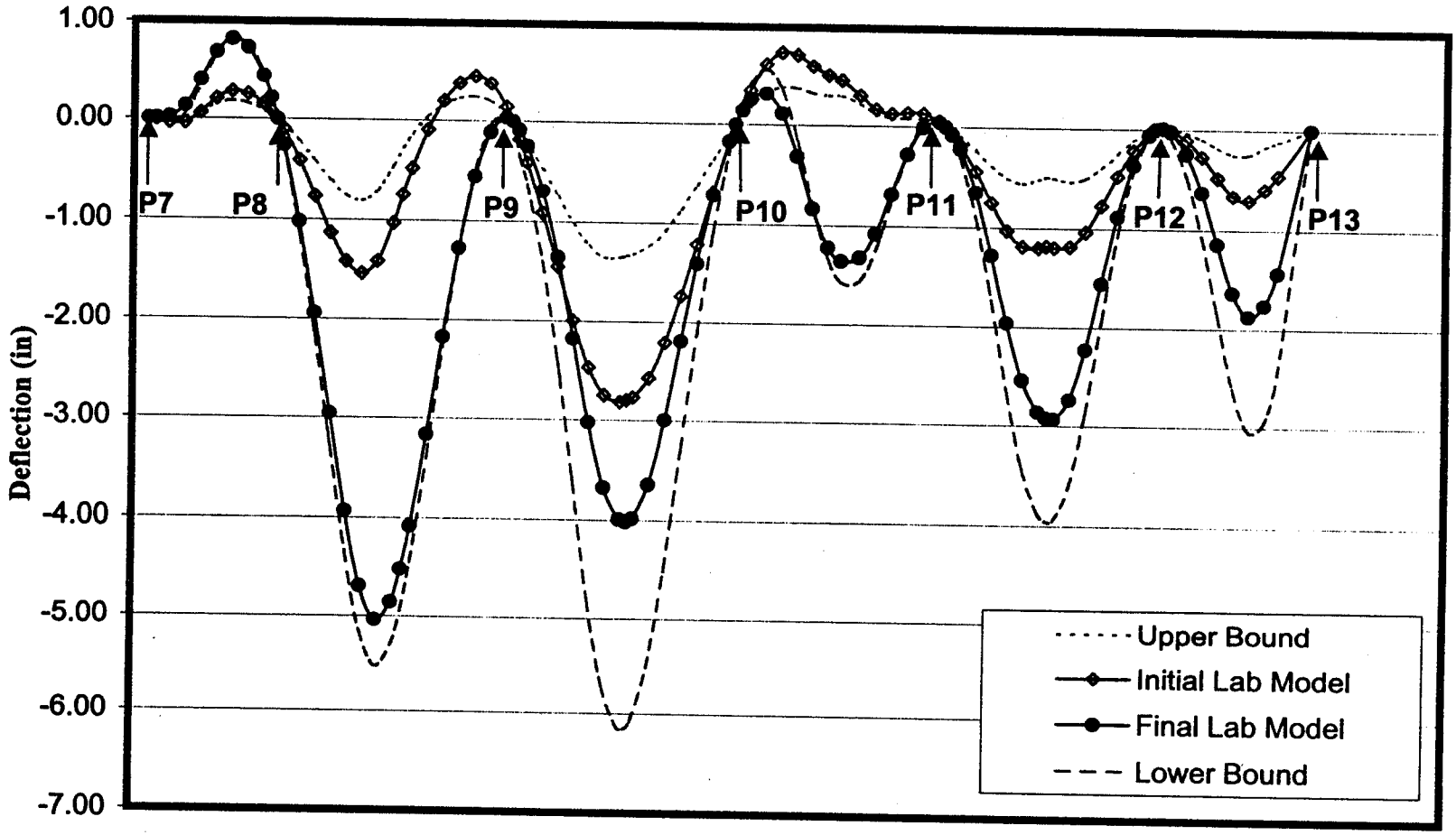

Figure 7.12: Long term deflection envelope (30 years; 3/95-3/2025)

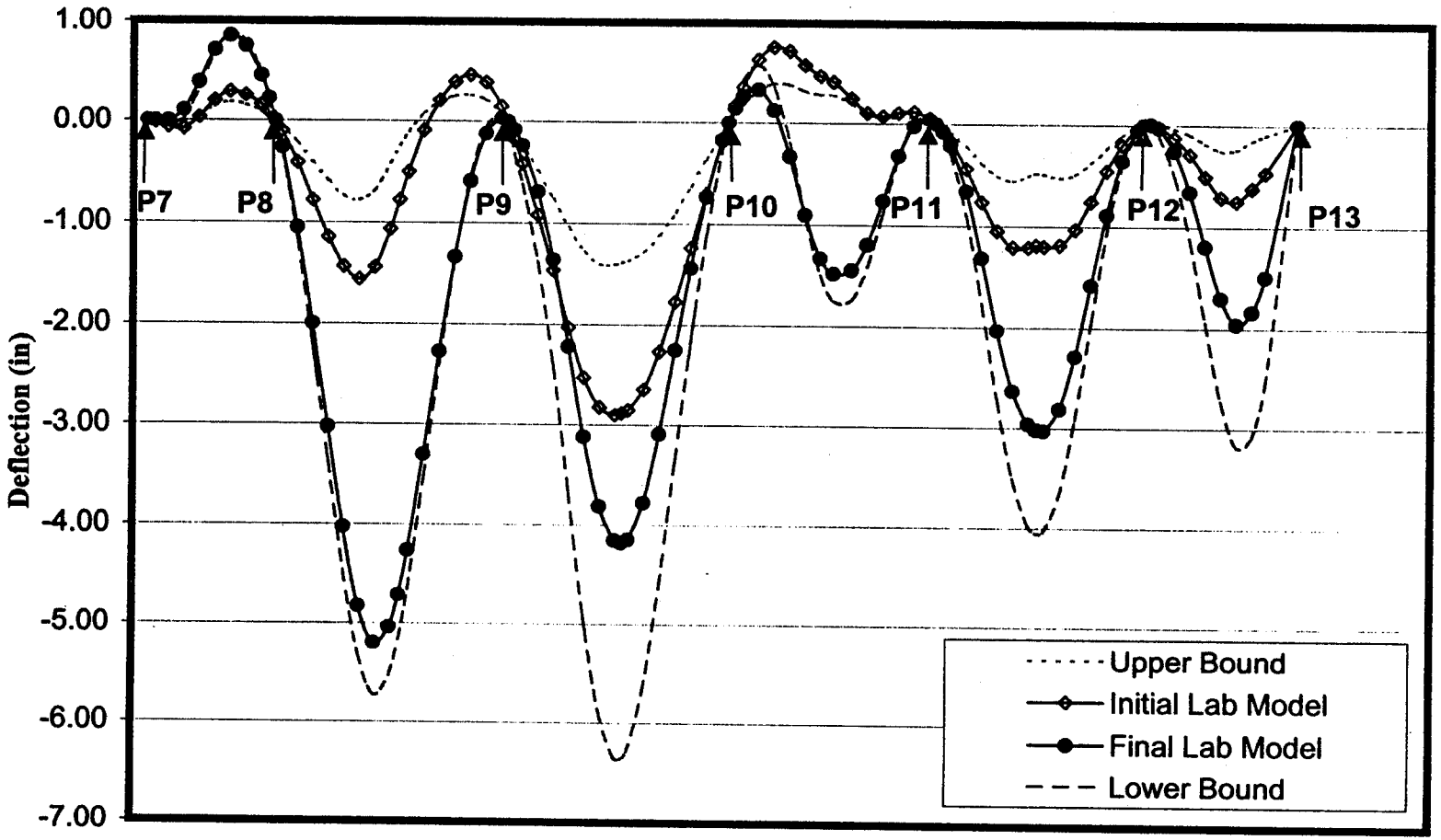

Figure 7.13: Long term deflection envelope (40 years; 3/95-3/2035)

7.13). In reality, at the start of a project, the design engineer would only have access to the initial lab model and the deflection envelope. The absolute maximum anticipated deflection would than be 6.4 inch at midspan of P9-10 (Figure 7.13). Continued monitoring of the bridge deflections will allow for future confirmation of the analytical model's predictions.

7.5 Midspan deflection with time

Figures 7.14 through 7.17 illustrate the increase in midspan deflection over 40-years for all four instrumented spans as predicted by the final lab model and the deflection envelopes. The deflection continues to increase for a long period of time, but the rate of increase decreases with time.

7.6 Span shortening envelope

Figures 7.18 through 7.23 illustrate the upper and lower limits of axial shortening for all six spans of Unit 2IB extended to 40 years after completion of construction. The same upper and lower bound parameters used in the deflection prediction were used here. This would be useful as a design guide for determining the bearing size required at each sliding support.

By extending the final lab model prediction to 40 years, an estimate of the total span shortening for each span is obtained (Figures 7.18 to 7.23). Assuming zero longitudinal movement at midspan of P9-10, the span between fixed piers P9 and P10, the bearing

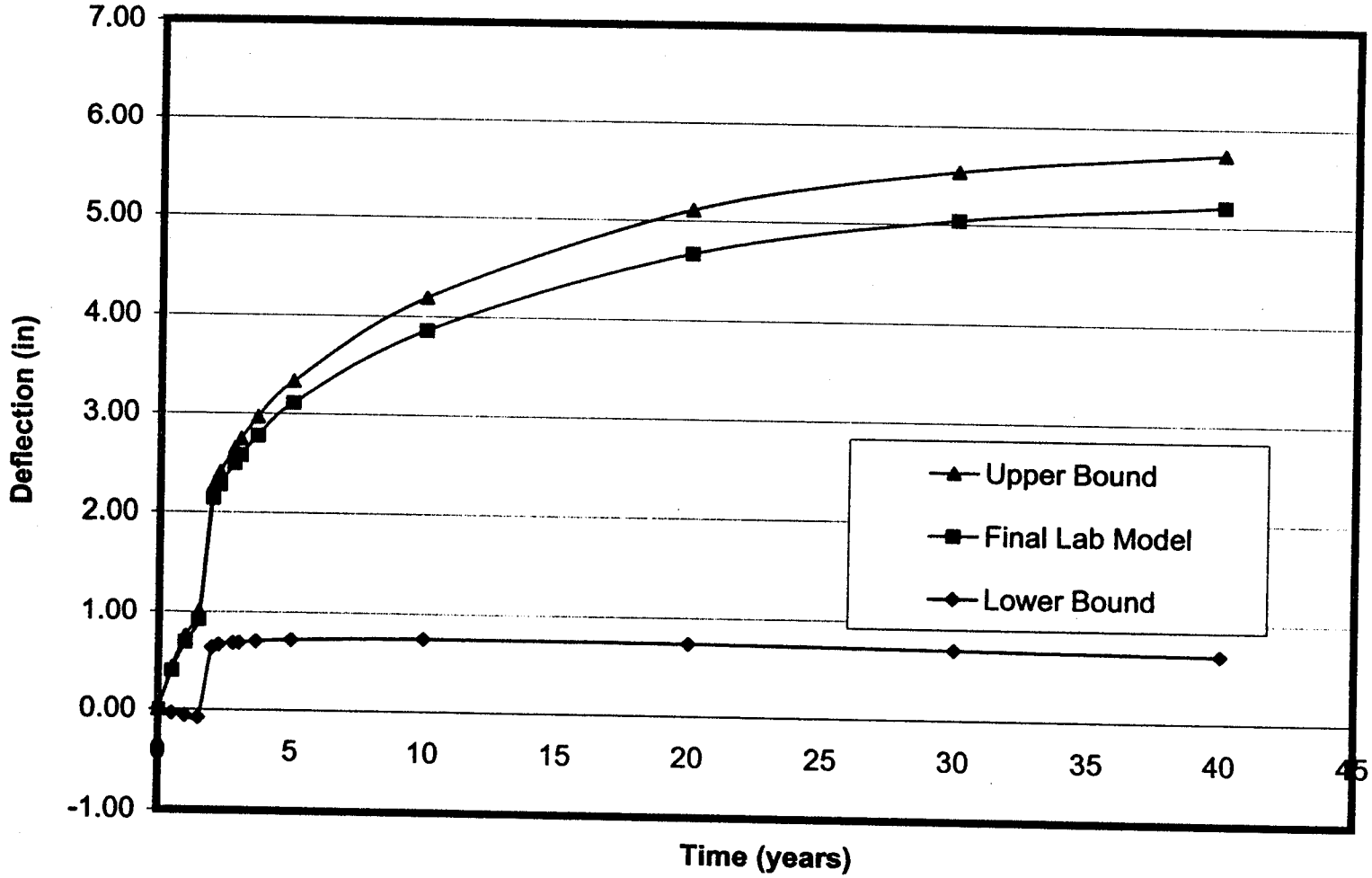

Figure 7.14: Midspan P8-9 deflection envelope

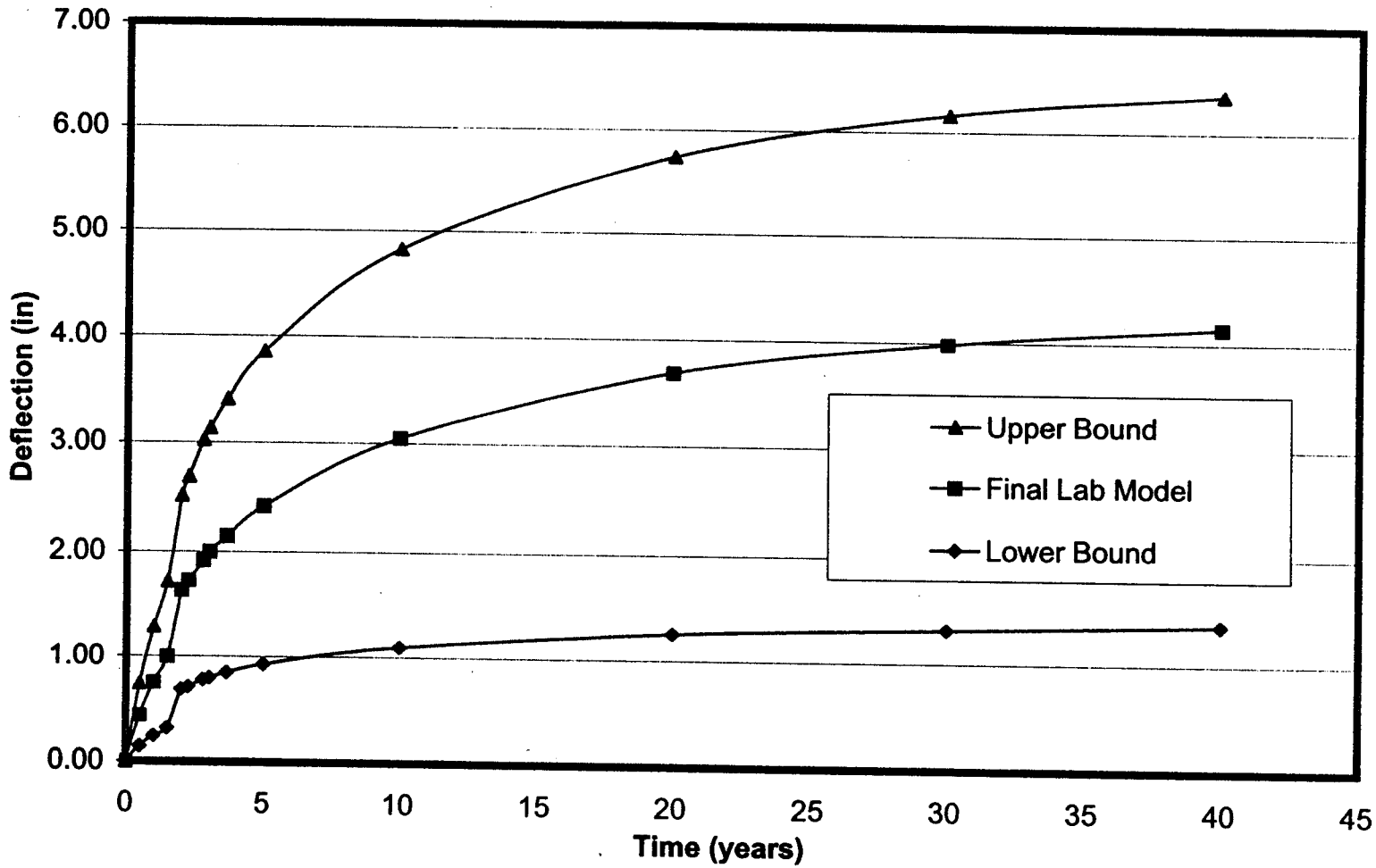

Figure 7.15: Midspan P9-10 deflection envelope

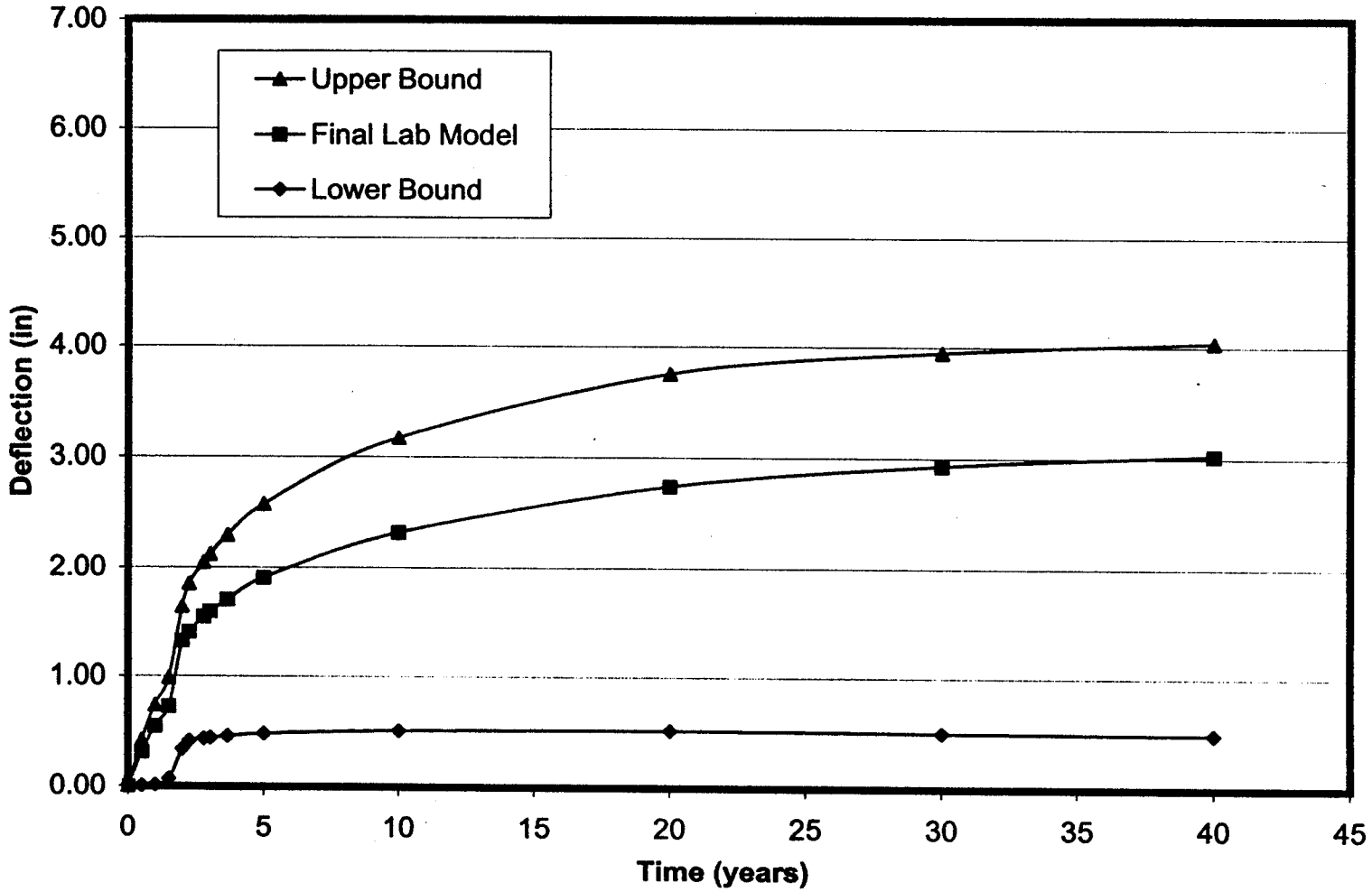

Figure 7.16: Midsapn P11-12 deflection envelope

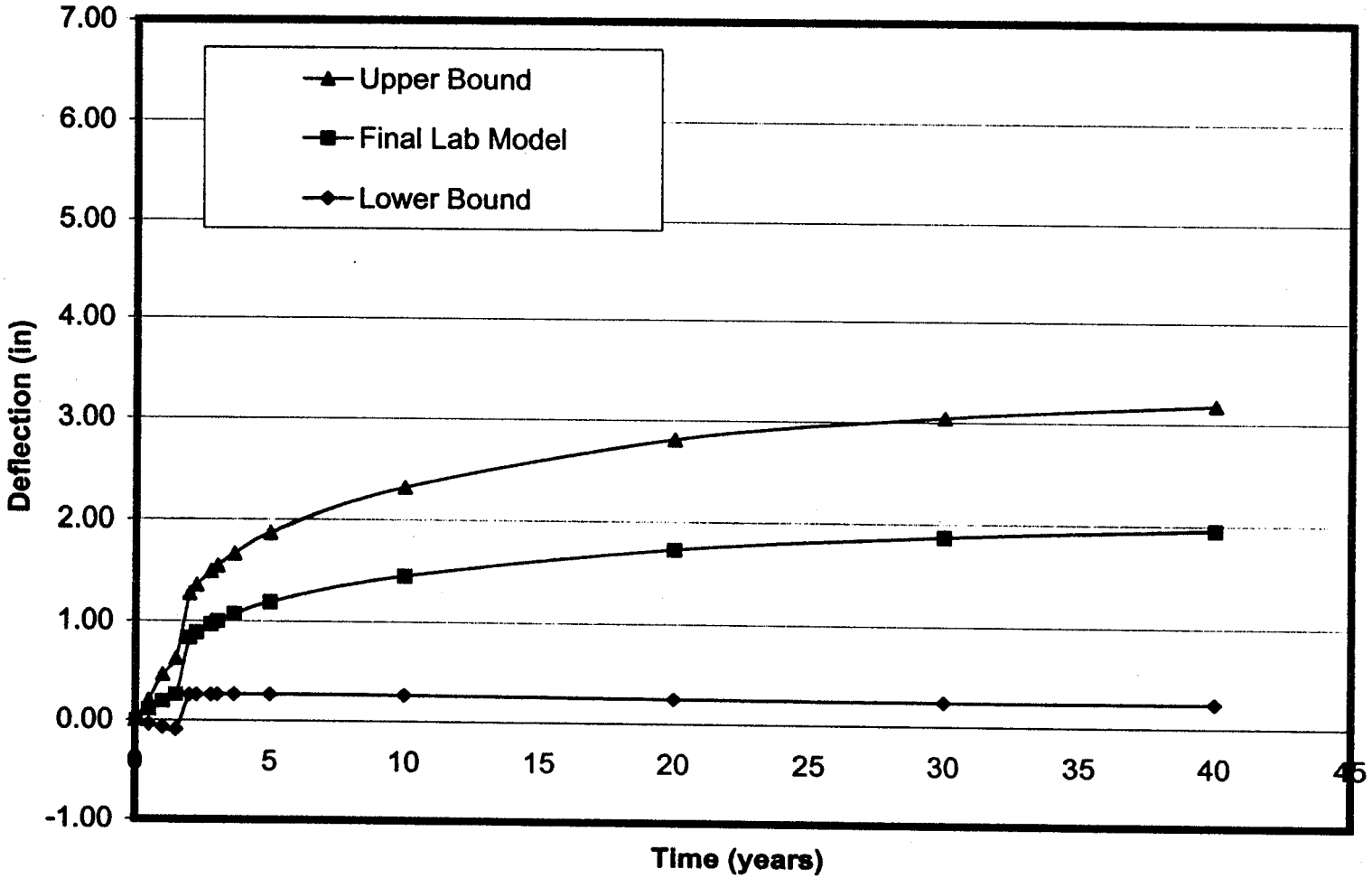

Figure 7.17: Midspan P12-13 defleciton envelope

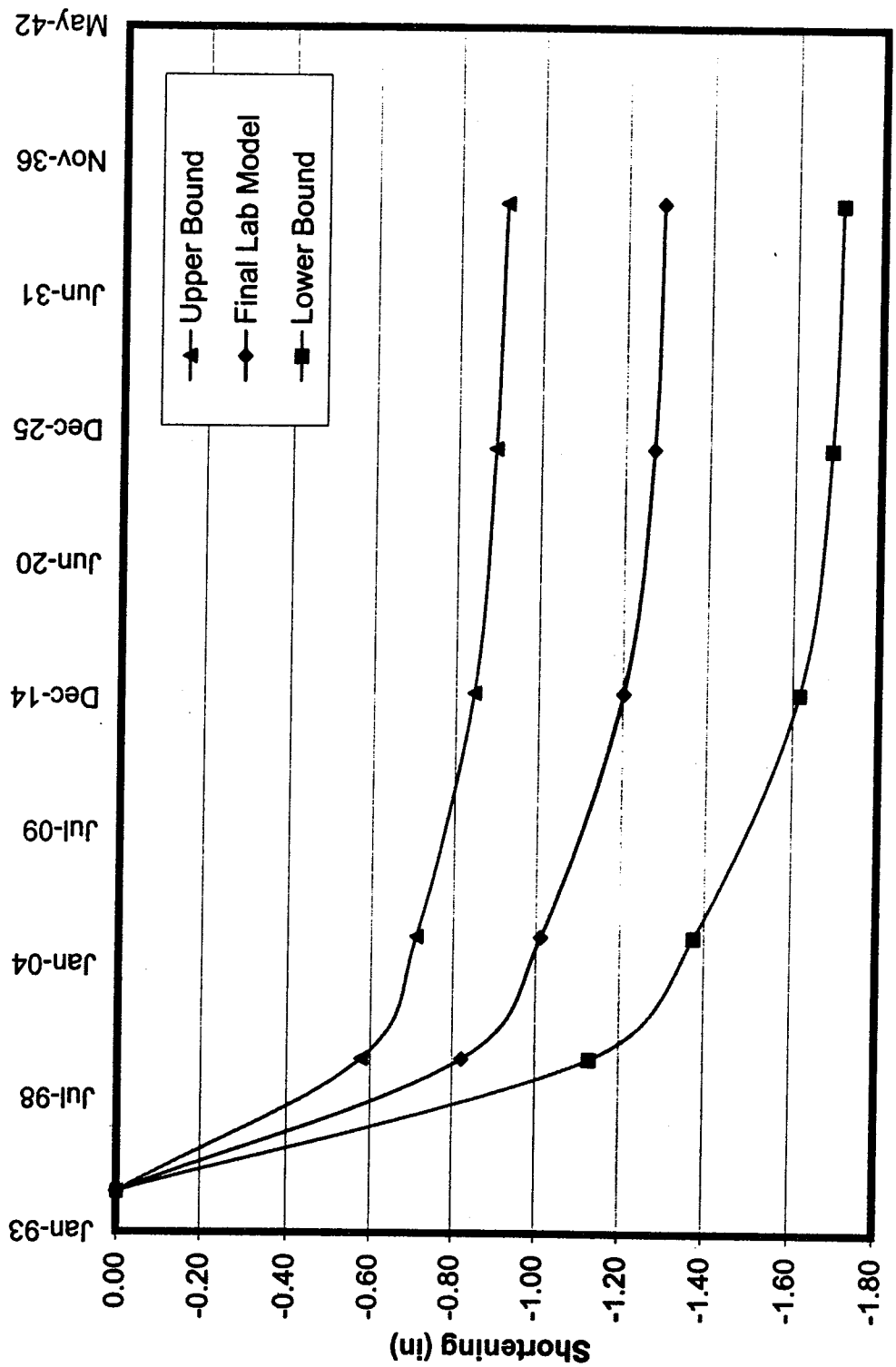

Figure 7.18: Span P7-8 shortening envelope

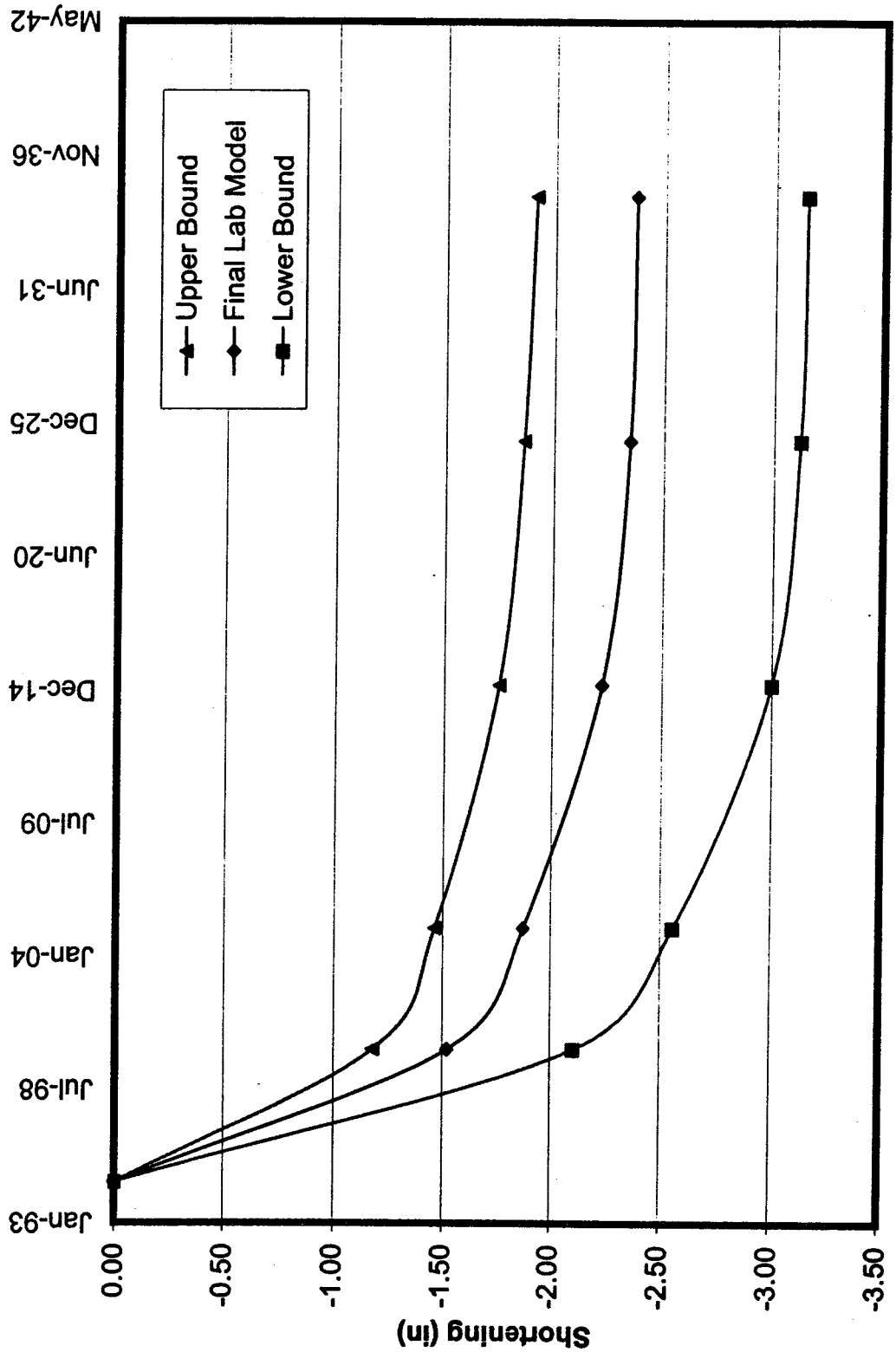

Figure 7.19: Span P8-9 shortening envelope

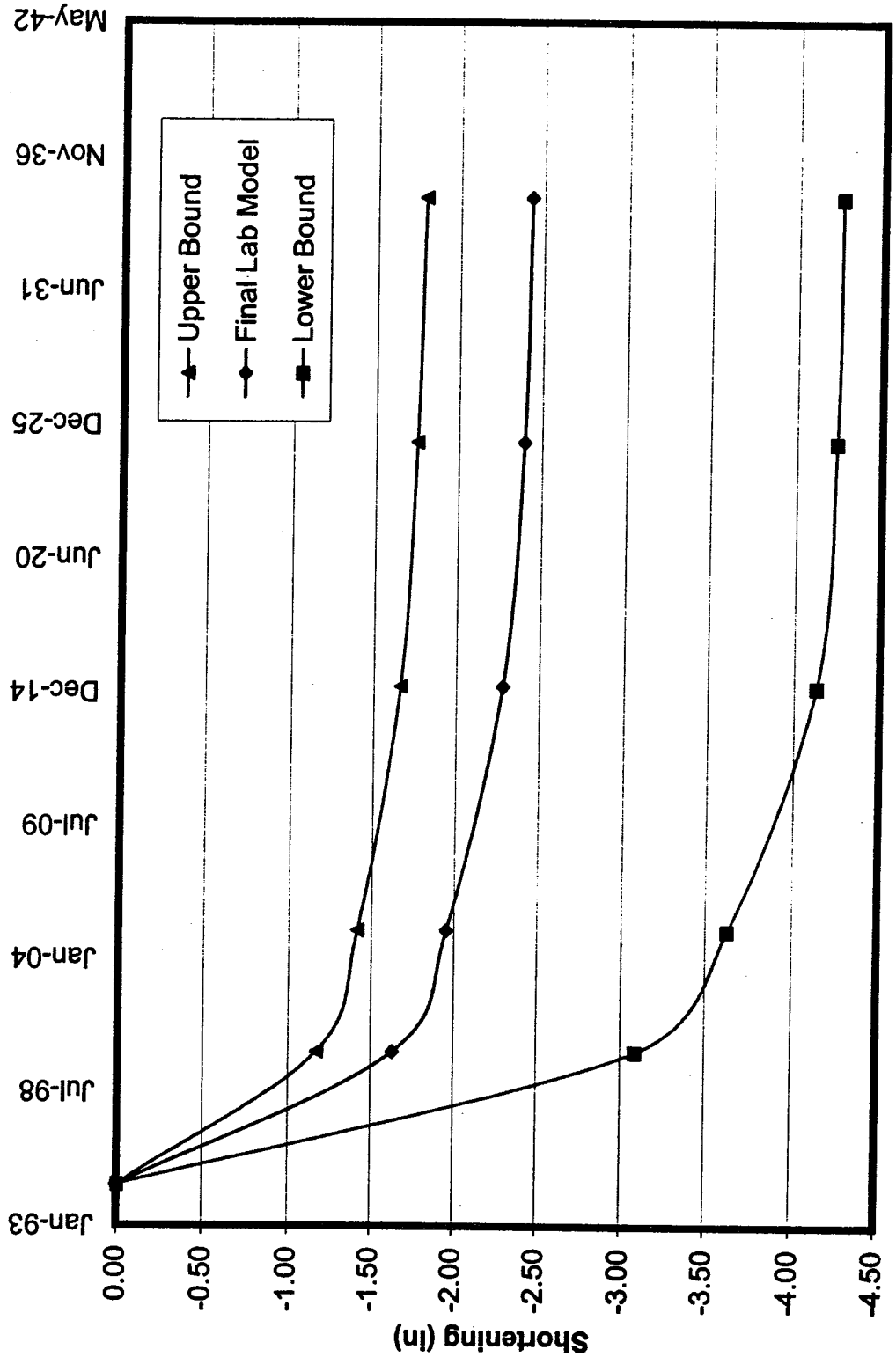

Figure 7.21: Span P10-11 shortening envelope

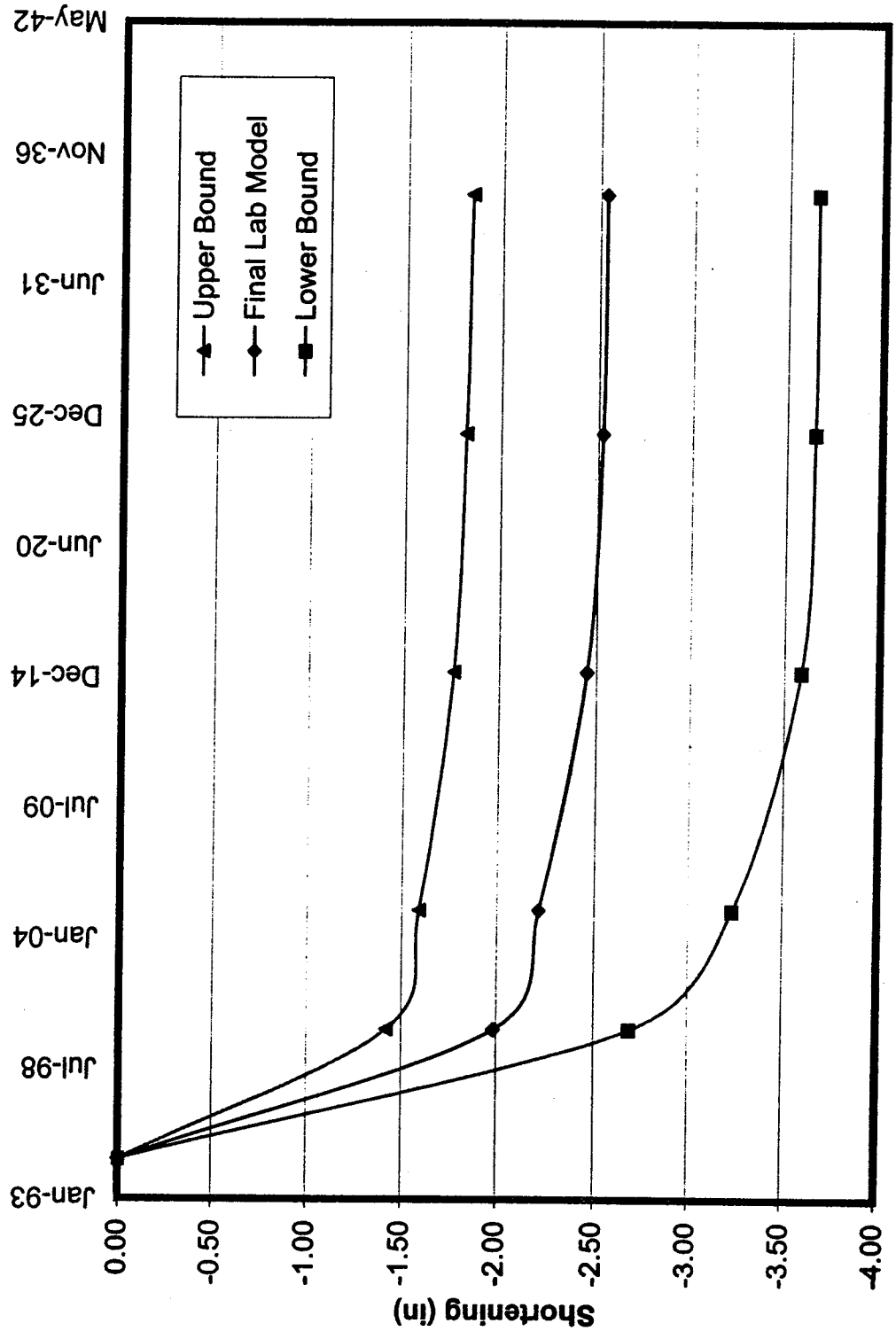

Figure 7.23: Span P12-13 shortening envelope

movement at each sliding support can be estimated as shown in Tables 7.1 and 7.2. After 40 years, it is predicted that the box girder at pier P7 will move 4.81 in. upslope while the box girder at pier P13 will move 9.35 in. downslope.

Table 7.1: Span Shortening (inches)

	P7-8	P8-9	P9-10	P10-11	P11-12	P12-13
End of Construction	0.00	0.00	0.00	0.00	0.00	0.00
5 years	0.82	1.52	1.52	1.63	2.48	1.99
10 years	1.01	1.87	1.84	1.95	2.79	2.22
20 years	1.20	2.23	2.16	2.28	3.10	2.45
30 years	1.27	2.35	2.28	2.40	3.21	2.52
40 years	1.28	2.37	2.31	2.43	3.23	2.54

Table 7.2: Box-girder Movement at top of pier (inches)

(Negative indicates downslope movement)

	P7	P8	P9	P10	P11	P12	P13
5 years	3.10	2.28	0.76	-0.76	-2.39	-4.87	-6.86
10 years	3.80	2.79	0.92	-0.92	-2.87	-5.66	-7.88
20 years	4.51	3.31	1.08	-1.08	-3.36	-6.46	-8.91
30 years	4.75	3.49	1.14	-1.14	-3.54	-6.74	-9.27
40 years	4.81	3.52	1.15	-1.15	-3.58	-6.81	-9.35

CHAPTER 8

CONCLUSIONS

This research was conducted using a time dependent finite element analysis program SFRAME to study the long-term structural performance of Unit 2 IB of the North Halawa Valley Viaduct (NHVV). The responses that were investigated are the long-term vertical deflection, span shortening, and prestress losses. Field measurements were made using a base line deflection system, tiltmeters, optical surveys, extensometers and load cells installed in Unit 2IB during construction in 1994.

Based on this study, the following conclusions are drawn:

1. Concrete creep and shrinkage results for concrete made using the same mix design can vary significantly. This variability has a major impact on the long-term response of the structure.
2. It is not possible to predict long-term deflection accurately using a single constitutive material model for the entire structure.
3. A more appropriate constitutive model for the long-term concrete behavior can provide a better analytical prediction of long-term structural response.
4. Creep and shrinkage prediction models must be modified based on short-term laboratory test results in order to improve the constitutive material model.

5. A revised version of the ACI R209-92 modulus of elasticity prediction is developed to match the laboratory test results for the concrete used in the NHVV.
6. Shrinkage of the box girder causes shortening of the span between the fixed piers, resulting in inward rotations at the tops of the piers. This results in downward deflection of the span between the fixed piers, but upward deflection in the adjacent spans. This influence decreases with distance from the fixed piers.
7. The optimum design would be one that is viable for a range of creep and shrinkage values. It is recommended that whenever possible, measures should be taken to make designs as insensitive as possible to creep and shrinkage.
8. It is necessary for the designer to estimate likely ranges for each of the critical parameters affecting the long-term structural response rather than using one set of values. Upper and lower deflection envelopes can then be developed in order to provide a reliable estimate of potential structural response.

REFERENCES

1 Lee and Robertson (1995), *Instrucmentation and Long-term Monitoring of the North North Halawa Valley Viaduct,* Report UHM/CE/95-08, Unversity of Hawaii.

2 Ketchum, M. A.(1986), *Redistribution of Stresses in Segmentally Erected Prestressed Concrete Bridges, (SFRAME),* UCB/SESM Report No. 86-07, University of California at Berkeley, Department of Civil Engineering.

3 Shushkewich K.W., Vo N.T., Robertson I.N. (1998), *Instrumentation of the North Halawa Valley Viaduct Oahu, Hawaii Progress Report*, Sep. 1998.

4 T.Y. Lin International, *North Halawa Valley Viaduct Inspection and Maintenance Manual,* Oct. 1998.

5 Gilbert, R.I. (1988), *Time Effects in Concrete Structures*, Elsevier Science Publishers B.V., 1988.

6 Bazant, Z.P., and Baweja, S. (1996), *Short Form of Creep and Shrinkage Prediction Model B3 for Structures of Medium Sensitivity,* Material and Structures, Vol. 29, Dec. 1996.

7 Gardner, N.J., and Zhou, J.W. (1993), *Shrinkage and Creep Revisited*, ACI Materials Journal, May-June 1993.

8 ACI Committee 209 (1996), *Creep and Shrinkage Prediction Model for Analysis and Design of Concrete Structures*, Draft report by ACI Committee 209, Creep and Shrinkage in Concrete.

9 CEB (1993), Comite Euro-International du Beton, *CEB-FIP Model Code 90*, published by Thomas Telford Services for the Comite Euro-International du Beton, 1993.

10 Hamada, H., Watari, J., and Chiu, A. (1972), *Creep and Shrinkage of Concrete made from Hawaiian Aggregates,* Technical Report CE71-R2, Department of Civil Engineering, University of Hawaii, Feb. 1972.